Scilight

*Environmental and Microbial Technology*
https://www.sciltp.com/journals/emt

*Review*

Check for updates

# Transition Metal Catalysts in Persulfate-Based Advanced Oxidation Processes: Structural Features, Activation Mechanisms and Applications

Yong Liu [1,2]

[1] College of Chemistry and Materials Science, Sichuan Normal University, Chengdu 610066, China; liuyong75@sicnu.edu.cn
[2] Sichuan Environmental Protection Key Laboratory of Persistent Pollutant Wastewater Treatment, Chengdu 610066, China

**How To Cite:** Liu, Y. Transition Metal Catalysts in Persulfate-Based Advanced Oxidation Processes: Structural Features, Activation Mechanisms and Applications. *Environmental and Microbial Technology* **2026**, *1*(1), 15. https://doi.org/10.53941/emt.2026.100015

Received: 20 April 2026
Revised: 2 June 2026
Accepted: 12 June 2026
Published: 3 July 2026

**Abstract:** Transition metal (TM) catalysts play a pivotal role in persulfate (PS)-based advanced oxidation processes (AOPs) due to their tunable electronic structures and versatile activation mechanisms. These catalysts enable PS activation through both homogeneous and heterogeneous pathways. In homogeneous systems, the catalytic activity is governed by the elemental composition and ligand coordination of TM. For heterogeneous systems, the catalytic activity of TM active site depends dominantly on its electronic states, which are critically regulated by intrinsic structural features, including particle size, crystalline phase, surface defect density, and the coordination micro-environments. To enhance the activity and stability of TM catalysts, strategic support-loading approaches have been developed, where catalytic performance is also synergistically determined by the support's structure and metal-support interactions. Accordingly, TM catalysts with various structures synthesized by various synthesis methods have been developed to activate PS. This review systematically summarized recent advances in the rational design of TM catalysts, focusing on: (1) synthesis methods and corresponding structure features of TM catalysts; (2) PS activation mechanisms by TM catalysts with different structure features and the catalytic activity enhancement strategies. Moreover, key factors influencing the emerging contaminants (ECs) degradation efficiency in TM-activated PS systems, such as pH, coexisting anions, and dissolved organic matter alongside the enhancement strategies were discussed. Finally, the challenges and future research directions were proposed. This review will deepen the understanding of the structural features, activation mechanisms and applications of TM catalysts in PS-based AOPs, and promote the design and development of advanced and practical application-oriented TM catalysts for the treatment of ECs in water and wastewater.

**Keywords:** advanced oxidation processes; persulfate; activation mechanism; emerging contaminants; transition metals

## 1. Introduction

Advanced oxidation processes (AOPs), such as Fenton oxidation [1,2], catalytic ozonation [3,4], ionizing radiation [5,6] have gained prominence as a leading remediation strategy [7,8], because they can degrade emerging contaminants (ECs) via reactive oxygen species (ROS) (e.g., sulfate radical ($SO_4^{\bullet-}$), hydroxyl radical ($^{\bullet}OH$)). Among various AOPs, persulfate (PS)-based AOPs have attracted significant interest due to their low peroxide bond (O-O) energies and distinct structures that promote easier activation and more diverse ROS generation, compared to conventional oxidants (e.g., $H_2O_2$, $O_2$, $O_3$) [9–12].

Persulfates (PS) mainly comprise two categories: peroxymonosulfate (PMS) and peroxodisulfate (PDS), with their structural features depicted in Figure 1a,b. The molecular formula for PMS is $HSO_5^-$, which can be conceptualized as $H_2O_2$ with one hydrogen atom substituted by $HSO_3^-$. The O-O bond length measures 1.453 Å, with a bond energy ranging from 140 to 213.3 kJ/mol [13]. The molecular formula for PDS is $S_2O_8^{2-}$, analogous to $H_2O_2$ but with both hydrogen atoms replaced by $HSO_3^-$. The O-O bond length in PDS is 1.497 Å, exhibiting relatively lower bond energy (92–140 kJ/mol) [13]. The PMS, featuring an asymmetric charge distribution, is prone to nucleophilic attack, whereas the PDS, with a symmetric charge distribution, exhibits lower susceptibility to nucleophilic reagents.

The PS activation requires external energy input (e.g., heat, light, ultrasound, or microwave) or catalysts (e.g., transition metal (TM) catalysts, carbon-based materials) to cleave the O-O bond, thereby generating highly reactive ROS [14–17]. From Web of Science (2014–2025), we searched 1781 and 7909 papers, respectively, using "PDS activation" and "PMS activation" as topics, respectively. Figure 1c presents the publication trends from Web of Science (2014–2025). As depicted from Figure 1d, there are approximately 14,026 papers focusing on PMS activation and PDS activation in total, whereas the total number of papers concerning PMS activation and PDS activation by TM (Fe, Cu, Mn, Co, Mo, Ni, Ti, Pd, W, Pt, Ru, Rh, Ir) reaches around 10,775. These trends indicate that TMs are excellent catalysts and are highly favored compared to energy-based activation methods, such as heat, UV and ultrasound [18], etc., due to less energy consumption [19,20].

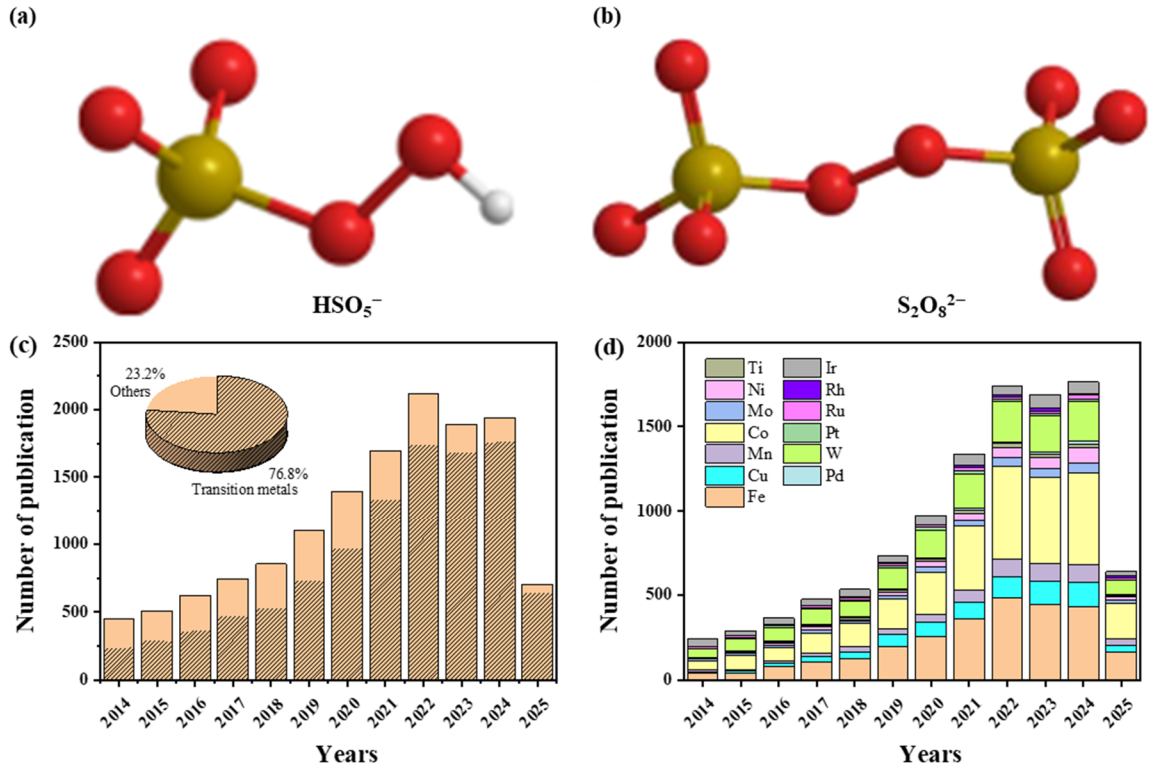


**Figure 1.** (**a**,**b**) The structures of PMS/PDS and (**c**,**d**) trends of publications on PS activation by TM catalysts (2014–2025).

Transition metals (TMs) are located in groups 3–12 of the periodic table (d-block elements), which are characterized by partially filled d orbitals (or the ability to form such configurations) [21,22] Based on their abundance and economic value, TMs can be categorized into: (1) precious metals: Pt, Pd, Ru, Rh, Ir; (2) non-precious metals: Fe, Co, Ni, Cu, Mn; and (3) rare metals: Mo, W, Re. Among these TMs, Co, Fe, W, Cu, Mn, Mo, Ni, and Ti are commonly employed for PS activation due to its variable oxidation states, low cost and availability (Figure 1d).

The unique electronic structure endows TMs outstanding catalytic activity for PS activation, which is mainly reflected in that (1) partially filled d orbitals facilitate coordination with reactants or intermediates (e.g., the overlap of 3d orbitals of TMs and the $O_{2p}$ orbitals of PS or contaminants), lowering activation energy barriers [23,24]; (2) small energy gaps between d orbitals enable facile electron transitions, allowing TMs to adopt multiple oxidation states (e.g., $Fe^{2+}/Fe^{3+}$, $Cu^{+}/Cu^{2+}$) and serve as electron shuttles to drive reactions [25,26]; (3) the d-orbital symmetry alignment with reactant antibonding orbitals weakens target bonds (e.g., O-O, C-H) via electron back-donation,

enhancing bond cleavage [27,28]; (4) the large ionic radii of some TMs permit ligand incorporation, tuning catalytic activity and selectivity through electronic, steric, and asymmetric effects [29,30].

Owing to their unique and adjustable valence electron configurations (e.g., electronic states, coordination environments, and geometries), TMs can activate PS via multiple mechanisms, mainly including single electron transfer, oxygen transfer or TM-PS* complex. During the PS activation, most TMs may occur valence cycling. The element composition, oxidation valence, and coordination microenvironments of TMs collectively determine their electronic structure and subsequent interaction with PS. Based on their solubility in aqueous systems, TM catalysts are categorized as either homogeneous or heterogeneous.

In homogeneous systems, the element composition and ligand coordination of TMs affect greatly the coordination and electron transfer of TM catalysts with PS/ECs [31].

Heterogeneous TM catalysts can be classified by TM particle size:(1) single-atom TM catalysts (SA-TMCs) (0.1–0.3 nm) [32]; (2) nanoscale TM catalysts including sub-nanometer clusters TM catalysts (0.3–1 nm) and nanoparticles TM catalysts (1–100 nm, typically 2–10 nm for optimal catalysis) [33,34]; (3) bulk TM catalysts (>100 nm to micrometer scale) [35,36]. This size effect modulates surface atomic coordination, geometric structure (atomic arrangement), and electronic properties (e.g., d-band center position), ultimately governing catalytic activity, selectivity, and stability [37].

Heterogeneous TM catalysts can also be classified as unsupported or supported based on the presence of support. The support not only disperses TM atoms but also precisely modulates their electronic structure (e.g., d-band center, oxidation state, orbital hybridization) through charge transfer, coordination effects, strain engineering, and quantum confinement. Moreover, the support can minimize the leaching of TM ions [38–40]. Understanding these structure modulation strategies is critical for designing advanced TM catalysts with enhanced PS activation performance. Thus, in order to favor the application of TM catalysts in PS activation, it is necessary to deeply understand the structure-activity relationship of TM catalysts and the interaction mechanism of TM with PS/ECs. Furthermore, the structure of the TM catalyst is determined by the synthesis method. It is very necessary to understand the influence of some synthesis methods on their structures for synthesizing catalysts with the expected structures.

The degradation efficiency of ECs depends on both their molecular structures and the generated ROS [41,42]. In complex wastewater matrices, the formation of these ROS is influenced not only by the catalyst structure but also by wastewater compositions (e.g., coexisting substances and pH) and the structure properties of ECs [43]. A key challenge lies in how to utilize the diverse ROS from TM-activated PS systems to effectively degrade structurally varied ECs in such complex wastewater matrices. Recent studies have focused on enhancing ROS generation efficiency, optimizing ROS composition, strengthening mass transfer and improve the reactor for specific contaminants to minimize wasteful oxidant consumption [44–46]. Understanding these mechanistic principles is crucial for advancing the practical implementation of TM-activated PS-based AOPs.

Over the past decade, PS-AOPs has garnered extensive attention in the field of water and wastewater treatment, with a large number of review articles dedicated to this subject [47–49]. Current reviews primarily evaluate this technology from various perspectives: Some studies concentrate on the performance and application of specific catalyst types, including SA-TMCs catalysts [17], metal-organic framework (MOFs)-derived catalysts [50], carbon-based catalysts, and iron-based bimetallic catalysts, offering a systematic overview of their preparation methods and degradation efficacies. Other reviews categorize the technology based on activation methods, encompassing thermal activation [51], photoactivation [52], electro-activation [53], ultrasonic activation [54], and metal catalyst activation [55]. Additionally, certain studies specifically address particular pollutant categories, such as antibiotics [56], sulfonamides [57], and emerging contaminants [58], examining the effectiveness and constraints of PS-AOPs in their removal.

However, most of the aforementioned reviews predominantly adopt a singular perspective, categorizing catalysts either by their types, by activation methodologies, or by focusing on specific categories of pollutants. Few studies have systematically integrated the synthesis methods, structural attributes, mechanisms of PS activation catalyzed by TM with diverse structures, strategies for augmenting catalytic activity, and the influencing factors of these catalysts in the degradation of ECs within aqueous environments. Specifically, research on the correlation between the activation mechanisms of TM catalysts and their structural features remains notably insufficient, and the intrinsic link between the structural features of catalysts and the generation efficiency of ROS necessitates systematic explication. Furthermore, the existing literature is deficient in comprehensive summaries regarding strategies for enhancing TM catalyst activity, as well as in multidimensional analyses concerning the impact of actual aquatic environmental factors on the degradation process.

This review is intended to compensate for the aforementioned shortcomings by focusing on TM catalysts as the core subject. It systematically examines multiple critical dimensions, including their synthesis methods, structure-activity relationships, activation mechanisms, performance optimization strategies, and factors

influencing practical applications. The objective is to construct a comprehensive knowledge framework that covers the sequence from "synthesis methods → structural characteristics → activation mechanisms → activity enhancement → application to ECs degradation". This review will inspire the development of novel and efficient TM-activated PS-based AOPs for the effective removal of ECs from water and wastewater.

## 2. Structural Features and Synthesis Methods of Heterogeneous TM Catalysts

Heterogeneous TM catalysts are characterized by a range of structural features, including morphology, composition, crystallinity, specific surface area, surface defects, functional groups, TM valence states, and local coordination environments [59–61]. These features can be systematically analyzed using advanced characterization techniques: Morphology & composition are resolved through SEM/TEM imaging combined with EDS elemental mapping [62–64]. Crystal structure primarily elucidated via XRD for phase identification, supplemented by HRTEM/SAED for lattice resolution and EXAFS/XANES for coordination environment analysis [65,66]. Surface/interface properties are dissected by XPS (oxidation states), Raman (defects), and FT-IR (functional groups). Porosity and surface area are often quantified by BET nitrogen adsorption measurements [67,68].

The structural features of TM catalysts are intrinsically linked to their synthesis methods. Common synthesis strategies include precipitation/co-precipitation method, hydrothermal/solvothermal method, impregnation method, ion exchange method, pyrolysis-based method, and solution-phase coordination method. The selection of synthesis method is critical, as it directly governs the TM catalyst's final structure and, consequently, its catalytic performance (Figure 2).

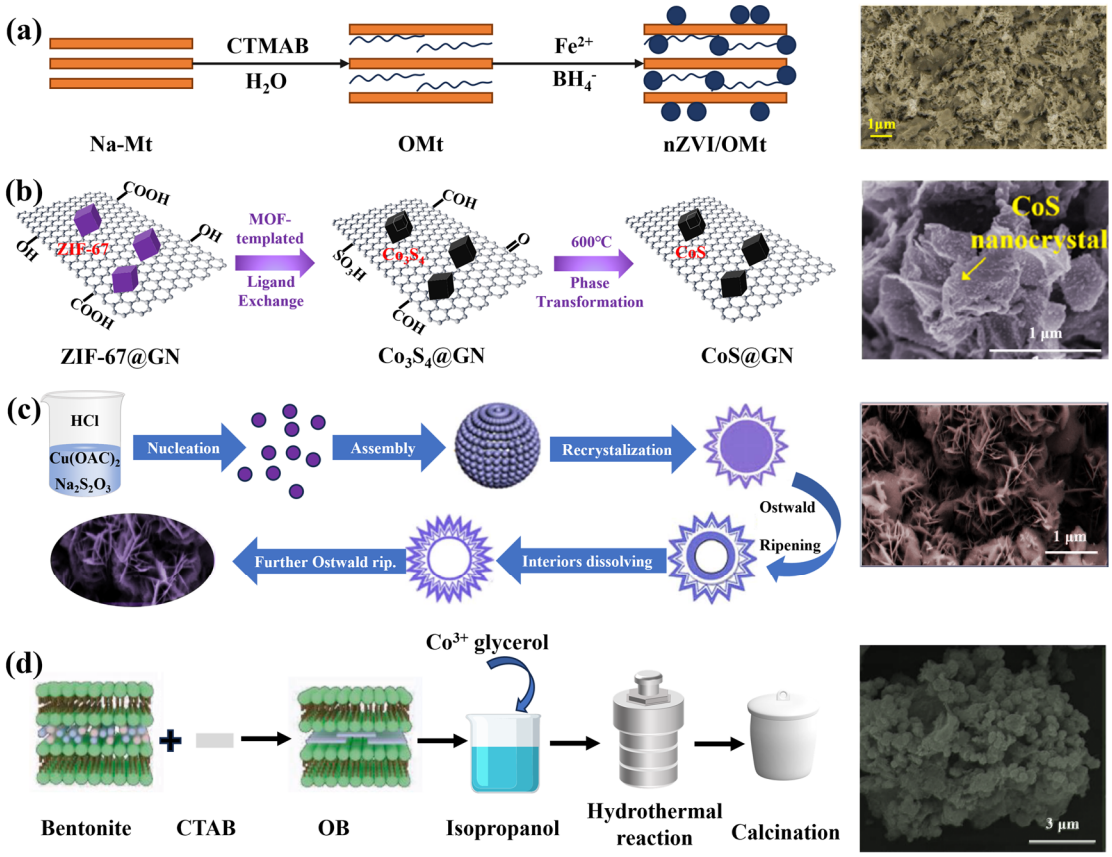


**Figure 2.** Synthesis methods and structural characteristics of representative TM catalysts. (**a**) nZVI/OMt [69]; (**b**) CoS@GN [70]; (**c**) CuS@N-doped CNCs [71]; (**d**) $Co_3O_4$/Bent [72]. (Adapted from the corresponding reference)

### *2.1. Unsupported TM Catalysts*

#### 2.1.1. Structure Features

Based on the valence state of TM, non-supported TM catalysts can be classified zero-valent TM (e.g., metallic Fe, Co, Ni nanoparticles) and TM compounds (e.g., oxides, sulfides, phosphates). Based on the element composition of TM, it can be classified two key criteria: Single TM catalysts: (e.g., TM oxides, TM sulfides, TM phosphates) and composite TM catalysts: (e.g., perovskites oxides, spinel oxides, layered double hydroxides

(LDHs)). In this review, the structural features and synthesis methods of some representative unsupported TM for PS activation will be discussed.

Single TM oxides are compounds composed of one TM element and oxygen. Representative single TM oxides for PS activation are including $Fe_2O_x$, $Co_3O_x$, $MnO_x$, $CuO_x$. Key features of single TM oxides are the variable oxidation states (e.g., $Fe^{II}/Fe^{III}$, $Mn^{II}/Mn^{III}/Mn^{IV}$) and non-stoichiometric compositions caused by the intrinsic defects (e.g., oxygen vacancies (OVs), metal vacancies, interstitial atoms). Analogs of single TM oxides, single TM sulfides sharing similar compositional and structural features: variable metal states (e.g., $Mo^{IV}/Mo^{VI}$ in $MoS_2$), non-stoichiometric phases (e.g., $Cu_{2-x}S$) and mixed-valence sulfides [73,74]. Common TM sulfides for PS activation including $FeS_2$, $MoS_2$ and $CuS_x$, etc.

General chemical formula of perovskite-structured TM oxides is $ABO_3$, where: A-site is large-radius cation with +1, +2, or +3 valence states, occupying cuboctahedral interstitial sites. B-site is TM ion located at the centers of oxygen octahedra and O-site is oxygen ions, forming the $BO_6$ octahedral framework. In $ABO_3$, the A- or B-site ions can be doped with foreign ions, and non-stoichiometry may arise due to OVs or A/B- site deficiencies. Representative unsupported $ABO_3$ for PS activation include strontium-doped ruddlesden-popper perovskites ($Sr_xLa_{2-x}CoO_{4\pm\delta}$, x = 0.6–1.5), barium-strontium cobalt ferrites ($Ba_{0.5}Sr_{0.5}Co_{0.8}Fe_{0.2}O_{3-\delta}$), and nickel-substituted lanthanum cobaltites ($LaCo_{0.5}Ni_{0.5}O_3$) [75–77].

The chemical formula of spinel-structured TM oxides is $AB_2O_4$, where A-site is typically occupied by divalent metal ions. B-site is usually trivalent TM ion and O-site is oxygen ions form a closely packed framework. In $AB_2O_4$, the A- or B-site ions can be substituted by foreign metal ions, and their catalytic properties are often modulated through defects such as cation vacancies or OVs.

The general chemical formula of layered double hydroxides (LDHs) is $[Me^{II}_{1-x}Me^{III}_x(OH)_2]^{x+}\cdot(A^{n-})_{x/n}\cdot mH_2O$. $Me^{II}$ and $Me^{III}$ are divalent and trivalent metals, $A^{n-}$ are interlayer anions, and $x$ is the molar ratio of $Me^{III}/(Me^{II} + Me^{III})$, typically ranging from 0.2 to 0.33, which determines the layer charge density. The properties of LDHs can be tailored by varying the $Me^{II}/Me^{III}$ combinations. The interlayer anions are exchangeable, enabling functionalization, while the $x$ value influences layer charge and stability. Additionally, catalytic activity can be optimized through metal or hydroxyl vacancies. Further electronic structure modulation is achievable by incorporating heterovalent ions (e.g., $Me^{IV}$ or $Me^{I}$).

### 2.1.2. Synthesis Methods

The synthesis methods for non-supported TM catalysts primarily include ball milling, precipitation/co-precipitation, and hydrothermal/solvothermal methods (Table 1). Ball milling mainly relies on mechanochemical processes to reduce the particle size of TM, thereby increasing the specific surface area and exposure of active sites. It can also induce lattice distortion and reduced crystallinity in certain TM oxides, modulating their structure and electronic properties. For example, Kang et al. [78] made the particle size of zero valent iron decreased from 8.74 μm to 2.91 μm by ball milling process at 500 rpm for 12 h with the addition of $Na_2S_2O_8$. Liu et al. [79] found that ball milling of $Mn_3O_4$ at a speed of 500 rpm for 2.5 h induced the lattice distortion and chemical bond fracture of $Mn_3O_4$ and destroyed its symmetry.

In the precipitation method, $OH^-/CO_3^{2-}$, $S^{2-}$ or $PO_4^{3-}$ are the common precipitating agents for TM oxides, TM sulfides or TM phosphates synthesis, respectively. The co-precipitation method can be used for the synthesis of various structured mixed-metal oxides, such as spinel, perovskites, LDHs, and core-shell structures. For instance, Hu et al. [80] prepared the $Co_3O_4$-$Bi_2O_3$ catalyst with a surface of uniform distribution of element Co and Bi via a microwave-assisted co-precipitation method under microwave irradiation at 150 W for 20 min followed by calcination at 200 °C. Bao et al. [81] fabricated ZnFe-LDH through a facile co-precipitation method involving slow alkalization of a $Fe(NO_3)_2/Zn(NO_3)_2$ mixed solution, followed by an aging process. Ke and Huang [82] synthesized Mn-Fe bimetallic oxide nanocubes with a hollow/porous spinel structure via a modified co-precipitation method.

The hydrothermal/solvothermal method leverages high-temperature/pressure liquid-phase reactions to enable precise control over catalyst morphology and nanocrystalline phases, yielding TM catalysts with well-defined architectures. For example, a low-crystallinity composite structure OVs-α@δ-$MnO_2$ (α/δ heterojunction) was fabricated through using δ-$MnO_2$ as the precursor under hydrothermal conditions (160 °C, 16 h) [83]. Wu et al. [84] facilitated a layered Fe-Co LDH structure with electron-enriched localized defects through hydrothermal coupled with hydrogen reduction process. In addition, the TB-ZnO (mesocrystalline branched structure) with optimized OVs concentrations [85] and CuCoNi oxide nanowires with stabilized three-dimensional architectures [86] were prepared via hydrothermal process, respectively.

**Table 1.** Structural features and synthesis strategies of representative unsupported TM catalysts.

| Catalysts | Precursors | Synthesis Methods | Synthesis Conditions | Catalyst Features | | | | References |
|---|---|---|---|---|---|---|---|---|
| | | | | Particle Size | Elements | Structure | Functional Groups/Defect Sites | |
| $Ru_n$/NC-850 | Melamine, $RuCl_3$ | Pyrolysis | 850 °C | 3 nm | Ru, O, N, C | Hexagonal Ru crystals | pyridinic-N | [87] |
| PSZVI$^{bm}$ | $Fe^0$, $Na_2S_2O_8$ | Ball milling | 12 h, 500 rpm | 12.3 μm | Fe, O, S, C | Chainlike spherical structure | / | [78] |
| Fe-Cu | $FeCl_3·6H_2O$, $CuSO_4·5H_2O$ | $Fe^0$: $NaBH_4$ reduction; Fe-Cu: displacement | $Fe^0$: 0.5 h; Fe-Cu: 0.3 h | / | Fe, Cu, O | Spherical shape | / | [88] |
| BM $Mn_3O_4$ | $Mn_3O_4$ | Ball milling | 2.5 h, 500 rpm | 50 nm | Mn, O | Spinel crystalline structure | / | [79] |
| γ-$Al_2O_3$ | $Al_2O_3$ | / | / | / | Al, O | Spherical shape | hydroxyl groups | [89] |
| $CO_3O_4$-L | $CoSO_4·7H_2O$, urea | Hydrothermal-calcination | Hydrothermal: 95 °C, 6 h; calcination: 300–400 °C, 2 h | / | Co, O | Stacked lamina morphology, spinel structure | OVs | [90] |
| OVs-α@δ-$MnO_2$ | $MnSO_4·H_2O$, $KMnO_4$, urea | One-step hydrothermal | 160 °C, 16 h | 500 nm | Mn, O, K, C | Rod-like nanoflower nanostructure | hydroxyl groups/OVs | [83] |
| TB-ZnO | $Zn(NO_3)_2$, hexamethylene tetramine | Hydrothermal-calcination | Hydrothermal: 80 °C, 21 h; calcination: 300 °C, 3 h | / | Zn, O | Symmetric twin-brush-like structure | OVs | [85] |
| Cu-Al@PVDF | $Cu(NO_3)_2·3H_2O$, $Al(NO_3)_3·9H_2O$, urea, polyvinyl pyrrolidone; N,N-Dimethylacetamide; PVDF | Cu-Al: Co-precipitation; Cu-Al@PVDF: phase inversion | Cu-Al: 500 °C, 2 h; Cu-Al@PVD F: 60 °C; 12 h | / | Cu, Al, C, O | Porous structure | OVs | [91] |
| MnFeO | $MnCl_2·4H_2O$, polyvinylpyrrolidone | Co-precipitation and calcination | 400 °C, 3 h | 300 nm | Mn, Fe, O | Cubic and spinel structures | / | [82] |
| $Co_3O_4$@$CeO_2$-IE | $Co(OH)_2$, $Ce(NO_3)_3·6H_2O$ | Hydrothermal-calcination | Hydrothermal: 120 °C, 12 h; Calcination: 400 °C, 2 h | / | Co, Ce, O | Hexagonal nanoparticle | OVs | [92] |
| $Co_3O_4$-$Bi_2O_3$ | $Bi(NO_3)_3·5H_2O$, $Co(NO_3)_3·6H_2O$ | Microwave-assisted co-precipitation | Microwave: 150 W, 0.3 h; calcination: 200 °C, 2 h | / | Co, O, Bi | Rod-shaped structure | / | [93] |
| CuCoNi-NF | $Co(NO_3)_2·6H_2O$, $Cu(NO_3)_2·3H_2O$, $CO(NH_2)_2$, $NH_4F$ | Hydrothermal-calcination | Hydrothermal: 120 °C, 8 h; calcination: 350 °C, 3 h | / | Cu, Co, Ni, O | Chestnut-like microspheres, the spinel structure | / | [86] |
| CoMnAl-MMO | $Co(NO_3)_2·6H_2O$, $Mn(NO_3)_2$, urea $Al(NO_3)_2·9H_2O$ | Hydrothermal-calcination | Hydrotherma: 100 °C, 48 h; Calcination: 500 °C, 5 h | / | Co, Mn, Al | Sub shrubby peony and bowknot like morphology, the spinel structure | / | [94] |
| $MoS_2$, $Fe^{2+}$ | $MoS_2$, $FeSO_4·7H_2O$ | / | / | / | Mo, Fe, S, O | / | / | [95] |
| $CoS_x$@LDH@Co-NC | Melamine, $Co(NO_3)_2·6H_2O$, $Al(NO_3)_2·9H_2O$, polyvinyl pyrrolidone | Pyrolysis, hydrothermal, sulfidation | 550 °C, 4 h; 800 °C, 1 h | / | Al, Co, C, N, O, S | Carbon nanotube and nanosheet structures | hydroxyl groups, pyrrolic-N/oxygen-sulfur vacancies | [96] |
| $Mo_2C$/$MoO_x$ thin films | Carbon cloth, $MoO_3$ | One-step chemical vapor deposition | 900 °C, 0.5 h | 200 nm | O, C, Mo | Spherical nanoparticles | holes | [97] |
| $Pd_xS_y$ | Palladium acetylacetonate, S, oleylamine, borane tributylamine complex | One-pot oil phase reaction | 320 °C, 0.8 h | 10–60 nm | S, Pd | Cubic/tetragonal structure | / | [98] |
| FeP | $FeCl_3$, $Na_2SO_4$, $NaH_2PO_4·H_2O$ | Phosphidation | 200 °C, 12 h; 350 °C, 2 h | / | Fe, P, O | Fan structure | / | [99] |
| Fe-Co LDH | $Fe(NO_3)_3·9H_2O$, $Co(NO_3)_2·6H_2O$ | Hydrothermal and hydrogen reduction | 200 °C, 24 h | 50–100 nm | Fe, Co, O | Layered structure | OVs | [84] |
| ZnFe-LDH | $Zn(NO_3)_2·6H_2O$, $Fe(NO_3)_3·9H_2O$ | co-precipitation method | 65 °C, 24 h; 600 °C, 2 h | / | Zn, Fe, C, O | Two dimensional layered structure, hexagonal crystals | / | [81] |
| $CuFeS_2$ | CuI, $C_{18}H_{36}$, iron acetylacetonate, $C_{12}H_{26}S$ | Modified chemical colloidal synthesis | 100 °C, 1 h; 230 °C, 1 h | 20–25 nm | Fe, S, Cu, C | Tetragonal structure | / | [100] |
| $FeS_2$ | $FeS_2$ | Sieving and cleaning | 105 °C, <48 h | 5–80 μm | Fe, S | Block structure | / | [101] |
| $CuFeS_2$ NPs | CuCl, $FeCl_3·6H_2O$ | Hydrothermal | 200 °C, 10 h | 15 nm | Cu, Fe, S, C, O | Irregular shape, magnetite phase | / | [102] |

### *2.2. Supported TM Catalysts*

In supported TM catalysts, TM is anchored on the surface of supports in a highly dispersed form through various mechanisms, including physical adsorption, electron transfer, chemical bonding, or interface reconstruction. The primary roles of the support include: dispersing TM active sites to maximize surface area, enhancing stability to prevent sintering or TM leaching, modulating the electronic structure of TM centers, and participating in cooperative catalysis in certain reactions. Common supports for TM catalysts can be categorized as carbon-based supports (e.g., graphene (rGO), carbon nanotubes (CNTs), porous carbon, heteroatom-doped carbons etc.), metal oxides (e.g., $TiO_2$, $CeO_2$, $MnO_2$, $Fe_2O_3$ etc.), molecular sieves/zeolites(e.g., ZSM-5, metal-organic frameworks (MOFs), etc.), sulfides/nitrides(e.g., $MoS_2$, MXenes, etc.) and other advanced supports (e.g., polymers, two-dimensional materials, etc.). In supported TM catalysts, TM in the sizes of nano particle and single-atom on carbon-based supports and metal oxides have been investigated due to their superior catalytic performance and well-defined structures [103,104].

#### 2.2.1. Supported Nanoscale TM Catalysts

In nanoscale catalysts, TM particles are dispersed on the supports as sub-nanometer clusters or nanoparticles, primarily stabilized by metallic bonds (M-M bonds). These nanostructures feature abundant low-coordination atoms on their surfaces, and their electronic structures exhibit continuous energy bands due to the collective interactions of delocalized electrons [105].

The synthesis methods for supported nanoscale TM catalysts primarily includes the impregnation method, sol-gel method, hydrothermal/solvothermal method, co-precipitation method, etc (Table 2). In the impregnation method, the composition and structure of TM catalyst are primarily influenced by factors such as precursor concentration, calcination temperature, and support properties [106]. Through the impregnation method, various catalysts such as CoFe/SBA-15 catalyst [107], n$Fe_3O_4$/rGO composite [108]. Fe@ACFs [9], $CoFe_2O_4$/TNTs [33], FeN-$TiO_2$ [109], CuBN-X [110], and $Fe_2O_3$/g-$C_3N_4$ [111] can be successfully prepared.

The sol-gel method is often used to achieve uniform dispersion of TM oxides nanoparticles on the support surface. The rate of TM hydrolysis to form sol or gel precursor greatly affect the size and dispersion degree of nanoparticles. To this end, Zhang et al. [112] prepared a $CoFe_2O_4$/MWCNTs catalyst with highly dispersed spinel structure by coordinating TM ions with carboxyl groups on multi-walled CNTs and chelating them with citric acid, forming a homogeneous precursor gel. Jorfi et al. [113] obtained highly dispersed $TiO_2$ nanoparticles with sizes below 20 nm by controlling the hydrolysis rate using nitric acid as an acid catalyst. However, sol-gel method is often along with high-temperature pyrolysis process, which may cause support sintering or metal agglomeration.

The hydrothermal/solvothermal method can achieve *in situ* anchoring of TM particles on support under high temperature and liquid-phase environment. It can precisely control over crystal morphology and the size distribution of TM particles by adjusting the solvent polarity, pH, hydrothermal temperature and reaction time. For instance, Li et al. [114] supported micrometer-sized rod-like single crystals Co on MOFs by adjusting the solvent system. Feng et al. [115] finely tuned the size distribution and chemical valence of Pd nanoparticles on $Al_2O_3$ support by optimizing hydrothermal temperature and reaction time. Similarly, catalysts such as Mn-MGO [116], DArGO-Cu [117], Co-Fe PBAs@rGO [118], RSBC-CuO [119], and $Co_3O_4$/Bent [72] were successfully synthesized via hydrothermal/solvothermal methods.

In the co-precipitation method, co-precipitation process ensured uniform mixing of TM and supports, while calcination facilitated the adherence of dispersed TM oxides on support. Some supported TMOx, such as CoMgAl-LDO materials [120], $Ag_2WO_4$/PCN catalyst [121], and $Fe_3O_4$/MWCNTs/PHQ [122] were synthesized using the co-precipitation method.

In addition to above four primary synthesis methods, various alternative strategies have been developed to synthesize the supported nanoscale TM catalysts. For instance, Dong et al. [123] employed a mechano-chemical impregnation approach combined with photochemical initiation to prepared Fe-PAA-g-PP. Lin et al. [124] developed an *in situ* self-combustion method using mesoporous SBA-15 as the support to obtain a bimetallic Fe-Cu/SBA-15 catalyst. Marinescu et al. [125] utilized an ultrasound-assisted approach to prepare an rGO-CoPc composite.

**Table 2.** Structural features and synthesis strategies of representative nano-sized TM catalysts.

| Nano TM Catalysts | Synthesis Methods | Conditions | Precursors | Supports | TM Compositions | TM Size (nm) | Specific Surface Area ($m^2/g$) | References |
|---|---|---|---|---|---|---|---|---|
| CoFe/SBA-15 | Impregnation-calcination | 400–700 °C; 5 h | $Co(NO_3)_2·6H_2O$; $Fe(NO_3)_3·9H_2O$ | SBA-15 | $CoFe_2O_4$ | 4.95 | 506.1 | [107] |
| $Fe_3O_4$/MWCNTs/PHQ | Co-precipitation | Stir: 24 h; 0.1 g $(NH_4)_2SO_4$ | $Fe(NO_3)_3·9H_2O$; $FeSO_4·7H_2O$; 1, 4-benzoquinone | MWCNTs | $Fe_3O_4$ | - | - | [122] |
| Fe@ACFs | Impregnation-calcination | 400–700 °C; Ar; 2 h | $FeCl_3·6H_2O$ | ACFs | $Fe^{3+}$ | - | - | [9] |
| nZVI/BC | In situ reductive | Stir: pH(5.0); $N_2$ | $FeSO_4·7H_2O$; $NaBH_4$ | Biochar | nZVI | 30 | 205.35 | [126] |
| $CoFe_2O_4$/TNTs | Impregnation-calcination | 400–700 °C; 3.5 h | $Co(NO_3)_2·6H_2O$; $Fe(NO_3)_3·9H_2O$; | TNTs | $CoFe_2O_4$ | 6–8 | 120 | [33] |
| Mn-MGO | Hydrothermal reduction | 500 °C; $N_2$; 2 h | $KMnO_4$; | $Fe_3O_4$/GO | $MnO_x$ | - | - | [116] |
| $nFe_3O_4$/rGO | Reverse co-precipitation | Ultrasound: 5 h | $FeSO_4·7H_2O$; $Fe(NO_3)_3·9H_2O$ | rGO | $nFe_3O_4$ | 20 | - | [108] |
| Co-BTC | Solvothermal + co-precipitation method | 120 °C; 24 h | $Co(NO_3)_2·6H_2O$; $H_3BTC$ | BTC | $Co^{2+}$ | - | 0.4279 | [114] |
| $CuFe_2O_4$/MWCNTs | Sol–gel combustion | 400 °C; Ar; 2 h | $Cu(NO_3)_2·3H_2O$; $Fe(NO_3)_3·9H_2O$ | MWCNTs | $CuFe_2O_4$ | 10–25 | - | [112] |
| T@MPAC | Sol-gel+co-precipitation | 400 °C; $N_2$; 2 h | $TiO_2$ | Activated carbon | $Fe_3O_4$; $TiO_2$ | 54 | 572.6 | [113] |
| rGO-CoPc | Ultrasound | 90 °C; 5 h | $CoPc(COOH)_4$ | rGO | CoPc | - | - | [125] |
| MNPs@C | Co-precipitation | 400 °C; 2 h | $FeCl_2·6H_2O$; $FeCl_3·4H_2O$ | Activated carbon | $Fe_3O_4$ | 20 | 572.6 | [18] |
| CuS@N-CNCs | One-step simultaneous precipitation + hydrothermal | 100 °C; 1 h | CNCs | N-CNCs | CuS | 20 | 65 | [71] |
| $Co_3O_4$-g-$C_3N_4$ | Thermal polycondensation | 500 °C; $N_2$; 2 h | $CoSO_4·7H_2O$ | g-$C_3N_4$ | $Co_3O_4$ | 10–50 | - | [127] |
| Pd/$Al_2O_3$ | Hydrothermal | - | Pd | $Al_2O_3$ | Pd | - | - | [115] |
| DArGO-Cu | Hydrothermal | 70 °C; 12 h | $Cu(CH_3COO)_2·H_2O$ | rGO | Cu | - | - | [117] |
| Co@NC | Pyrolysis | 700 °C; 2 h | Melamine; $Co(OAC)_2$ | N-doped CNTs | Co | 50 | 51.9 | [128] |
| nZVI/OMt | Impregnation-calcination | Stir: 3 h | $FeSO_4·7H_2O$; $NaBH_4$ | organo-montmorillonite | nZVI | 50 | - | [69] |
| FeN-$TiO_2$ | Impregnation-calcination | - | $Fe(NO_3)_3·9H_2O$ | N-doped $TiO_2$ | Fe | 18–25 | 51.9 | [109] |
| Fe-Cu/SBA-15 | In situ auto-combustion | 500 °C; 6 h | $Cu(NO_3)_2$; $Fe(NO_3)_2$ | SBA-15 | Fe, Cu metal oxides | - | 565 | [124] |
| Co-Fe PBAs@rGO | Hydrothermal | 180 °C; 10 h | $CoCl_2·6H_2O$; $K_3[Fe(CN)_6]$ | rGO | Co-Fe Prussian blue | 20 | 186.84 | [118] |
| Fe-PAA-g-PP | Graft polymerization + coordination | - | $FeCl_3·6H_2O$ | PAA-g-PP | $Fe^{3+}$ | - | - | [123] |
| CuO/$MnFe_2O_4$ | Incipient wetness impregnation | 180 °C; 24h | $Cu(NO_3)_2·3H_2O$; $Mn(NO_3)_2·4H_2O$; $Fe(NO_3)_3·9H_2O$ | $MnFe_2O_4$ | CuO | 50–200 | 8.298 | [129] |
| $MnFe_2O_4$/MX | Sol-Gel | 180 °C; 24h | $Mn(NO_3)_2·4H_2O$; $Fe(NO_3)_3·9H_2O$ | MX | $MnFe_2O_4$ | 50–100 | 389 | [130] |
| $Co_3S_4$@GN; CoS@GN | MOF-templated ligand exchange | 600 °C; $N_2$; 2 h | ZIF-67; $Co(NO_3)_2·6H_2O$ | Graphene | $Co_3S_4$; CoS | 10–40 | 75 | [70] |
| DMG | Double-network hydrogel template | 800 °C; Ar; 2 h | $FeSO_4$; FeOOH | Three-dimensional graphene hydrogel | FeS | 300–400 | 218.8 | [131] |
| CuBN-X | Immersion-calcination | 400 °C; Ar; 5 h | $Cu(NO_3)_2·3H_2O$ | h-BN | CuO | - | 13.1 | [110] |
| RSBC-CuO | Hydrothermal synthesis | pH(8); 170 °C; 7 h | $Cu(NO_3)_2·3H_2O$ | RSBC | CuO | 200–300 | 197.84 | [119] |
| $Ag_2WO_4$/PCN | Co-precipitation | 550 °C; 4 h | $AgNO_3$; $Na_2WO_4$ | P-doped graphitic carbon nitride | $Ag_2WO_4$ | - | 61.43 | [121] |
| Co@CNFs-Ag | Electropspinnin + chemical reduction | 1000 °C; 1 h | $Co(NO_3)_2$; $AgNO_3$ | CNFs | Co; Ag | 20–30; 5–10 | 143.49 | [132] |
| PZBC800U | Pyrolysis | 800 °C; $N_2$; 1.5 h | $Fe(OH)_3$; Urea | Diatomite-modified biochar | FexN | 300 | 334.34 | [133] |
| $Fe_2O_3$/g-$C_3N_4$ | Immersion-calcination | 350 °C; 2 h | $FeCl_3·6H_2O$ | Carbon cloth | $Fe_2O_3$/g-$C_3N_4$ | - | - | [111] |
| $Co_3O_4$/Bent | HTC + pyrolysis | 550 °C; 2 h | $Co(NO_3)_2·6H_2O$ | Organically modified bentonite | $Co_3O_4$ | - | 51.78 | [72] |

2.2.2. SA-TMCs

In SA-TMCs, the TM atoms are anchored on the surface or defect sites of the support (e.g., oxides, nitrogen-doped carbon, or molecular sieves) via coordination bonds (e.g., M-O, M-N, or M-C), forming a well-defined TM-support coordination structure. The electronic structure of the TM centers exhibits discrete energy levels due to their atomic dispersions, and the TM sites are highly polarized. Notably, the electronic states of TM atoms are critically modulated by the local coordination environment of the support. Based on the local coordination environment, SA-TMCs can be categorized into: N-coordination (e.g., M-$N_4$ moieties, prevalent in carbon-based supports), O-coordination (e.g., M-O bonds in metal oxides), S/P-coordination (e.g., sulfide or phosphide supports), and mixed coordination (e.g., M-$N_2O$, M-$N_3S$) (Table 3). The coordination number typically ranges from 2 to 6, which directly governs the d-band electronic structure of the TM centers and thereby their catalytic activities [134,135]. Carbon-based materials including graphitic carbon nitride (g-$C_3N_4$), MOF-derived carbons, and rGO are widely employed as SA-TMCs supports owing to their high surface area, tunable porosity, and superior conductivity.

In SA-TMCs, to achieve high dispersion of TM atoms, stable anchoring, and controllable coordination structures, the following synthesis methods include pyrolysis-based methods, solution-phase coordination, post-modification strategies, *in situ* templating, and auxiliary construction approaches have been developed.

In the pyrolysis-based methods, the co-pyrolysis process of TM sources and organic compounds often leads to the anchor of TM atoms within the carbon matrix, forming stable coordination structures. The pyrolysis conditions, precursor composition, and thermal decomposition pathways significantly influence the site type and electronic structure. This method has been widely applied in the successful synthesis of Fe/N–SAC materials containing both Fe-$N_4$ and Fe-Fe dual-center structures [136], FeCo-DAC [137], Mn-$N_5$ [134], and SA-Co-LDH [138].

The solution-phase coordination methods typically rely on chelation reactions between TM ions and organic frameworks or oxygen-containing functional groups (e.g., pyridinic N, carboxyl, or hydroxyl groups). Subsequent drying or moderate-temperature treatment fixes the coordination structure. For example, $Cu_{SA}$/Ace-COF was synthesized by introducing $Cu^{2+}$ into a COF structure with rich pyridinic nitrogen sites, forming a stable Cu-$N_2$ configuration [8]. Similar strategies have been employed for constructing Co-TPML [139], $Co_1$-GO membrane [140], and $Ru_1O_x$/ZnO [141].

Post-synthetic modification involves introducing TM precursors onto pre-constructed carbon materials or porous frameworks, followed by thermal treatment or reduction to achieve stable TM anchoring. This method offers high flexibility for tuning the spatial distribution or electronic environment of TM active sites. This strategy has been applied to construct SA-TMCs such as $Cu_1$/NG [142], FeCo-NCB [143] and FeSA-N-CNT [59].

*In-situ* templating relies on structural directing agents (e.g., Zn, $NH_4Cl$, $SiO_2$) that evaporate or decompose during pyrolysis, forming transient templates to regulate pore structures, carrier defects, and site distribution. This enables the anchoring of high-density, uniformly structured single-atom TM sites. For example, the $NH_4Cl$-induced vapor-phase etching of the carbon framework, combined with a "4 + 1" coordination modulation strategy, successfully constructed Fe-$N_5$ sites in SA-Fe$N_5$ [143]. This approach has also been adapted for the synthesis $Co_{SA/ZnO}$-ZnO [144] and $Fe_1$/CN [145].

Besides, auxiliary methods including electrodeposition, ball milling, self-assembly, and wet impregnation are often combined with primary strategies to fine-tune coordination structures or improve loading homogeneity. These auxiliary methods have been applied to the synthesis of Fe-SA/MXene [146], Co-MCAMeIm [147] and Mn-ISAs@CN [148].

**Table 3.** Structural features and synthesis strategies of representative SA-TMCs.

| Transition Metal Single-Atom Catalysts | Synthetic Methods | TM Precursors | Conditions | Single Atom | Supports | Coordination Structure | References |
|---|---|---|---|---|---|---|---|
| Fe/N-SAC | Template-assisted pyrolysis | $Fe(acac)_3$ | 900 °C 2 h, Ar | Fe | N-doped carbon | Fe-$N_4$, Fe-Fe (2Fe-$N_4$), $Fe_2$-$N_6$ | [136] |
| $Ru_1O_x$/ZnO | Impregnation-calcination | $RuCl_3$ | 300 °C 2 h, Ar | Ru | ZnO | Ru-$O_5$ (single Ru oxide) | [141] |
| $Co_1$CNCl/S | Salt-template pyrolysis | $CoSO_4$ | 900 °C 2 h, Ar | Co | N-doped carbon nanosheets | Cl-Co-$N_4$-S | [149] |
| $Cu_{SA}$/Ace-COF | Post-synthetic modification | $CuCl_2{\cdot}2H_2O$ | 180 °C thermal fixation for 2 h | Cu | Covalent organic framework (Ace-COF) | Cu-$N_2$ | [8] |
| $Co_{SA/Zn,O}$-ZnO | Hydrothermal + annealing | $Co(CH_3COO)_2{\cdot}4H_2O$ | 150 °C, 20 h, hydrothermal | Co | ZnO (nano-island structure) | Co-O-Zn | [22] |
| FeCo-NCB | Wet impregnation + calcination | $FeCl_3{\cdot}6H_2O$ + Co $(NO_3)_2{\cdot}6H_2O$ | pH = 13, 120 °C, 12 h, hydrothermal | Fe, Co | N-doped carbon black | Fe-$N_4$, Co-$N_4$ | [150] |
| pFe-SAC | Template-assisted pyrolysis | $FeCl_3{\cdot}6H_2O$ | 800 °C 2 h, $N_2$ | Fe | Porous N-doped carbon | Fe-$N_5$ | [151] |
| Nv-rich Fe-SACs | Template-assisted calcination and exfoliation | $FeCl_3{\cdot}6H_2O$ | 550 °C 4 h + 620 °C 4 h, $N_2$ | Fe | g-$C_3N_4$ | Fe-$N_4$ with adjacent nitrogen vacancy (Nv) | [152] |
| Fe/Co/Cu-SAC | Pyrolysis | $FeCl_2$, $CoCl_2$, CuCl | 550 °C 1 h + 950 °C 1 h, $N_2$ | Fe, Co, Cu | N-doped carbon | Fe/Co/Cu-$N_4$-C | [153] |
| CuBN-HCMs | Self-assembly + pyrolysis | $Cu(NO_3)_2{\cdot}3H2O$ | 800 °C 2 h, Ar | Cu | B, N co-doped hollow carbon microspheres | Cu-$N_4$ regulated by B atoms | [154] |
| CM-UCNv-Fe | Defect engineering and pyrolysis | $FeCl_3{\cdot}6H_2O$ | 500 °C 2 h, air | Fe | g-$C_3N_4$ with Nv defects | Fe-$N_4$ with enriched electron density | [155] |
| $Ru_1$/NC | Template-assisted pyrolysis | $RuCl_3$ | 550 /650–850/950 °C 2 h, $N_2$ | Ru | N-doped carbon | Ru-$N_2$ | [87] |
| Fe-SAC-H/CF | One-step pyrolysis | $Fe(NO_3)_3{\cdot}9H_2O$ | 550 °C 2 h, Ar | Fe | Carbon felt (CF) | Fe-$N_4$ | [156] |
| SA-$FeN_5$ | "4 + 1" strategy pyrolysis | Ferric acetylacetonate | 550 °C 4 h, Ar | Fe | g-$C_3N_4$ | Fe-$N_5$ | [143] |
| FeCo-DAC | MOF-derived pyrolysis | Co $(NO_3)_2{\cdot}6H_2O$ + Fe $(acac)_3$ | 900 °C 2 h, $N_2$ | Fe-Co | N-doped carbon | FeCo-$N_6$ | [137] |
| FeSA-MNC | Template-assisted pyrolysis | $Fe(acac)_3$ | 300 °C 2 h + 900 °C 5 h, $N_2$ | Fe | Mesoporous N-doped carbon | Fe-$N_4$ | [157] |
| Fe-PNC | Template-assisted pyrolysis | $Fe(NO_3)_3{\cdot}9H_2O$ | 1000 °C 1 h, Ar | Fe | N,P-codoped carbon | Fe-$N_4P_2$ | [158] |
| Co-MCAMeIm | Molecular self-assembly + pyrolysis | $Co(NO_3)_2{\cdot}6H_2O$ | 550 °C 2 h, $N_2$ | Co | g-$C_3N_4$ | Co-$N_4$ | [147] |
| $MnN_5$ | Pyrolysis | $Mn(acac)_3$ | 550 °C 4 h, Ar | Mn | g-$C_3N_4$ | Mn-$N_5$ | [134] |
| SA-Co-LDH | Ion exchange + calcination | TCPP-Co | 550 °C 2 h, $N_2$ | Co | Layered double hydroxide (Mg/Al-LDH) | Co-$N_4$ | [152] |
| Fe-N-C | Wet impregnation + pyrolysis | Ferrous acetate | 700 °C 2 h, $N_2$ | Fe | N-doped carbon | Fe-$N_4$ (pyridinic N) | [65] |
| Mn-ISAs@CN | MOF-template pyrolysis | $Mn(acac)_3$ | 900 °C 3 h, Ar | Mn | N-doped porous carbon | Mn-$N_4$ | [148] |
| $Fe_1$/CN | Supermolecule-assisted pyrolysis | $FeCl_3{\cdot}6H_2O$ | 550 °C 2 h, Ar | Fe | g-$C_3N_4$ | Fe-$N_4$ | [42] |
| $Cu_1$/NG | Chemical vapor deposition (CVD) | $CuCl_2$ | 900 °C, $N_2$, $NH_{3-x}$ (from dicyandiamide) | Cu | N-doped graphene | Cu-$N_4$ | [142] |
| Co-SA | MOF-template pyrolysis | $Co(NO_3)_2{\cdot}6H_2O$ | 900 °C 2 h, Ar | Co | N-doped carbon | Co-$N_{2+2}$ | [159] |
| Co-TPML | Solution-phase coordination + pyrolysis | $Co(NO_3)_2{\cdot}6H_2O$ | 800 °C 2 h, $N_2$ | Co | Tetrapyridomacrocyclic ligand-derived carbon | Co-$N_4$ | [139] |
| SA-Fe-NC | Cascade anchoring + pyrolysis | $Fe(NO_3)_3{\cdot}9H_2O$ | 800 °C 2 h, $N_2$ | Fe | N-doped porous carbon | Fe-pyridinic $N_4$ | [160] |
| Fe-SA/$Mo_2TiC_2T_x$ | Electrochemical deposition + etching | $FeCl_3{\cdot}6H_2O$ | CV electrodeposition (25 cycles, −0.5~1.2 V vs Ag/AgCl, 20 mV/s) | Fe | Mo vacancy-rich MXene ($Mo_2TiC_2T_x$) | Fe-$O_6$ | [146] |
| CuSA-NC | Template-assisted pyrolysis | $Cu(NO_3)_2{\cdot}3H_2O$ | 800 °C 2 h, $N_2$ | Cu | N-doped carbon nanosheets | Cu-$N_2$ (unsaturated) | [16] |
| FeSA-N-CNT | High-energy ball milling + pyrolysis | $Fe(acac)_3$ | 500 °C 3h + 700 °C 2 h, $N_2$ | Fe | N-doped CNT | Fe-$N_4$ | [59] |
| $Co_1$-GO | Wet chemical reduction + vacuum filtration | $CoCl_2{\cdot}6H_2O$ | 80 °C stirring 2 h (with VC), vacuum filtration | Co | Graphene oxide membrane | Co-$O_{2-3}$ | [140] |
| Co-$N_4$-C | Wet impregnation + pyrolysis | $Co(NO_3)_2{\cdot}6H_2O$ | 550 °C 1h + 950 1 h, $N_2$ | Co | N-doped biomass-derived carbon | Co-$N_4$ | [135] |

## 3. Activation Mechanisms

### *3.1. General Mechanism of PMS Activation*

In the TM-activated PMS-based AOPs, $SO_4^{\bullet-}$, $^{\bullet}OH$, singlet oxygen ($^1O_2$) and unstable high-valent TM (e.g., ($Fe^{IV}$, $Co^{III}$, $Mn^{IV}$) have been identified as key ROS. Moreover, some complexed PS with TM catalysts (TM-PS*) is often believed as the active species that can oxidize some ECs through direct electron transfer mechanism. Besides, the structure and properties of ECS as well as the composition of coexisting substances can affect the type and formation pathway of ROS [153]. Here, the mechanisms of ROS generation on different structures of TM catalysts are intensively discussed. The ROS generation depends on the interaction mode between PS and TM catalysts. Generally, the PS activation by TM catalysts involves three mechanisms: single electron transfer, oxygen transfer and complex mechanisms.

#### 3.1.1. Single Electron Transfer Mechanism

In single electron transfer mechanism, when PS interacts with TM catalysts, the unfilled d orbitals of TM undergo inner-sphere coordination to form a $Me^{n+}$-$OOSO_3$ complex [136,155,161]. Subsequently, outer-sphere electron transfer occurs from the $Me^{n+}$ active sites of the catalyst to PS, leading to the cleavage of the O-O bond and the generation of $SO_4^{\bullet-}$. This radical can further react with water to produce $^{\bullet}OH$, ultimately yielding $SO_4^{2-}$ and $Me^{(n+m)+}$ as final products [162,163]. Conversely, PMS oxidation at the $Me^{(n+m)+}$ site proceeds via inner-sphere electron transfer, forming $Me^{n+}$ and $SO_5^{\bullet-}$. The $SO_5^{\bullet-}$ intermediate rapidly undergoes self-reaction to generate $^1O_2$. Because electron transfer process from PS to $Me^{(n+m)+}$ site requires the strong potential difference, the reactivity of $M^{(n+m)+}$ toward PS too weak to sustain the reaction [164–166].

#### 3.1.2. Oxygen Atom Transfer Mechanism

Oxygen atom transfer mechanism is also be called as two-electron transfer mechanism. A typical oxygen transfer process includes that TM (e.g., $Co^{2+}$, $Fe^{2+}$, $Cu^{2+}$) firstly coordinates with PS to form inner-sphere complexes via direct ligand sharing [167]. Then, electrons from the TM to PS occurs through the coordination bridge (e.g., the O-O bond of PS), resulting in O-O bond cleavage and the generation of $Me^{n+2}$ = O species. The $Me^{n+2}$ = O species formation involves two steps. Step 1, PS binds to the TM ion through oxygen atoms of its peroxy group (-O-$O^-$), forming an inner-sphere complex ($Me^{n+} + HSO_5^- \rightarrow [Me^{n+} - OOSO_3]^- + H^+$); Step 2, the two electrons of the TM in 3d orbitals transfer to the σ* antibonding orbital of PS via the -O-$O^-$ bridge, inducing heterolytic O-O bond cleavage. Concurrently, the vacant 3d orbitals of the TM accept lone pair electrons from O, forming a $Me^{n+2}$ = O double bond ($[Me^{n+}{-}OOSO_3]^- \rightarrow Me^{n+2} = O + SO_4^{2-}$). The resultant $Me^{n+2}$ = O species serves as a highly reactive intermediate that directly inserts oxygen atoms into specific bonds of contaminants (e.g., C=C, C-H, S-H) via electrophilic attack or concerted insertion mechanisms, yielding oxidized products such as epoxides, alcohols, and ketones.

#### 3.1.3. Complex Mechanism

The complex mechanism is also known as the direct electron transfer mechanism (ETP). In the complex mechanism, the interaction of TM with PS to form activated TM-PS* complex, which may directly oxidize contaminants as a highly reactive intermediate. The high activity of TM-PS* complex is often attributed to two reasons. On the one hand, the d orbitals of TM (such as $Co^{2+}$, $Mn^{2+}$) react with the -O-O- of PS to form σ coordination bonds. Electrons are fed back from the O-O σ* antibonding orbital of PS to the empty d orbitals of the TM, resulting in a decrease in the electron cloud density of the O-O bond and a weakening of the bond energy (from ~140 kJ/mol to ~80 kJ/mol). On the other hand, after the formation of σ coordination bonds between TM and PS, the electron density of the TM is partially transferred to PS through ligand-metal charge transfer, causing the transforms of -O-O- into a more electrophilic "$O^+$-$O^-$" structure.

The TM-PS* complex can oxidize pollutants through the following two ways: (1) electrophilic oxygen transfer. The "$O^+$" in the complex directly attacks the electron-rich groups of the contaminants (such as benzene rings, C=C double bonds); (2) electron abstraction: The complex as a whole obtains electrons from the contaminants (such as phenols → phenoxyl radicals).

### *3.2. Activation Mechanism by Homogeneous TM Catalysts*

In homogeneous TM catalysis, the unfilled d orbitals of TM coordinate with water molecules or other ligands to form water-soluble complexes. When PS contacts with TM, the unfilled d orbitals of TM coordinate with PS to

form $Me^{n+}$-$OOSO_3$ complex by ligand substitution reaction. Subsequently, the radicals (e.g., $SO_4^{\bullet-}$, $^{\bullet}OH$) or $^1O_2$ may be generated by single electron transfer mechanism [161,162], along with the recycle of $Me^{(n+m)+}/Me^{n+}$ (Figure 3) [166,168].

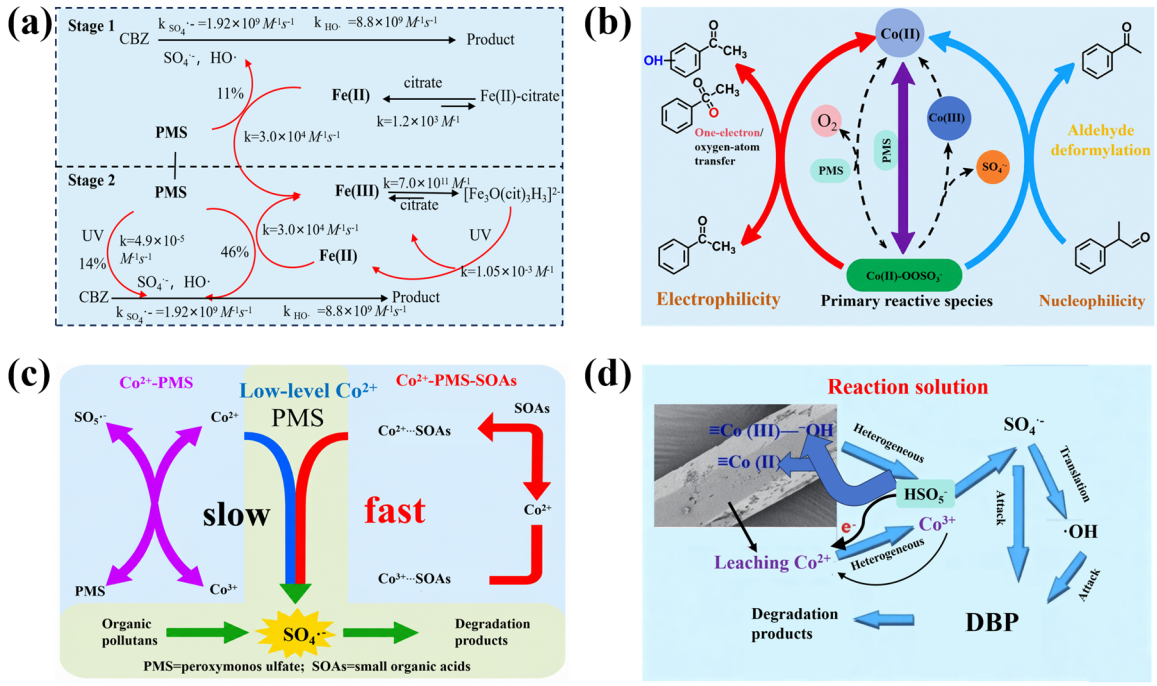


**Figure 3.** Schematic diagram of activation mechanism by representative homogeneous TM catalysts. (**a**) CBZ degradation by the $Fe^{2+}$/citrate/UV/PMS system [169]; (**b**) $Co^{2+}$-catalyzed PMS activation process [163]; (**c**) Small organic acids (SOAs) enhanced PMS activation by $Co^{2+}$ [168]; (**d**) PMS activation by Co-BTC catalysts [114]. (Adapted from the corresponding reference)

In recent years, through the MPSO probe assay, $^{18}O$ labeled water experiments, and Raman spectroscopy analysis, it has been confirmed that homogeneous TM ions can also form unstable high-valent TM ions (e.g., $Fe^{IV}$, $Co^{III}$, $Cu^{III}$, etc.) when interacting with PS [169]. For example, Li et al. [163] identified that in the $Co^{2+}$/PMS system, a fraction of the $Co^{2+}$-PMS complex at higher pH decomposes to generate $Co^{3+}$ and $SO_4^{\bullet-}$. However, the transfer of electrons in the formation mechanism of unstable high-valent TM is unclear. In some reports, two electron transfer during PMS activation resulted in the formation of unstable high-valent TM conversion [170]. Gao et al. [171] found that the addition of nitrogen-containing ligands (e.g., EDTA, NTA) into $Mn^{2+}$/PMS system, the formation of $Mn^V$ species was through two-electron transfer mechanism. Gong et al. [162] proved the formation of $Fe^{IV}$-oxo intermediate in the $Fe^{2+}$/PMS system under acidic conditions (such as pH3) through a two-electron transfer process using $^{18}O$ isotope labeling experiments. On the contrary, other reports believe that $Fe^{IV}$-oxo mainly produced from $Fe^{3+}$ through a single electron transfer process. For instance, Yang et al. [172] employed the complexes of $Fe^{3+}$ with the biodegradable picolinic acid (PICA) to activate PMS. The key intermediate was identified as a PICA-$Fe^{3+}$-$OOSO_3^-$ complex, which undergoes O-O homolysis to yield $Fe^{IV}$-oxo without the involvement of commonly invoked $Fe^{2+}$.

In homogeneous activation processes, TM ions can serve as electron-transfer mediators, directly oxidizing organic contaminants via electron transfer. For instance, Gong et al. [162] identified a $Co^{2+}$-PMS* complex during PMS activation by aqueous $Co^{2+}$ ions under acidic conditions. This $Co^{2+}$-PMS* complex could directly oxidize organic contaminants. Li et al. [163] further demonstrated that in the $Co^{2+}$/PMS system, the primary reactive species was the $Co^{2+}$-$OOSO_3^-$ complex, which exhibited dual reactivity, facilitating both oxygen-atom-transfer and one-electron-transfer pathways.

### *3.3. Activation Mechanism by Unsupported TM Oxides*

The PS activation by heterogeneous TM is similar to homogeneous systems but involves solid-liquid interface reactions. PS is activated through surface TM sites and regulated by TM species, valence states, surface defects, and interface microenvironment. Zero valent TM catalysts, insoluble TM metallization, and TM oxides are usually used for PS activation. The PS activation by zero valent TM catalysts (e.g., $Fe^0$ and $Cu^0$) for ROS

generation are mainly through single electron transfer mechanism. Unlike other TM catalysts, zero valent TM catalysts can directly transport electrons to PS leads to $SO_4^{\bullet-}$ formation and accelerate the cycles of $Me^{(n+m)+}/Me^{n+}$ [173].

In the metallization (e.g., CoP, $Cu_3P$, FeP, CuS, FeS, $FeS_2$, pyrite, FeOCl etc.) activated PS system, the interaction of the redox pair of $Me^{(n+m)+}/Me^{n+}$ with PS mainly contribute the ROS generation. However, some metallization, the free-metals (e.g., S, P, B) possesses the electron-donating ability due to its low valence, which can also activate PS and regenerate $Me^{n+}$ from $Me^{(n+m)+}$, promoting the ROS generation [100]. Compared with the previous two types of catalysts, TM oxide catalysts have more applications, their structures are more complex and variable, and their activation mechanisms are also more complicated. This work mainly discusses the activation mechanism of TM oxides.

### 3.3.1. General Activation Mechanism by TM Oxides

The PS activation by TM oxides for ROS generation can be categorized into three main pathways (Figure 4).

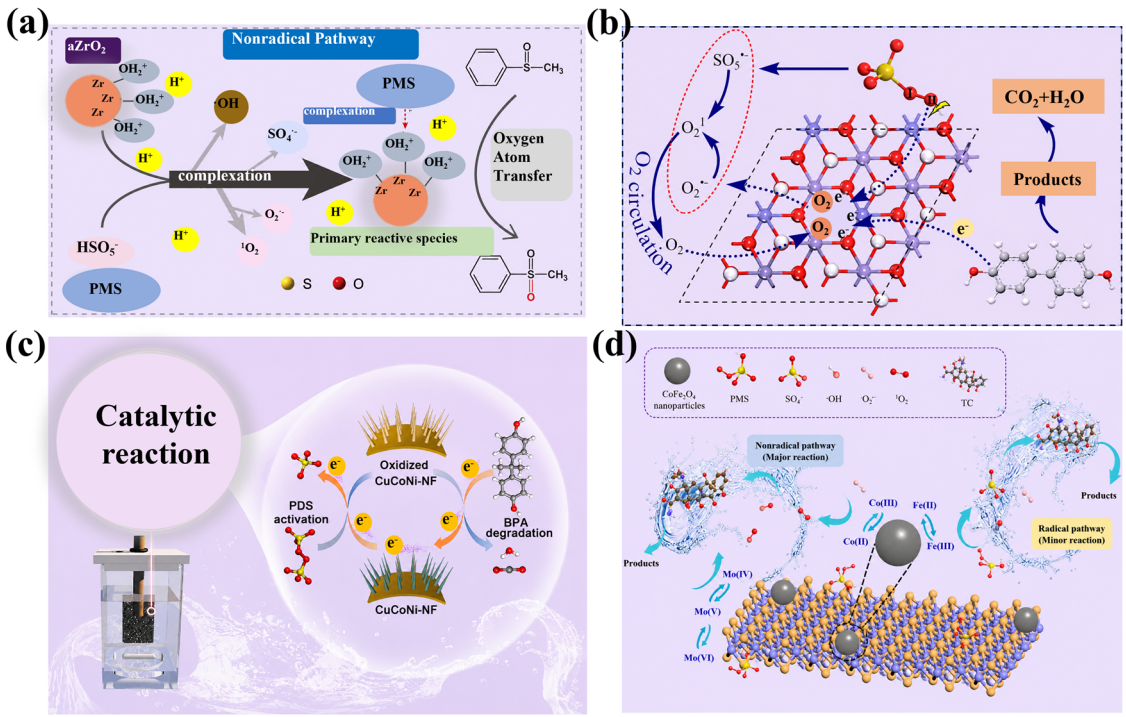


**Figure 4.** Schematic diagram of activation mechanisms by representative TM oxide catalysts. (**a**) $ZrO_2$-induced PMS activation [174]; (**b**) Nonradical oxidation of BPA by the 200Fe-Co LDH/PMS system [84]; (**c**) PDS activation by CuCoNi−NF [86]; (**d**) PMS activation by $CoFe_2O_4$@$MoS_2$ [175]. (Adapted from the corresponding reference)

(1) Surface electron transfer. The surface-active sites (≡$Me^{n+}$) activate PS through single-electron or oxygen-atom (two-electron) transfers, generating radicals ($SO_4^{\bullet-}$, $^{\bullet}OH$) and unstable high-valent TM species. The redox pair of $Me^{(n+m)+}/Me^{n+}$(e.g., $Mn^{IV}/Mn^{III}$, $Mn^{III}/Mn^{II}$, $Cu^{III}/Cu^{II}$, $Co^{III}/Co^{II}$, $Fe^{III}/Fe^{II}$, $V^{IV}/V^{V}$) meditated this activation process [71,176,177]. For example, in the $Co_3O_4$ nanosheets-activated PMS system, single-electron transfer induces the generation of $SO_4^{\bullet-}$ and $^{\bullet}OH$ [174].

(2) Surface complex. The TM oxides surface basic sites promote the formation of surface-bound complex (≡Me–PS*), oxidizing contaminants via interfacial electron transfer without radical intermediates [170,178,179]. For example, the abundant hydroxyl groups of amorphous zirconium dioxide ($aZrO_2$) promote the adsorption of $HSO_5^-$ driven by Coulomb force, then form $Zr^{IV}$-PMS* complex caused the deviation of the negative charge from $Zr^{IV}$ metal sites to the oxidant. It can directly oxidize contaminant via electron transfer from contaminants to the complex [174].

(3) Defects and surface groups meditated $^1O_2$ generation. OVs in metal oxides can regulate the electron structure and activity of the surrounding sites, greatly affect the binding behavior between PS and TM oxides and further induce $^1O_2$ generation by produce superoxide radicals ($O_2^{\bullet-}$) intermediates. OVs plays dual roles: to adsorb and heterolytically cleave PS to yield $^1O_2$, and to facilitate the regeneration of active TM sites, sustaining catalytic activity [170,180]. Wang et al. [181] constructed a $MnO_2$ with OVs promoted the

generation of $^1O_2$. In some TM-based catalyst with hydroxyl group catalyzed PMS system, both the conversion of $O_2^{\bullet-}$ and the self-reaction and hydrolysis of $SO_5^{\bullet-}$ contributed to $^1O_2$ generation. Moreover, unstable high-valent metals or reactive oxygen atoms induce PMS decomposition also produce $^1O_2$ [170].

Compared with single TM, the double or multiple TM have more metal types, more complex crystal structure, the increased surface hydroxyl groups, and richer OVs. The mechanisms of the pathways of ROS generation in double or multiple TM -activated PS process become more complex.

### 3.3.2. Activation Mechanism by LDHs

As mentioned above, LDHs have unique hydrotalcite-like structural with the general formula of $Me^{II}_{1-x}Me^{III}_x(OH)_2]^{x+}\cdot(A^{n-})_{x/n}\cdot mH_2O$. LDHs exhibit excellent PS activation performance due to their tunable bimetallic synergistic effects, abundant surface hydroxyl groups, and defect-mediated electronic regulation. In addition to the previously mentioned surface electron transfer, OVs and surface group-induced ROS generation, the activation mechanism of LDHs also includes that (a) electron transfer between $Me^{II}/Me^{III}$ and PS induces ROS generation, while the redox cycling of dual metals (e.g., $Co^{II}/Co^{III}$ and $Fe^{II}/Fe^{III}$) facilitates continuous electron transfer; (b) high-valent TM (e.g., $Co^{III}$) in the LDH layers can directly decompose $HSO_5^-$ to produce $^1O_2$ [182,183].

For example, in MnFe-LDH containing $Mn^{II}$, $Mn^{III}$, $Fe^{II}$ and $Fe^{III}$/PMS system, the $Fe^{II}$ sites may give an electron to the $Mn^{III}$ sites and transform into $Fe^{III}$ and $Mn^{II}$ sites [184]. Zhang et al. [185] demonstrated that in the 200Fe-Co LDH activated PMS system, the OVs promoted $^1O_2$ formation in two ways: (1) PMS donated an electron to OVs (rendered electron-deficient by $O_2$), generating $^1O_2$, and (2) affinity of OVs for O localized $^1O_2$, enhancing $O_2$ accumulation.

### 3.3.3. Activation Mechanism by Perovskites Oxides

In the spinel perovskites $ABO_3$, the A- and/or B-site cations can be appropriately replaced by a foreign cation, which can tailor their physiochemical and electronic properties. Since they have tunable electronic structure of B-site metals, abundant OVs, and a stable crystalline framework, perovskite oxides have emerged as an attractive candidate for the PS activation. In perovskites, the valence cycling of TM can be accelerated due to the synergistic effects of bimetal. In bimetallic perovskites, the B-site TM (e.g., Co, Mn, Fe, Cu) exhibits the synergetic electron-transfer between different TMs. Their variable valence states (e.g., $Co^{III}/Co^{II}$, $Mn^{IV}/Mn^{III}$) facilitate electron transfer with PS, activating it to generate $SO_4^{\bullet-}$ and $^{\bullet}OH$ [186]. He et al. [76] demonstrated that strategic Ni substitution at the B-site of $LaCoO_3$ perovskite facilitated the crucial $Co^{III}/Co^{II}$ redox cycle vital for sustained radical generation, significantly enhancing PMS activation. Besides, perovskites possess abundant OVs, which also regulate the electron structure and activity of the surrounding sites, promoting PMS activation [187].

In addition to the valence cycling of TM and electron transfer mediated by OVs serve as the core driving forces, the lattice oxygen and doping may also promote PS activation. The lattice oxygen in perovskites may be released as surface-active oxygen species (e.g., $O^-$ or $O_2^{2-}$), which subsequently reacts with PS to directly generate $^1O_2$ [68,188,189]. In the strategy for doping, doping at A-sites (e.g., La, Sr) or B-sites can modulate the perovskite's band structure and electron mobility, optimizing PS activation efficiency. For instance, in $LaCo_{1-x}Cu_xO_3$ perovskite, B-site substitution by copper could form a bimetallic system and facilitate the $Co^{III}/Co^{II}$ redox cycle, enhancing PMS activation [76].

### 3.3.4. Activation Mechanism by Spinel Oxides

The enhanced PS activation of spinel oxide $AB_2O_4$ is also attributed to the synergistic effect of A-site and B-site TM, abundant OVs and the flexible cation substitution for surface modification, which is similar to the perovskites and LDHs.

Firstly, the A-site and B-site TM facilitate efficient electron transfer through valence cycling, lowering the activation energy barrier for PS [190]. For example, in the $CoMn_2O_4$ spinel oxide, the rich M-OH groups (M = Co or Mn) react with PMS, generating $SO_4^{\bullet-}$ and $^{\bullet}OH$. The $Co^{III}/Co^{II}$ ($E^0$ = 1.81 V) couple is efficiently reduced by $Mn^{III}/Mn^{II}$ ($E^0$ = 1.51 V) and $MnO_2/Mn_2O_3$ ($E^0$ = 0.15 V), enabling $Co^{II}$ regeneration [191].

Secondly, the abundant OVs in spinel oxides not only directly participate in PS activation by serving as electron donors but also promote valence cycling of B-site metals, sustaining catalytic activity. For instance, in CuFeMnO spinel oxides activated PMS system, the OVs and unsaturated metal sites adsorb and activate PMS, generating unstable high-valent species ($Cu^{III}$, $Fe^{IV}$, $Mn^{V}$) and $^{\bullet}OH$ (derived from $Cu^{III}$) [192].

Finally, the substitution of A-site or B-site TM with foreign cations allows precise tuning of surface acidity/basicity to enhance PS adsorption [63]. Huang et al. [192] revealed that compared to $CuFe_2O_4$, Mn

incorporation in CuFeMnO redistributes electron density, creating a charge density gradient at symmetry-breaking centers, further boosting catalytic activity.

### *3.4. Activation Mechanism by Supported Heterogeneous TM Catalysts*

The active sites in supported heterogeneous TM catalysts typically consist of isolated metal atoms or highly dispersed clusters/nanoparticles anchored on the support. The support plays crucial roles in stabilizing TM clusters/nanoparticles clusters/nanoparticles or single-atom sites, modulating electronic properties through synergistic effects, and preventing TM leaching. Notably, the activation mechanisms of PS by supported nano-TM catalysts and SA-TMCs exhibit substantial differences. These distinctions primarily arise from variations in atomic-level dispersion of active sites, electronic configurations, and the unique interface microenvironments characteristic of each catalyst type.

#### 3.4.1. Activation Mechanism by Nano-TM Supported Catalysts

In nano-TM in supported catalysts systems, certain supports play additional roles beyond merely dispersing and stabilizing nano-TM. These supports actively participate in the reaction process through their intrinsic physicochemical properties, thereby modifying or enhancing ROS generation (Figure 5). This section focuses specifically on support-enhanced activation mechanisms of PS.

(1) Dispersing TM clusters/nanoparticles and reducing the release of TM ions. Some supports have a large specific surface area, which can disperse TM ions. The functional groups on the carriers can fix TM ions through coordination or ion exchange reactions, thereby reducing their leaching [69,124,125]. For example, in the $CoFe_2O_4$/TNTs, titanate nanotubes (TNTs) support could promise small size and good dispersion of $CoFe_2O_4$ nanoparticles. Besides, TNTs could exchange partial free metal cations released from the reaction process and promise less metal ion leaching as compared to sole spinel ferrites [33].

(2) Enhancing electron transfer. Conductive supports (e.g., rGO, CNTs) facilitate electron transfer between TM centers and PS, effectively reducing the reaction's kinetic energy barrier [126]. For instance, in ferric oxide supported on carbon, activated carbon acts as an excellent electron transfer support, facilitating electron transfer and enhancing the activity and stability of the catalyst [18]. In the $CuFe_2O_4$/MWCNTs, MWCNTs not only served as a support to provide a large number of loading sites for $CuFe_2O_4$, but also exhibited unique properties that facilitate electron transfer [112].

(3) Surface functional groups. Carbon defects (including vacancies and edge sites) function as electron traps that promote PS adsorption and facilitate the formation of dual active centers. Oxygen-containing functional groups (-COOH, -OH) on carbon surfaces enhance supports hydrophilicity, promoting PS enrichment at the interface. Additionally, acidic functional groups on carbon may assist in O-O bond cleavage via proton transfer mechanisms [71]. For example, in the $Fe_3O_4$/MWCNTs/PHQ catalysts, the quinone substances in PHQ were prone to react with $Fe^{III}$, forming a cycle that continuously generates $Fe^{II}$, thereby continuously activating PS [122]. Yan et al. [108] found that in $nFe_3O_4$/rGO composite, the C-OH and COOH groups on the rGO surface released organic free radicals, promoting the electrons transfer from rGO to PS and accelerating the activation process of PS.

(4) Enhancing adsorption and mass transfer of reactants. The microporous/mesoporous structure of supports can confine reactants within localized high-concentration regions, thereby improving mass transfer efficiency. For example, in the iron loaded activated carbon fibers (ACFs), the high adsorption capacity of ACFs contributed to the adsorption of organic contaminants [9]. Li et al. [114] identified that the porous structure of cobalt MOFs catalyst was conducive to the adsorption and mass transfer of reactants, and exhibited good stability and recyclability under acidic conditions.

(5) Exhibiting photocatalytic activity. Some supports possess photocatalytic activity. Through the photo-generated electrons, they can facilitate the cycling of $Me^{(n+m)+}/Me^{n+}$, thereby enhancing their catalytic activity. For example, in $TiO_2$ loaded on $Fe^{II}Fe_2^{III}O_4$@C, the support was composed of $TiO_2$ and activated carbon. Under ultraviolet light irradiation, $TiO_2$ generated photo-generated electron-hole pairs, which subsequently produced active species such as $^{\bullet}OH$ and $O_2^{\bullet-}$ [113]. Besides, the $Co_3O_4$-g-$C_3N_4$ composite efficiently activated PMS through both synergistic photocatalytic and chemical catalytic effects. The p-n heterojunction formed by $Co_3O_4$ and g-$C_3N_4$ inhibited the recombination of photo-generated charges [127].

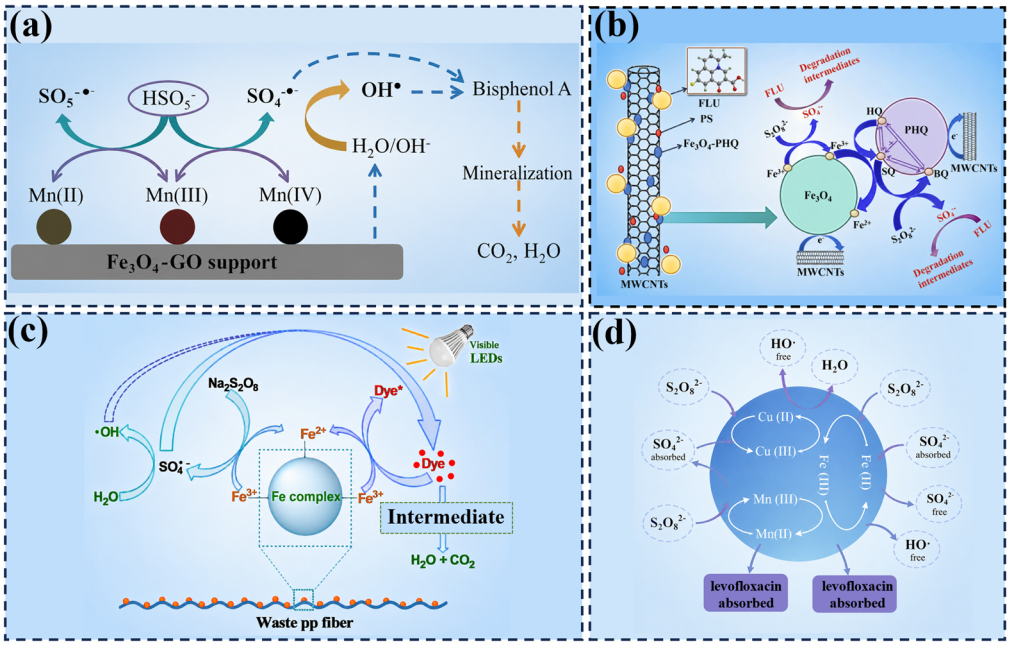


**Figure 5.** Schematic diagram of activation mechanism by representative nano-TM supported catalysts. (**a**) PMS activation by Mn-MGO hybrid particles [116]; (**b**) FLU oxidation by the system of PS and $Fe_3O_4$/MWCNTs/PHQ [122]; (**c**) Fe-PAA-g-PP catalyzed PMS activation process [123]; (**d**) PS activation by CuO/$MnFe_2O_4$ nanocomposite for levofloxacin degradation [129]. (Adapted from the corresponding reference)

### 3.4.2. Activation Mechanisms by SA-TMCs

The activation site of SA-TMCs is mainly atomically dispersed TM anchored on support (e.g., rGO, g-$C_3N_4$, metal oxide, etc.). During the PS activation by SA-TMCs, PS is often adsorbed onto the TM-N-C sites, forming reactive PS* intermediates, and then the electron transfer occur between TM-N-C sites, PS and ECs, generating ROS or occurring direct degradation of ECs. The ROS generation can be attributed to the three mechanisms mentioned earlier (Figure 6). (1) Electron transfer from TM center provides electrons, inducing homolytic cleavage of the O-O bond to generate $SO_4^{\bullet-}$ or heterolytic cleavage to form unstable high-valent metal species. Yang et al. [116] demonstrated that Co(II) centers in Co-$N_4$-C) donate electrons to PMS, inducing homolytic O-O bond cleavage to generate $SO_4^{\bullet-}$; (2) PS donates electrons to TM sites to generate $^1O_2$. Mi et al. [158] revealed that PMS donated electrons to atomically dispersed $CoN_{2+2}$ sites on nitrogen-doped carbon, triggering a selective generation of $^1O_2$ with near-quantitative yield (98.89%); (3) The surface complex forms reactive PMS* intermediates [136]. For instance, Co-$N_4$-C as the conductive bridge promoted the electron transfer from HOMO of BPA to LUMO of Co–$N_4$–C-PMS* complexes, resulting in BPA oxidation [135].

The coordination environment and support structure of SA-TMCs play a crucial role in PS activation. Liu et al. [193] constructed two distinct single-atom catalysts ($Cu_{lat}$-MgO and $Cu_{sur}$-MgO) with tailored steric configurations and precisely modulating the coordination environment of copper single atoms (lattice-embedded vs. surface-supported) on the MgO surface. They discovered that the $Cu_{lat}$-MgO/PMS system exhibited high selectivity for a non-radical pathway toward electron-enriched phenolic compounds (e.g., phenol). In contrast, the $Cu_{sur}$-MgO/PMS system operated via a hybrid radical/non-radical pathway.

Similar to supported nanoscale TM, the primary function of the support is to stabilize single atoms and modulate their coordination environment. The coordination environment influences the local electronic structure and energy levels of the TM, thereby determining the adsorption mode of PS and the extent of O-O bond cleavage, ultimately affecting ROS generation. This section focuses on summarizing the enhanced mechanisms by which the coordination environment and support synergistically optimize the electronic structure of the TM center and facilitate charge transfer.

When adjusting the local electronic structure of SA-TMCs, parameters such as electron cloud density, d-band center, and spin state are commonly used to characterize electronic modifications. The electron cloud density of a TM reflects the distribution of electrons in atomic or molecular orbitals. TM with low electron cloud density (electron-deficient TM, e.g., $Fe^{III}$, $Co^{III}$) exhibit higher oxidation states, with more d-orbital vacancies, facilitating electron acceptance from PS and favoring non-radical pathways [159]. Conversely, TM with high electron cloud density (electron-rich TM, e.g., $Fe^{II}$, $Co^{II}$) possess lower oxidation states and abundant d-electrons, enabling electron donation to PS and dominating radical pathways. For instance, PMS reacted with Fe-pyridinic N4 moieties

($Fe^{II}N_4/Fe^{III}N_4$) to form $FeN_x$-$(HO)OSO_3^-$ intermediates. Subsequent O-O bond cleavage led to distinct pathways: $Fe^{II}N_x$-$(HO)OSO_3^-$ underwent one-electron transfer to generate $SO_4^{\bullet-}$ radical, whereas $Fe^{III}N_x$-$(HO)OSO_3^-$formed a high-valent $Fe^{V}$=O complex via two-electron and O-atom transfer [42].

The d-band center directly governs the adsorption strength of reactants or intermediates on the catalyst surface, thereby determining the activity and selectivity of TM. When the d-band center shifts closer to the Fermi level, enhanced interaction occurs between the TM d-orbitals and the antibonding states of adsorbed molecules, resulting in stronger adsorption. Conversely, downward shifting of the d-band center weakens adsorption interactions. For example, in the nano-island encapsulated single cobalt atom (CoSA/Zn.OZnO) catalyst, the introduction of Co atoms into the ZnO lattice enabled the d-band center of Co atoms shift upward, enhancing the interaction with PMS and facilitating the generation of $SO_4^{\bullet-}$ [22]. Table 4 lists the regulation strategies of local electronic structure of SA-TMCs for enhancing PS activation.

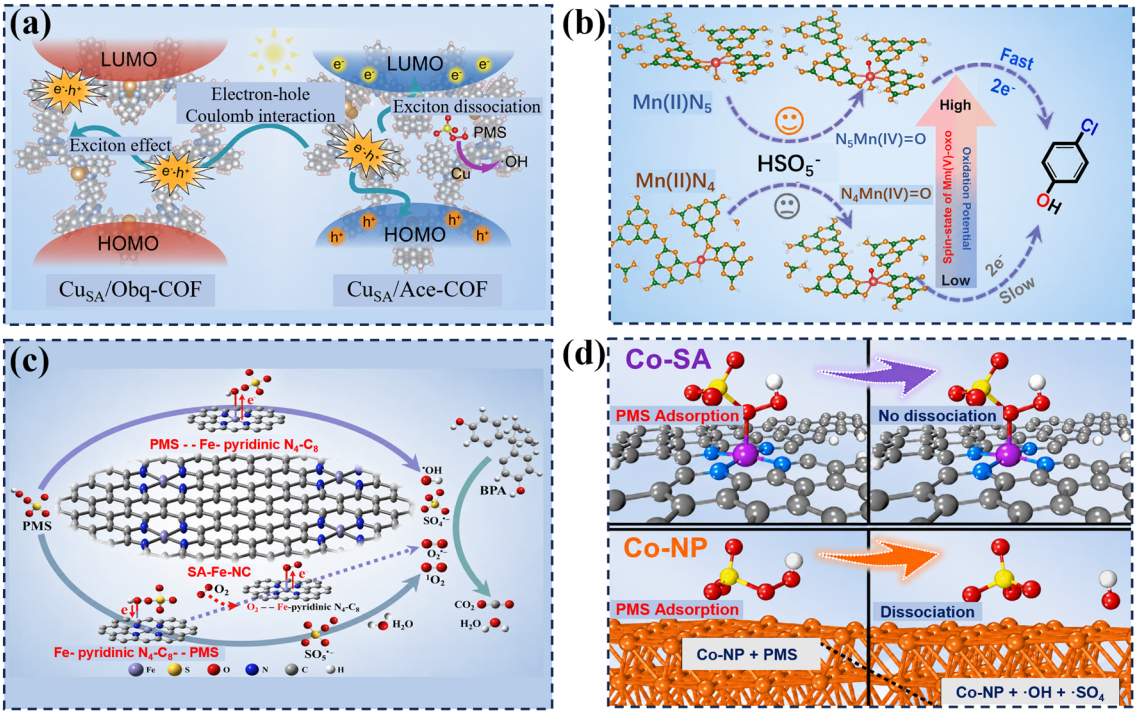


**Figure 6.** Schematic diagram of activation mechanism by representative SA-TMCs. (**a**) Photocatalytic PMS activation over CuSA/COFs [8]; (**b**) PMS activation by Mn based SA-TMCs [134]; (**c**) PMS activation by the SA-Fe-NC [160]; (**d**) PMS activations on the surface of Co-SA and Co-NP, respectively [161]. (Adapted from the corresponding reference)

The spin state of TM species critically determines both adsorption strength of reactants on the catalyst surface and the reaction thermodynamics, thereby governing reaction pathways, product selectivity, and overall catalytic efficiency. Fundamentally, high-spin states with multiple unpaired d-electrons exhibit weaker metal-substrate bonding, typically resulting in superior catalytic activity. For example, Miao et al. [134] found that in comparison to $MnN_4$ sites, the five-nitrogen coordinated $MnN_5$ sites facilitated the formation of high-spin $N_5Mn^{IV}$-oxo species with a stronger oxidation capacity. The higher spin state facilitated a lower energy barrier for electron transfer during the oxidation of organic contaminants.

The primary role of the support in SA-TMCs is to stabilize single atoms and modulate their coordination environments, with electronic effects being central to this function. N-doped carbon matrices are usually used supports, which provide intrinsic coordination sites while synergistically participating in the activation process. TM sites exhibit strong electronic coupling with carbon substrates through hybridization between their tunable 3d orbitals and carbon coordination orbitals, which greatly affect the catalytic activity of TM-carbon composites. Gao et al. [194] revealed that in PMS activation by SA-Fe-NC process, the Fe-pyridinic N4 moiety created an electron-rich Fe single atom and electron-poor carbon atoms neighboring pyridinic N, which served as active sites for PMS activation. The electron-rich Fe single atom donated electrons to PMS, facilitating PMS reduction to produce $^{\bullet}OH$ and $SO_4^{\bullet-}$. The electron-poor carbon atoms neighboring pyridinic N accepted electrons from PMS, leading to the generation of $^1O_2$.

**Table 4.** Regulation strategies of local electronic structure of SA-TMCs for enhancing PS activation.

| Catalysts | Strategy for Regulating Electronic Structure | Chang in the Electronic Structure | Effect on PS Activation | References |
|---|---|---|---|---|
| $Co_{SA}/_{Zn.O}$-ZnO | Introduction Co atoms into the ZnO lattice | D-band center of Co atoms shifts upward | Enhancing the interaction with PMS and facilitating the generation of $SO_4^{\bullet-}$ | [22] |
| $Fe_xSe_y$@C | Varying Fe/Se ratio and crystal structure | High spin state of Fe (4.16 $\mu_B$) with a large effective magnetic moment; stronger super-exchange electron interaction between Fe and Se | Regulating PMS adsorption for increasing electronic density, accelerating interfacial charge transfer for $HSO_5^-$ decomposition to produce $SO_4^{\bullet-}$ | [195] |
| $Co_3O_4$/CoS-2 | Sulfur doping strategy to construct crystalline-amorphous interfaces | Rise of d-band center; transformation of Co sites from low to high spin states; more unpaired electrons | Accelerating charge transfer and enhancing adsorption capacity for PMS; forming $Co_3O_4$/CoS-$PMS^+$ complex; dissociation of $H^+$ and combination with unpaired electrons to produce $H^{\bullet}$; fracture of peroxy bond to form high-valent $Co^{4+}$=O | [196] |
| $NiCu_{0.4}Fe_{1.6}O_4$ | Cu-doping inducing isomorphous substitution of $Fe^{3+}$ by $Cu^{2+}$, creating abundant oxygen vacancies | The d-band centers of Fe and Ni shifting closer to the Fermi level. | Enhancing PMS adsorption on OVs sites; elongated O–O bond; promoting $SO_4^{\bullet-}$ and $^{\bullet}OH$ generation with lower free energy | [197] |
| $Co_{SA}$-$Co_{NC}$/CN | Constructing Co single-atoms (saturated asymmetric $CoC_2N_2$ coordination configuration) integrated with Co nanoclusters | D-band center of Co sites shifted closer to the Fermi level; overcoming the intrinsic oxygen confinement limitation of high-spin Co; | lowering the PMS activation energy barrier ($\Delta G$ = 0.816 eV); promoting charge transfer (0.23 e) and O–O bond elongation | [198] |
| Fe-Cu-CN | Inducing a spin-state transition of Fe from low-spin to high-spin | D-band center of Fe 3d orbitals shifted closer to the Fermi level; increasing effective magnetic moment | Enabling a highly efficient electron transfer pathway for pollutant degradation; lowering free energy barrier of PMS adsorption; formation of Fe-Cu-CN-PMS* intermediate | [199] |
| TM-SA/PN-g-$C_3N_4$ | Varying transition metal (Cu, Ni, Co, Fe) in single-atom catalysts to tailor d-band center | The highest d-band center on Fe site; stronger overlap between Fe 3d and O 2p orbitals in Fe(IV)=O | Stronger PMS binding (formation of PMS*-Fe(IV)=O complex) and over-oxidation (PT ratio 44.9%); | [200] |
| Fe-$N_4$ | Engineering low-spin and high-spin $FeN_4$ sites | Coexistence of low-spin and high-spin $FeN_4$ sites; high-spin $FeN_4$ exhibiting a downshifted d-band center | Low-spin $FeN_4$ promoting $^1O_2$ generation; high-spin $FeN_4$ stabilizing $N_4Fe$-O*-$SO_4$ intermediate and lowering energy barrier for Fe(IV)=O formation | [201] |
| B-$FeN_4$CA | Doping electron-accepting B (or electron-donating P) into the second coordination shell of $FeN_4$ moiety | B-doping decreasing Fe spin state and elevates d-band center; P-doping increasing spin state and lowering d-band center | Enhancing electron transfer from PMS to Fe; stretching of H-O bond in PMS | [180] |
| Mo-doped $Co_3O_4$ | Introducing $Mo^{6+}$ into $Co_3O_4$ lattice; 3d-4d orbital hybridization between Co and Mo | Synchronous increase in spin states of both metal centers. Co d-band center shifts from 0.14 eV to –0.29 eV | Enhancing PMS adsorption and interfacial electron transfer | [202] |
| Co-NCs/C | Pyrolyzing Co-alginate hydrogel beads to form cobalt clusters anchored on carbon support | High-spin state of Co sites; increasing saturation magnetization intensity | Enhancing PMS adsorption and activation; selective generation of Co(IV)=O (nonradical pathway); lower energy barrier for Co(IV)=O formation | [144] |
| Fe-$N_5$Si-HCNs | Axial -$NH_2$ coordination and second-shell Si doping | D-band center of Fe lowering to −1.743 eV; asymmetric d-orbital electrons | Enhancing electron transfer process with autonomous regeneration of active sites | [203] |

## 4. Strategies for Improving the Activity of TM Catalysts

In most TM-activated PS-based AOPs for ROS generation, the PS activation by low-valent TM ($Me^{n+}$) typically exhibits high activity with a large reaction rate constant. However, the reduction of high-valent TM ($Me^{(n+m)+}$) by PS often becomes the rate-limiting step due to its slow kinetics. Therefore, accelerating the redox cycle between $Me^{(n+m)+}/Me^{n+}$ is critical to enhancing PS reactivity. Additionally, the structure of the TM catalysts significantly influences the adsorption and electron transfer of PS or target contaminants on their surface. To improve the catalytic performance, tailoring the electronic structure of TM catalysts is essential.

To address these challenges, various strategies have been developed to design efficient TM catalysts and optimize reaction conditions. These strategies include (1) modulating the element composition of TM; (2) engineering the TM catalyst structure; (3) introducing chemical additives; and (4) applying external energy inputs (Figure 7).

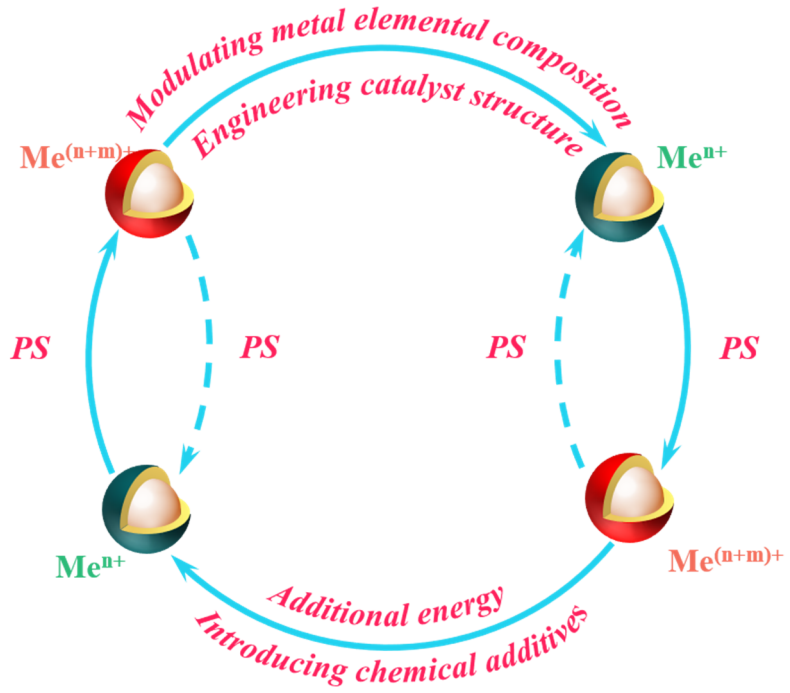


**Figure 7.** Strategies for improving the activity of TM catalysts.

### *4.1. Modulating the Element Composition of TMs*

The variation in valence electron configurations and redox potentials among different TMs leads to differences in their valence transition capabilities (e.g., $Co^{3+}/Co^{2+}$, $Fe^{3+}/Fe^{2+}$). These differences directly influence the electron transfer efficiency with PS, thereby affecting their catalytic activity. For instance, $Co^{2+}$ generally exhibits higher efficiency than $Fe^{2+}$ in activating PMS. Li et al. [204]demonstrated that high standard redox potential of $Co^{3+}/Co^{2+}$ pair (1.92 V) lied between that of $HSO_5^-$/ $SO_4^{\bullet-}$ (2.5–3.1 V) and $HSO_5^-/SO_5^{\bullet-}$ (1.1 V), enabling it to efficiently recycle for PMS activation, whereas the $Fe^{3+}/Fe^{2+}$ pair (0.8 V) exhibits a negative redox potential compared to $HSO_5^-/SO_5^{\bullet-}$, rendering its redox cycling thermodynamically unfavorable.

To enhance the conversion of $Me^{(n+m)+}$ to $Me^{n+}$ during the single electron transfer process, developing bimetallic TM catalysts may be a feasible strategy. This is because in bimetallic catalysts, the redox potential difference between metal pairs drives electron transfer, accelerating the $Me^{(n+m)+}$ to $Me^{n+}$ cycle [205]. Oh et al. [19] elaborated that this potential-gap-facilitated electron transfer represented a key mechanism enhancing catalytic efficiency in bimetallic systems. For another example, in the $MnO_2/MnFe_2O_4$ nanocomposites activated PMS system, the redox cycle between $Mn^{III}/Mn^{II}$ and $Fe^{III}/Fe^{II}$, was driven by the potential difference ($Mn^{III}/Mn^{II} \approx 0.15$ V, $Fe^{III}/Fe^{II} = 0.77$ V), facilitating electron transfer from $Mn^{III}$ to $Fe^{III}$ to regenerate the active $Fe^{II}$ species [206].

Similarly, in Fe-Co LDHs containing $Co^{II}$, $Co^{III}$, $Fe^{II}$, and $Fe^{III}$, redox coupling between $Co^{II}/Co^{III}$ and $Fe^{III}/Fe^{II}$ accelerated the $Fe^{II}/Fe^{III}$ cycle through electron exchange [207]. Moreover, introducing foreign TM into double or multiple TMs co-catalysis often promotes the redox cycles of $Me^{(n+m)+}$ to $Me^{n+}$ the metal. As mentioned in Section 3.3 above, introducing a foreign cation into perovskite, spinel and LDHs oxides can promote the TM cycles [194,208].

*4.2. Tuning the Structure of TM Catalysts*

To improve the catalytic performance, the structures of TM catalysts are primarily optimized through modifications in catalyst size, element doping, defect engineering, confinement effects, and electronic structure regulation (Figures 8 and 9).

(1) Particle size of TM catalysts

The particle size of TMs influences the number of active sites, electron transfer kinetics, and structural stability, thereby affecting catalytic activity. Generally, a decrease in particle size leads to an increased specific surface area, exposing more active sites (e.g., unsaturated coordinated metal sites), and a shorter bulk electron transfer pathway, accelerating the PS activation. However, excessively small particle sizes (e.g., <5 nm) may lead to particle agglomeration, blocking active sites and consequently reducing catalytic efficiency. Wang et al. [209] demonstrated that Co catalysts with varying active center sizes (single atoms, clusters, nanoparticles) exhibited distinct PMS activation mechanisms: single atoms predominantly drive nonradical pathways, while clusters/nanoparticles promoted radical generation via PMS dissociation. Zhang et al. [42] revealed that atomic-scale control of Fe coordination in PMS activation enabled superior bisphenol A degradation versus $Fe_3C$ nanoparticles (3–5 nm). Conversely, exceeding this size threshold triggered Fe agglomeration that obstructs active sites and electron transfer, severely compromising activity.

(2) Crystal plane defects and doping

Crystal plane defects refer to localized irregularities in atomic arrangement on crystal surfaces or within the bulk phase, encompassing point defects, line defects, and planar defects. In TM oxides, OVs represent a prevalent type of defect. The roles of OVs in modulate the electronic structure of TM centers have been discussed in the Section 3.3. Li et al. [90] demonstrated that OVs dominating $CO_3O_4$ surface defects (74%) exposed high-index facets, lowered PMS adsorption energy, and triggered O-O bond polarization via elongation, enabling efficient PMS cleavage and ofloxacin degradation. Yu et al. [210] confirmed that OVs in manganese oxides triggered charge imbalance, enhancing PMS chemisorption and polarizing the O-O bond and achieving record-high turnover frequency for bisphenol A degradation.

Doping refers to the intentional introduction of heteroatoms into the host TM lattice. The incorporated dopants modify the electronic redistribution of the host TM and induce charge compensation effects, thereby significantly influencing its catalytic activity. Duan et al. [75] found that in $Ba_{0.5}Sr_{0.5}Co_{0.8}Fe_{0.2}O_{3-\delta}$ (BSCF) perovskite, doping less-electronegative Ba/Sr at A-sites and Fe at B-sites increased electron density at Co active sites, enabling an 81-fold higher turnover frequency than undoped $Co_3O_4$ in PMS activation. Xie et al. [24] showed that S doping in iron-based nanoparticles elevated the d-band center of Fe and enhance PMS adsorption energy.

In practical catalyst design, defects and doping are frequently combined to exploit their synergistic effects, thereby optimizing catalytic performance through complementary mechanisms [211]. Yang et al. [212] revealed that dual doping of high-valence W and OVs into $Co_3O_{4-x}/WO_{2.72}$ synergistically boosted PMS activation. This enhancement originated stems from W-induced up-shifting of the Co-3d band center toward the Fermi level (facilitating electron transfer) and OVs -accelerated electron mobility in Co-3d orbitals, which collectively promoted catalytic redox cycling. Zhang et al. [22] demonstrated that the atomic cobalt doping in a nano-island catalyst ($CoSA/Zn_xO$-ZnO) optimized electron transfer for radical generation while defects ensured the microenvironmental stability.

(3) Confined TM catalysts

In PS activation systems, nano-TM /SA-TMCs catalysts face dual limitations: ultrashort radical lifespans (<10 μs) causing self-quenching and poor contaminant targeting, alongside nanoparticle agglomeration and TM leaching. Confined TM catalysts overcome these by immobilizing active sites in tailored architectures (e.g., channels, interlayers, core-shells, cages), yielding three synergistic benefits: (1) radical efficacy enhancement via proximity-driven reactions and size exclusion co-concentrating reactants; (2) lowered activation energy through spatially constrained reaction pathways; (3) stabilized TM dispersion inhibiting agglomeration/leaching while boosting activity and durability.

For instance, Zhu et al. [149] developed 3D porous SA-TMCs (e.g., honeycomb-like structures) that spatially confine TM catalytic sites within interconnected pores. This design shortened radical-contaminants mass transfer distances while enhancing electron migration via axial Cl coordination, thus achieving high PMS utilization and rapid degradation of contaminants across pH 3–11 with minimal $Co^{2+}$ leaching (3.8 ppb). Huang et al. [157] revealed that synergistic surface/space-confinement enhanced Fe-3d/O-2p orbital overlap, strengthening PMS-catalyst interfacial interactions and accelerating electron transfer. This yielded a 34.6-fold kinetic enhancement over unconfined systems.

(4) Optimizing the electronic structure of TM centers in SA-TMCs

The electronic structure of TM centers in SA-TMCs related to the TM atom type of active centers [213]. For example, Zhang et al. [42] discovered that Fe-N4 sites in Fe1/CN selectively adsorbed terminal oxygen in PMS, enabling its oxidation to $SO_5^{\bullet-}$ and subsequent 100%-selective $^1O_2$ generation. In contrast, Co/Ni single-atom sites favored PMS reduction to produce radicals.

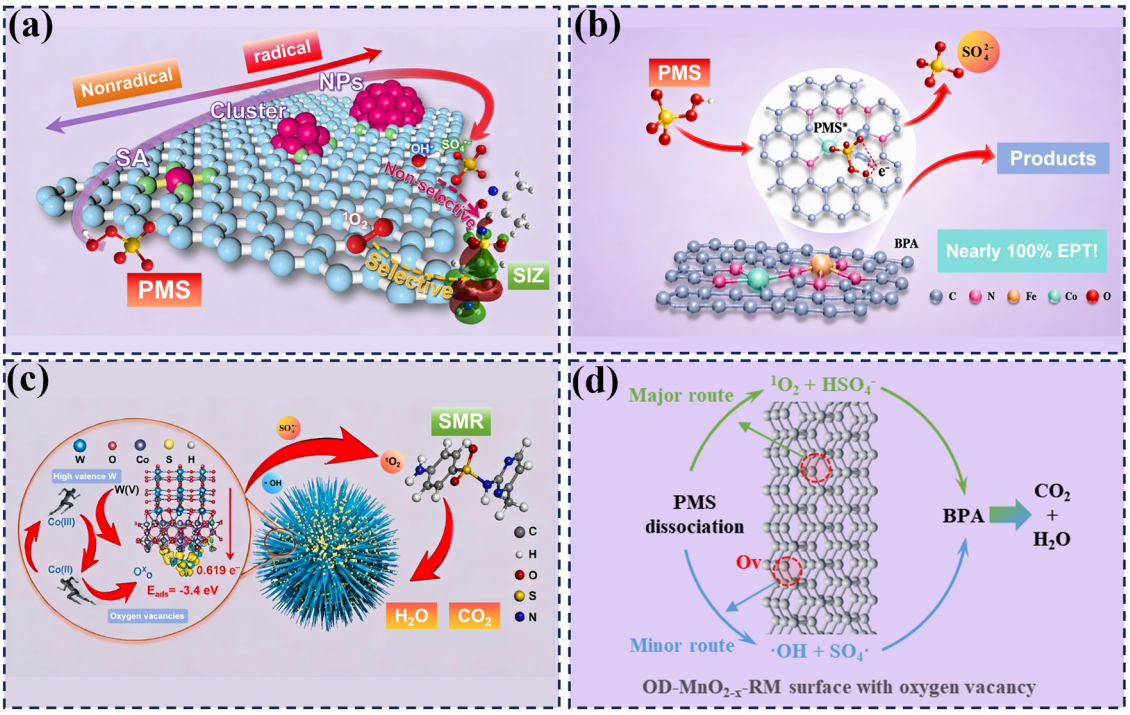


**Figure 8.** Strategies for tuning structure of representative TM catalysts in the particle size, defects and doping. (**a**) Active center size-dependent [214]; (**b**) Metal doping [137]; (**c**) Oxygen vacancy [212]; (**d**) Oxygen-deficient Mn-based SA-TMCs [210]. (Adapted from the corresponding reference).

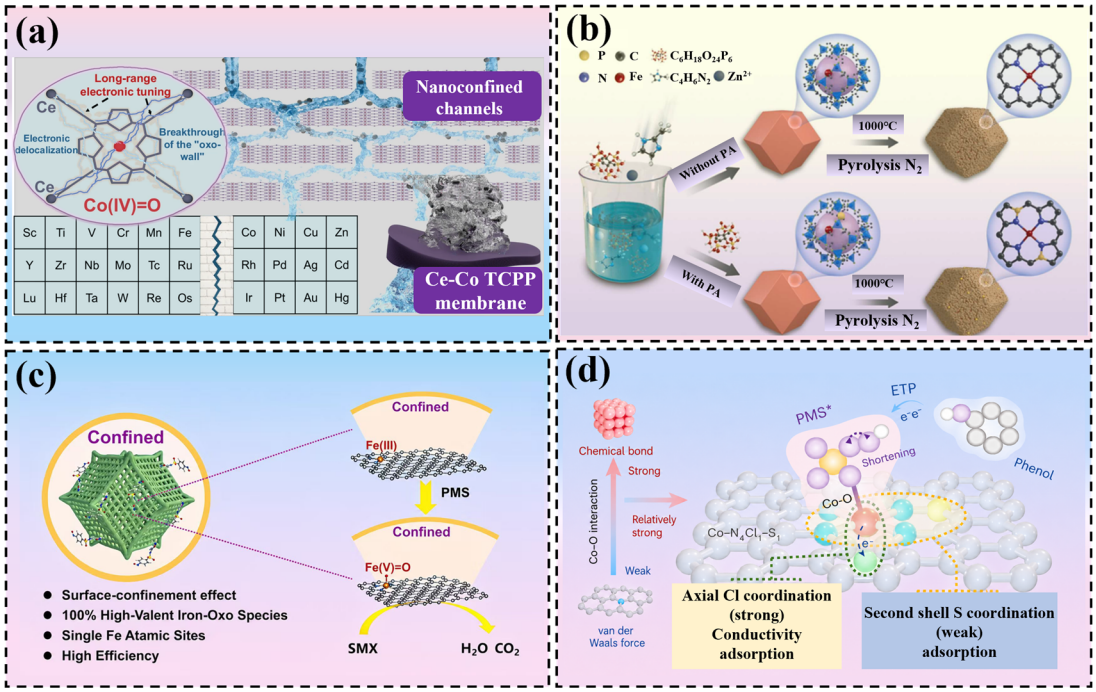


**Figure 9.** Strategies for tuning structure of representative TM catalysts in the confined domain and electronic structure. (**a**) 2D lamellar Ce-Co TCPP membrane [215]; (**b**) Tuning Fe-$N_4$ coordination environments [158]; (**c**) Surface-confinement effect on Fe single-atom catalysts [157]; (**d**) Coordination environment engineering of Co-based single-atom catalysts [149]. (Adapted from the corresponding reference).

The electronic structure of TM centers in SA-TMC can be precisely modulated by engineering their local coordination environment, including coordinated heteroatoms, coordination number, spatial configuration, and geometric configuration. (1) coordinated heteroatoms modulation [216]. For example, Chai et al. [158] demonstrated that introducing P into Fe-NC increased the electron density of Fe atoms, upshifted the d-band center, and enhanced the magnetic moment of Fe-PNC. This modification facilitated charge transfer from the Fe site to the O site in PMS, significantly improving catalytic reactivity; (2) Coordination number control. Yin et al. [217] revealed that Co-$N_3$ exhibited stronger PMS adsorption and more efficient electron transfer than Co-$N_4$, promoting O-O bond cleavage; (3) Spatial configuration engineering [149,159] identified $CoN_{2+2}$ moieties (bridging graphitic edges) as the actual active sites in $CoN_4$ configurations. The weakly positive Co centers prevented spontaneous PMS dissociation, instead facilitating electron transfer from PMS to Co for selective $^1O_2$ formation. Chen et al. [46] found that the introduction of oxygen atoms into the second coordination shell in Fe-$N_4$-$C_6O_2$ single-atom catalysts modulated the electronic state of the metal center, achieving synergistic optimization of catalytic activity and structural stability.

### *4.3. Introduction of Chemical Additives*

In the TM-activated PS systems, introducing chemical additives is a common strategy to enhance the catalytic activity of TM. The roles of these chemical additives mainly include the following aspects:

(1) Promoting TM cycling and enhancing radical generation efficiency. Some reducing additives, such as hydroxylamine, ascorbic acid, and sulfides, can accelerate the cycling of $Me^{(n+m)+}/Me^{n+}$ by $Me^{(n+m)+}$, thereby continuously activating PS and increasing the production of radicals. Li et al. [218] demonstrated that adding hydroxylamine salts to the PMS/$Fe^{2+}$ system rapidly reduced $Fe^{3+}$ to $Fe^{2+}$, significantly enhancing DMP degradation efficiency. Chen et al. [168] introduced the small organic acids (SOAs) such as formic acid, propionic acid and butyric acid in the $Co^{2+}$/PMS process. It was found that SOAs acted as electron donors to accelerate $Co^{3+}$ reduction to $Co^{2+}$ (reaction formula: $Co^{3+}$-$Ac^-$ + $e^-$ → $Co^{2+}$ + $Ac^-$), promoting the efficient cycle between $Co^{3+}$ and $Co^{2+}$ cycle in a homogenous $Co^{2+}$ /PMS system with low-level $Co^{2+}$.

(2) Regulating solution pH and inhibiting TM precipitation. PS activation often releases protons, leading to solution acidification. Certain additives (e.g., bicarbonate, phosphate) can buffer the pH, maintaining it at an optimal level. Additionally, chelating agents such as citric acid and EDTA can form soluble complexes with TM ions, preventing TM precipitation to enhance activation capability. For instance, Ling et al. [169] found that the introducing citrate in the $Fe^{2+}$/UV/PMS process at neutral pH not only stabilized $Fe^{2+}$ oxidation product ($Fe^{3+}$) by forming a soluble complex $[Fe_3O(cit)_3H_3]^{2-}$ and the formed $Fe^{3+}$-citrate complex with high molar absorbance/quantum yield promoted the UV-driven $Fe^{2+}$ regeneration.

(3) Reacting with PS or radicals to diversify ROS. Some additives (e.g., halide ions, quinones) can promote non-radical oxidation pathways. For instance, Dong et al. [219] systematically investigated the oxidation efficiency of $Mn^{2+}$/PS with different ligands and found that amino ligands such as EDTA and nitrilotriacetate could stabilize the $Mn^{3+}$ species through their electron-donating properties, thus promoting the generation of $Mn^{4+}$ species. Dong et al. [209] confirmed that the ligands in the solution could affect the electron arrangement and redox potential of iron, which also changed the reactive species generated in the $Fe^{2+}$/PDS system. The addition of chelators would induce PDS to generate $SO_4^{\bullet-}$ instead of $Fe^{IV}$ = O.

(4) Acting as co-catalysts for synergistic catalysis. Some insoluble solids additives such as $MoS_2$ can serve as supports or co-catalysts, optimizing electron transfer pathways or providing additional active sites. For example, $MoS_2$ in the $Fe^{2+}$/PMS system could enhance electron transfer through its sulfur vacancies [220]. Liu et al. [221] reported that the addition of BQ into the $Fe_3S_4$/ PMS system could effectively enhance the degradation and mineralization of bisphenol A, which was attributed to that the BQ and PMS would form active complexes (BQ-PMS*) on the surface of $Fe_3S_4$ and the excited BQ-PMS* can oxidize the BPA.

### *4.4. Introduction of External Energy*

In TM-catalyzed PS activation systems, the introduction of external energy (e.g., light, heat, ultrasound, electric fields, and mechanical energy) significantly enhances catalytic performance. This enhancement operates through mechanisms including: decreased reaction activation energy, accelerated metal redox cycling, diversified reactive species generation, and improved mass transfer.

(1) Decreasing activation energy of O-O bond cleavage in PS

The dissociation of O-O bonds in PS requires overcoming a substantial energy barrier (ca. 140–200 kJ/mol). External energy inputs (e.g., thermal, photonic, ultrasonic) directly provide the requisite activation energy to drive

homolytic cleavage of O-O bond, generating radical ROS. For example, ultrasonication cavitation achieves forcibly induce PMS homolysis through localized extreme conditions (~5000 K, 1000 atm) [18]. Cao et al. [63] documented that increasing temperature from 20 °C to 60 °C enhanced PMS dissociation efficiency by 40-fold because thermal activation overcame the inherent O-O bond dissociation barrier and directly drives homolytic cleavage of the O-O bond to generate $SO_4^{\bullet-}$ and $^{\bullet}OH$ radicals.

(2) Accelerating the cycling of $Me(n+m)^+/Me^{n+}$

As for the TM semiconductor catalysts, the photogenerated electrons in the conduction band can facilitate the intra catalyst self-redox conversion of TM ions ($Me^{(n+m)+}/Me^{n+}$) and drive self-regenerating TM ions redox cycles within the catalyst structure to maintain persistent PS activation. Hu et al. [222] observed that coupling $TiO_2$ with $Fe^{3+}$/PS under visible light decreased aqueous $Fe^{3+}$ concentration from 1.58 to 0.93 mg/L due to the photoelectron-drove the $Fe^{3+}/Fe^{2+}$ cycle. Dong et al. [223] revealed that in the g-$C_3N_4$-IMA-$FePcCl_{16}$ photocatalyst with an integrated structure, the photoelectrons from g-$C_3N_4$ under visible light reduced $Fe^{III}$ to $Fe^{II}$ in $FePcCl_{16}$, maintaining an internal $Fe^{III}/Fe^{II}$ redox cycle.

(3) Enriching the variety of ROS species

Beyond directly facilitating O-O bond homolysis to generate ROS, external energy sources significantly enrich ROS diversity. Chen et al. [224] demonstrated that in a BiOI/$TiO_2$ nanotube array photocatalytic fuel cell coupled with PMS activation, visible-light-induced photogenerated electron reduced PMS to $SO_4^{\bullet-}$, while $h^+$ facilitated $^1O_2$ generation via $SO_5^{\bullet-}$ intermediates, broadening ROS profiles ($SO_4^{\bullet-}$, $^{\bullet}OH$, $^1O_2$). Similarly, Tang et al. [225] revealed analogous charge-mediated ROS diversification in a sodium/sulfur co-doped cyano-rich polymeric carbon nitride system.

(4) Improving mass transfer and exposure of active sites

The inputs of physical energy, such as ultrasound or microwave irradiation can enhance PS activity through improving mass transfer mechanisms: (1) disrupting diffusion layer limitations at the catalyst surface to improve mass transfer and facilitate PS contact with TM active sites; and (2) increasing molecular collision frequency via thermal convection under elevated temperatures, thereby elevating the reaction rate constant. Cai et al. [226] identified that the ultrasound overcame surface diffusion barriers through acoustic cavitation, significantly enhancing PMS interaction with the Co/Fe active sites in Fe-Co/SBA-15 catalyst. Concurrently, increasing the reaction temperature from 20 °C to 60 °C boosted molecular collision frequency, raising the reaction rate constant from 0.0246 to 0.0414 $min^{-1}$. Similarly, Pang et al. [227] found that microwave irradiation overcame mass transfer limitations while leveraged thermal energy to maximize reaction kinetics, enhanced PMS activation.

## 5. Applications in the Degradation of ECs in Water and Wastewater

The pervasive detection of ECs, such as PPCPs, EDCs, PFAS, and micro-plastics, in the environments have caused significant concerns due to their persistence, bioaccumulation, and toxicological effects, which may induce adverse effects, such as endocrine disruption and carcinogenicity, threatening both ecological systems and human health [8,228]. Conventional wastewater treatment processes often fail to effectively remove ECs due to their structural complexity and low environmental concentrations [8,229,230].

### *5.1. Influencing Factors of ECs Degradation*

#### 5.1.1. Structures and Properties of ECs

ECs exhibit diverse structures, leading to significant variations in their electronic properties [231]. In PS-AOPs, the degradation efficiency of ECs primarily depends on the ROS involved and the ECs' structural and chemical characteristics [104,179]. In systems generating multiple ROS, the molecular structure of ECs critically influences both degradation efficiency and the dominant ROS pathway. For instance, Xie et al. [232] revealed that in a CoCaAl-LDO/PMS system capable of generating multiple ROS ($SO_4^{\bullet-}$, $^{\bullet}OH$ and $^1O_2$), ECs with similar structures shared common parent frameworks, resulting in consistent dominant ROS pathways for each ECs type. Certain ROS preferentially target specific functional groups or structural moieties in ECs. Zhang et al. [233] demonstrated that azo dyes were more susceptible to radical-based degradation while non-radical PMS systems were more effective for removing ECs such as bisphenols, sulfonamides, ofloxacin, and tetracyclines.

ECs properties significantly influence mass transfer and electron transfer, thereby determining their dominant reaction pathways in PS-AOPs [153,231]. As for the mass transfer efficiency, ECs enrichment near the interface promotes reactant interactions and accelerates degradation because most reactions in heterogeneous PS-AOPs occur at the solid-liquid interface [170,234,235]. As for the electron transfer propensity, key indicators for

evaluating electron-donating capacity include ionization potential (IP) and half-wave potential (φ1/2). Generally: Lower IP values (<9.0 eV) indicate greater electron loss tendency, classifying contaminants as suitable substrates for non-radical pathways [93,236]. Lower φ1/2 values reflect higher oxidation potential, favoring electron-transfer oxidation [237,238]. For instance, in the Fe7S8-2@HC800/PMS system, organics with IP > 9 (BA, NB, IBF) showed low oxidization ability, whereas those with IP < 9 (RhB, BPA, PN, p-HBA) were readily removed [239]. Pan et al. [240] demonstrated a strong correlation between φ1/2 and removal rates: φ1/2 (BPA, 4-CP, PE) < φ1/2 (SA, CBZ) < φ1/2 (MNZ, CPL), corresponding to $K_{obs}$ (BPA, 4-CP, PE) > $K_{obs}$ (SA, CBZ) > $K_{obs}$ (MNZ, CPL).

### 5.1.2. Solution pH

As previously discussed, solution pH significantly influences the ROS types and the PS stability. Under strongly acidic conditions (pH < 3), PS may homolyze to generate $SO_4^{\bullet-}$. In neutral to alkaline conditions (pH > 7), $SO_4^{\bullet-}$ can be converted to $^{\bullet}OH$. Under alkaline conditions, PS may degrade contaminants via non-radical pathways [241–244]. Besides, spontaneous decomposition of PS under alkaline conditions can lead to oxidant wastage [245]. In acidic media, $H^+$ may quench radicals (e.g., $SO_4^{\bullet-} + H^+ + e^- \rightarrow HSO_4^-$) [135,246]. Zhang et al. [233] demonstrated that $^{\bullet}OH$ and $SO_4^{\bullet-}$ were the dominant ROS in the $Co^{II}$/PMS system, with caffeine degradation exhibiting strong pH dependence due to pH-regulated radical generation. As pH increased from 4 to 9, the contribution of $^{\bullet}OH$ to caffeine degradation gradually rose, while $SO_4^{\bullet-}$ participation diminished and eventually ceased.

Solution pH determines the contaminant speciation. The solution pH modulates the molecular/ionic states of reactants, particularly the ionization of ECs (e.g., carboxylic acids, phenols), thereby altering electrostatic interactions [247]. Additionally, pH affects the thermodynamics and kinetics of electron transfer by modifying substrate electrochemical properties. Peng et al. [248] reported that as pH increased from 2.90 to 12.17, diclofenac sodium and ibuprofen transitioned from neutral molecules to anions, enhancing solubility but weakening hydrophobic interactions. This reduced adsorption at higher pH, leading to lower degradation efficiency.

Solution pH effects on activators/materials. Solution pH governs TM solubility and valence states. While low pH enhances TM dissolution, while high pH promotes hydroxide precipitation and deactivation. Chen et al. [249] achieved contaminant degradation at pH 4.0–9.0 using $Fe^{III}$-adsorbed carbon nanotubes. Besides, for heterogeneous TM activators, pH adjusts zeta potential, influencing electrostatic interactions between ECs and activator surfaces to modulate mass transfer and activation efficiency [248,250,251].

Since solution pH significantly affects the ROS type, stability and surface electronegativity of TM and contaminant properties (e.g., pKa), the design of TM catalysts capable of degrading ECs over a wide pH range is of great significance. For instance, Zhang et al. [252] designed spinel-type $ZnCo_2O_4$ porous nanosheets with engineered Co defects to mitigate pH effects on PMS activation. The amphoteric $\equiv Zn(OH)_2$ structure created a self-adaptive neutral microenvironment, enabling effective degradation across pH 4.58–9.99 via $Zn^{2+}$-mediated buffering.

### 5.1.3. Reaction Temperature

Generally speaking, an appropriate increase in temperature can substantially enhance the ECs degradation, since it promotes the cleavage of O-O bond in PS structure and expedites the ROS production. Shi et al. [253] examined the effect of temperature on PFOA decomposition during $CoMn_2O_4$/PMS process. It was revealed that the PFOA decomposition increased from 60% to 96% within 120 min when temperature increased from 30 to 50 °C. Liu et al. [254] found that the increase of reaction temperature at the range from 20 to 50 °C could easily accelerate the bisphenol S degradation by $CoFe_2O_4$/CoFe@C activated PMS system. Xu et al. [255] observed that within the p-$Co_{1.2}Mn_{1.8}O_4$/PMS system, a temperature rise similarly accelerated the degradation rate of TC significantly. Li et al. [256] underscored the favorable influence of high temperatures on reaction kinetics. Nevertheless, excessively high temperatures may impose an inhibitory effect, because they can intensify self-quenching reactions or side reactions among ROS, leading to a reduction in the concentration of effective oxidants and thereby constraining the ECs degradation. For instance, Wang et al. [257] found that the degradation efficiency of polycyclic aromatic hydrocarbon by PS-based AOPs decreased when the temperature was over 60 °C. Consequently, the optimal temperature necessitates fine-tuning based on the specific system under investigation.

### 5.1.4. Coexisting Substances

In PS-based AOPs, coexisting substances and water/wastewater matrix components exert complex effects on ECs degradation. Primary interfering substances include inorganic anions ($CO_3^{2-}$, $Cl^-$, $NO_3^-$, $SO_4^{2-}$) and natural organic matter (NOM, e.g., humic/fulvic acids) [258]. Inorganic anions typically exhibit dual roles: (1) Scavenging effects. $HCO_2^-/CO_3^{2-}$ quench $SO_4^{\bullet-}/^{\bullet}OH$ to form less reactive $CO_3^{\bullet-}$. $Cl^-$ (at high concentrations) reacts with $SO_4^{\bullet-}$ to yield less active $Cl^{\bullet}/Cl_2^{\bullet-}$ and potentially harmful halogenated byproducts. $NO_2^-$ rapidly consumes $SO_4^{\bullet-}$ to

generate $^{\bullet}NO_2$ [259]. $PO_4^{3-}$ inhibits PS activation via competitive adsorption, metal complexation, and active site blocking [260]; (2) Promotive effects under specific conditions. Yang et al. [172] found that low $Cl^-$ concentrations might initiate chain reactions producing HOCl/$Cl_2$ for indirect oxidation.

Similarly, in the $Co^{2+}$/PMS system, $Cl^-$ significantly consumes $Co^{IV}$ and enhances HOCl production via an oxygen-transfer pathway [45]. $CO_3^{\bullet-}$ selectively oxidizes electron-rich ECs (e.g., phenols) in $HCO_3^-$-containing systems [261,262]. Qin et al. [263] reported enhanced degradation of PABA, SDZ, and CAP in $Cl^-$/PMS systems due to HClO generation.

Notably, Li et al. [264] observed that in $Fe_3O_4$-mediated AOPs, $NO_3^-$ showed negligible ROS impact, $SO_4^{2-}$ suppressed ROS exposure by altering catalyst surface electronics $Cl^-$ selectively inhibited $^1O_2$ while generating $ClO^{\bullet}$ for targeted oxidation. Shi et al. [11] discovered that under low oxidant dosage conditions (e.g., less than tenfold the ECs concentration), inorganic anions commonly presented in water-such as $CO_3^{2-}$, $Cl^-$, $NO_3^-$, $SO_4^{2-}$, and $H_2PO_4^-$ exhibited significantly strong interference on heterogeneous chemical oxidation via direct electron transfer than on the ECs themselves. Furthermore, distinct interference effects were observed among different anions.

Regarding coexisting cations, the majority exhibits minimal influence or even a certain promoting effect on the ECs degradation. For instance, within the p-$Co_{1.2}Mn_{1.8}O_4$/PMS system, co-existing cations like $K^+$, $Ca^{2+}$, and $Mg^{2+}$ demonstrated almost no inhibitory effect on the tetracycline degradation, and the system exhibited robust resistance to interference [255]. In the Ni(Co)@NC/PMS system, cations such as $Ca^{2+}$ and $Mg^{2+}$ also had minimal influence on the degradation of enrofloxacin at a concentration of 1.0 mM [265]. Despite the generally minor effect of most cations, in some homogeneous PS activation systems, cations such as $Ca^{2+}$ and $Mg^{2+}$ slightly diminished the degradation efficiency of ECs due to competing for active sites or altering the ionic strength of the solution [266]. Nonetheless, on the whole, the inhibitory effect of cations on the ECs degradation is typically weaker than that exerted by certain anions (such as $HCO_3^-$ and $HPO_4^{2-}$).

NOM demonstrates antagonistic effects: On the one hand, humic acids, fulvic acids will compete to consume free radicals ($SO_4^{\bullet-}$/$^{\bullet}OH$) or combine with activators (such as $Fe^{2+}$) or block pore/active site on heterogeneous TM catalysts, thereby reducing the efficiency of ECs degradation [44]. On the other hand, NOM may enhance ECs degradation by quinoid/reducing moieties (e.g., phenolic -OH) promoting the electron transfer or accelerating $Me^{(n+m)+}$/$Me^{n+}$ redox cycling or functional group (e.g., carboxyl/ketone) producing DOM radicals [267].

For instance, NOM generated multiple photo-induced reactive intermediates (PPRIs) during photosensitization. While these PPRIs themselves exhibited a limited degradation efficiency toward ECs, they could activate PMS to produce more reactive radical species, thereby enhancing the degradation efficiency of ECs [268]. For another instance, Li et al. [264] and Wang et al. [269] demonstrated dual roles of DOM in iron/manganese oxide (IMHO)-catalyzed oxidation systems: (1) Promotive effects include accelerating $Me^{(n+m)+}$/$Me^{n+}$ redox cycling; enhancing IMHO physicochemical properties, boosting generation of DOM-derived radicals and unstable high-valent metal species, facilitating phenol/sulfonamide degradation; (2) Inhibitory effects involved pore/active site blockage via IMHO surface adsorption, radical scavenging through ECs competition, and ROS-shielding via DOM-ECs complexation.

In the most studies, the degradation of ECs through TM-activated PS-based AOPs have been carried out in pure water or simulated wastewater settings. Within these experimental frameworks, the majority of catalysts are capable of achieving approach 100% degradation efficiency for target pollutants. Nevertheless, when it comes to real aquatic environments or wastewater, the degradation performance of ECs is susceptible to the influence of various factors, including water pH, anions, and organic matter, which frequently leads to a reduction in degradation efficiency [270]. For instance, Xiang et al. [271] fabricated a FMO-FS-MS composite to activate PDS for the CBZ degradation of across diverse aqueous matrices. Their research revealed that, in comparison to ultra-pure water, the degradation efficiency of CBZ in natural water and simulated groundwater exhibited a slight decline, potentially attributable to the quenching effect stemming from the ubiquitous presence of organic and inorganic chemicals in the water. Notably, certain catalysts demonstrate high degradation efficiency in the context of actual wastewater treatment. For example, Huang et al. [100] employed the CuFeMnO/PMS system to execute continuous secondary effluent treatment on a pilot scale within a continuous flow reactor. They uncovered that the COD concentration in the effluent was below 30 mg/L with the removal efficiency of 50 to 70% during the running period. Although CuFeMnO/PMS system achieved efficient treatment performance for the secondary effluent, the final cost was estimated to be 126.8 RMB/$m^3$ of the secondary effluent, indicating that its large-scale application was unacceptable due to the unaffordable treatment costs.

The inhibition of ECs degradation in complex real water bodies or wastewater represents one of the critical bottlenecks that hinder the industrial application of TM catalysts. To boost the practical potential of TM-activated PS-based AOPs in real water matrices, employing a non-radical-dominated PS-based AOPs may constitute an effective pathway. For example, Wang and Wang [272] developed Co/SiC-2 /PMS system for the removal of SMX by surface-bound reactive and high-valent cobalt oxo. They found that Co/SiC-2 /PMS system achieved good

performance for the removal from surface water from a river, and secondary effluents from a municipal treatment plant, and secondary effluents from biopharmaceutical wastewater, respectively. Despite this fact, in a multitude of wastewater or aquatic environments, ECs are present at ng/Lor μg/L levels, whereas coexisting substances occur at mg/L levels. Although these non-radical species exhibit low reactivity towards $Cl^-$, NOM, and other substances, the significant concentration disparity between the ECs and coexisting substances can also exert an influence on the degradation process of the target ECs. Future research endeavors should persist in investigating strategies aimed at achieving efficient degradation of complex pollutants in real-world water bodies or wastewater.

Therefore, Water/wastewater matrix effects must be evaluated case-specifically, considering anion/cation type/concentration thresholds, NOM composition (e.g., quinone content), and catalyst-ECs-NOM ternary interaction.

### *5.2. Strategies for Improving the Degradation Efficiency of ECs*

In addition to enhancing the generation efficiency of ROS generation through the strategy described earlier such as engineering the TM catalyst structure and optimizing the reaction conditions, recent strategies for enhancing ECs also focus on the following aspects(Figure 10): (1) reducing the competition of background matrix with ECs for ROS by enhancing non-radical pathways with higher selectivity and longer life; (2) reducing the consumption of background matrix on the PS by galvanic cell-based reaction systems designs; (3) promoting the mass transfer to improve the utilization efficiency of ROS by TM catalyst-coupled membrane separation reactor designs; and (4) diversifying ROS types for radical and non-radical synergistic degradation.

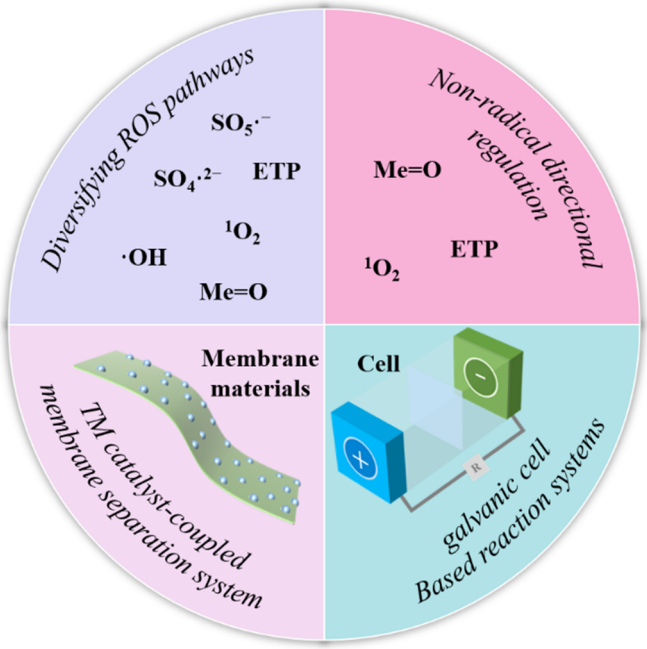


**Figure 10.** Strategies for enhancing the degradation of ECs.

#### 5.2.1. Directional Generation of Non-Radical Species

Since radicals ($^{\bullet}OH/SO_4^{\bullet -}$) are non-selective reactive oxidants, which can react with the coexisting inorganic anions and organic matter (e.g., NOM) and reduce the degradation efficiency of ECs, especially in wastewater with complex water quality components. In contrast to radicals, non-radical ROS, such as $^1O_2$, unstable high-valent metal and TM-PS* complex, has excellent resistance ability to water matrix interference (e.g., humic acid, salts). Therefore, the degradation of ECs by non-radical ROS is a promising strategy for improving the degradation efficiency of ECs.

For example, the PMS activation by Fe/O co-doped g-$C_3N_4$ nano-sheet catalyst could produce the $^1O_2$ and $Fe^V = O$. They can rapidly degrade bisphenol A in a simulated high salt wastewater (≥200 mM) with a reaction rate constant of 1204-fold higher than that in g-$C_3N_4$+PMS system [273]. Yao et al. [274] found that in the $Zn_xCo_t$-ZIFs activated PMS system, the produced $^1O_2$ could selectively oxidize electron-rich ECs. This $^1O_2$-dominant pathway made the system maintained nearly unchanged phenol degradation efficiency in the presence of 50 mM anions/cations (e.g., $Cl^-$, $HCO_3^-$, $Ca^{2+}$), whereas radical-dependent systems (e.g., $Zn_2Co_1$-C/PMS) showed significant inhibition.

Chen et al. [275] found that during non-radical-mediated PMS oxidation degradation, ECs underwent a polarity shift. This shift prevented their complete mineralization and instead, due to the "hydrophobic effect" leads to their enrichment on the catalyst surface. This phenomenon is termed the "Organic Carbon Transfer Process (OCTP)". Based on the mechanism of OCTP, the research team proposed two strategies for optimizing wastewater treatment technology: (i) enhancing OCTP to indirectly remove weakly polar micro-pollutants or ECs from water; and (ii) tuning the catalyst surface polarity to reduce the occurrence of OCTP, thereby improving the long-term stability of the catalyst.

#### 5.2.2. Development of Galvanic Cell-Based Reaction Systems

To overcome limitations of traditional AOPs where co-existing substrates compete for ROS, developing galvanic cell-based reaction systems to separate contaminant activation (anode) and oxidant activation (cathode) is a feasible strategy. This is because, on the one hand, activating PS for degrading ECs is essentially a redox reaction, which can be enhanced through rational design of the anode and cathode in a primary battery system. On the other hand, the spatially separated activation of substrates and oxidants prevents interference from co-existing matrix components (e.g., $Cl^-$, $HCO_3^-$). For example, Shi et al. [161] proposed a galvanic cell reactor with CuO as anode and CNTs as cathode, where phenol and PS were activated at the CuO and at CNTs, respectively. Electrons from phenol oxidation at CuO anode migrated to the cathode via the external circuit, reducing PDS to $SO_4^{2-}$. Because phenol and PDS were confined to separate chambers in a galvanic cell reactor, which reduced interfacial resistance and enlarged the potential difference between the two electrodes to maximize electron transfer efficiency. The [$CNT^+$|-$CuO^-$] configuration achieved a 4.6-fold higher reaction rate constant compared to single-catalyst systems. Zhu et al. [276] constructed a galvanic cell system utilizing FeCo@CF as the anode, while graphite rods served as the cathode electrode. The FeCo@CF catalyzed PMS decomposition, generating ROS, and the electrode exhibited excellent reactivity with PMS and the rapidly generated ROS efficiently degrade ECs. Shi et al. [161] utilized CuO and CNTs as model catalysts in a dual-chamber microbial fuel cell. By segregating the oxidant and contaminant in separate chambers, the system achieved direct electron transfer-driven ECs degradation with ultralow oxidant consumption (1.6 × contaminant concentration), eliminating chemical reagent residuals in treated water and demonstrating scalability for practical water purification.

#### 5.2.3. Coupled to Membrane Separation System

Loading the TM catalyst on a membrane material is currently a promising strategy for enhancing mass transfer and reaction efficiency. The membrane acted as both a support (improving mass transfer efficiency) and a barrier (intercepting contaminants). The coupled system has following advantages: (1) The membrane pores confine the ECs and PMS or ROS on the membrane surface, increasing local concentrations and restricting diffusion of ROS into the bulk solution, enhancing mass transfer and reducing diffusion limitations; (2) The mass transfer distances between ROS generation sites, PS and ECs are precisely shortened by the nanoconfinement effect in pores, ensuring sufficient contact for catalytic reactions; (3) PS activation on the membrane surface achieved simultaneous ECs degradation and fouling mitigation through ROS attack and interfacial repulsion.

Zhang et al. [270] developed monolithic ceramic $CoTiO_3/TiO_2$ membranes for PMS activation. It was found that the membrane pores spatially confined ECs near the ROS generation sites (i.e., the catalyst surface), thereby accelerating the reaction and enhancing the overall ROS utilization efficiency. Moreover, the $CoTiO_3/TiO_2$ membranes prevent $Co^{2+}$ leaching, ensuring both high catalytic efficiency and structural integrity under reaction conditions. Yin et al. [151] developed a novel Fe-SAC/PTFE catalytic membrane that activates PMS to efficiently degrade ECs by nano-confinement effects. This membrane acted as both catalyst support and physical barrier, enhancing reaction kinetics. The pore confinement boosted radical usage by 14% and reduced charge transfer resistance compared to non-porous systems, overcoming diffusion limitations. Liu et al. [277] engineered a catalytic membrane by immobilizing nitrogen-doped MWCNTs on an alumina ceramic substrate. This pressurized system concentrated ECs and PMS near catalytic sites, drastically shortening mass transfer distances. It achieved complete, continuous-flow phenol removal-significantly outperforming static setups (40% removal) and powdered catalysts requiring 40 min. The robust ceramic substrate prevented metal leaching during extended operation. This system could effectively remove 77–99% of fluorescent organics from challenging real waters like Songhua River.

#### 5.2.4. Diversifying ROS Types

In PS-based AOPs systems, the generated ROS primary include radicals (e.g., $^{\bullet}OH$, $SO_4^{\bullet-}$, $O_2^{\bullet-}$) and non-radical species (e.g., $^1O_2$, unstable high-valent TM species, and TM-PS* complexes). Radical species exhibit high oxidation potentials but low selectivity, degrading ECs via non-specific attack. Non-radical species demonstrate

longer lifetimes and higher selectivity, oxidizing ECs through direct electron transfer or specific interactions. Notably, non-radical pathways may promote polymerization and preferentially oxidize electron-rich organics, often generating intermediates when treating electron-deficient compounds [16]. Therefore, optimizing ROS distribution can achieve multiple functions in degrading contaminants [278].

Firstly, the synergistic interplay between radical and non-radical pathways can enhance system efficiency that caused by that different ROS target distinct sites on ECs [211]. For example, Xiao et al. [279] showed that cobalt-based catalysts activated PMS system, radical-dominated reactions broadly broke down complex ECs structures, non-radical pathways driven by $^1O_2$ selectively oxidized electron-rich sites via electrophilic attack, collectively minimizing byproduct accumulation and enhancing mineralization.

In addition, in the Pd-$Fe_3O_4$ activated PMS system, oxidative radicals ($^{\bullet}OH/SO_4^{\bullet-}$) cleave C-Cl bonds in chlorinated hydrocarbons (CHCs) by attacking electron-rich sites, whereas nucleophilic $H^{\bullet}$ selectively dechlorinates recalcitrant CHCs (e.g., carbon tetrachloride, chloroform). This synergistic radical/non-radical strategy achieves ultra-fast CHC degradation and mineralization, overcoming limitations of single-species systems [280]. A more detailed discussion on active species in PS-based AOPs can be found in the comprehensive reviews [15,281]. Liu et al. [282] revealed that in Fe/$Fe_3O_4$-anchored 3D rGO composite/PMS system, surface-generated radicals ($^{\bullet}OH/SO_4^{\bullet-}$) decomposed hydrophilic segments of phenolic compounds through non-selective oxidation, while non-radical pathways (dominated by $^1O_2$) mineralized pre-adsorbed hydrophobic moieties via electrophilic attack, enabling comprehensive ECs mineralization.

Secondly, synergistic radical/non-radical strategy can increase oxidant utilization efficiency because radical pathways may be quenched by common water constituents (e.g., $HCO_3^-$, NOM), whereas non-radical pathways remain less affected by water matrix interference. For example, Pei et al. [283] demonstrated that in the iodine single-atom catalyst (I-NC) activated PMS system, the surface-confined $^1O_2$ exhibited exceptional resistance to common water matrix interferents (e.g., $HCO_3^-$, $Cl^-$, $SO_4^{2-}$, humic acid) through electrophilic interfacial reactions. The system maintained >90% ciprofloxacin degradation efficiency across diverse water matrices (tap water, groundwater, hospital wastewater). This radical/non-radical synergy suppressed oxidant wastage (<5%) and intermediate accumulation in complex wastewaters.

Finally, synergistic radical/non-radical strategy can extend pH adaptability. Radicals (e.g., $^{\bullet}OH$) dominate under acidic conditions, while non-radicals (e.g., $^1O_2$) are more active in neutral/alkaline environments. This synergy broadens the effective pH range for contaminant degradation. For example, Luo et al. [284] revealed that acidic conditions (pH 3–5) promoted radical pathways through proton-assisted PMS dissociation, while neutral-to-alkaline conditions (pH 7–11) favored non-radical pathways via deprotonation-triggered PMS activation on carbon defects or heteroatom-doped sites of I-doped carbon or N/S-co-doped rGO catalysts. This pH-regulated mechanism switch mitigated efficiency loss at extreme pH values. Consequently, this dual-mechanism systems achieved >90% contaminant removal across pH 3–11, broadening effective pH windows >300% versus radical-only systems.

Above multi-pathway cooperation could enhance degradation kinetics, minimize undesired side reactions, and improve the practical applicability of PS-based AOPs in complex water matrices.

## 6. Conclusions and Perspectives

### *6.1. Conclusions*

TMs have demonstrated significant advantages in activating PS due to their unique electron structures, making them the predominant catalysts in recent years. Among them, Co, Fe, W, Cu, and Mn-based catalysts have attracted widespread attention in PS activation.

TM catalysts can be classified into homogeneous and heterogeneous types. Homogeneous TM catalysts primarily consist of soluble TM compounds, whereas heterogeneous TM catalysts exhibit diverse structures, including non-supported TM oxides, supported nano TM catalysts, and SA-TMCs, etc., which are currently the focus of extensive research. The structures of heterogeneous TM catalysts are highly dependent on their synthesis methods. Non-supported TM catalysts are typically prepared via ball milling, precipitation/co-precipitation, or hydrothermal/solvothermal methods. In contrast, supported TM nanoparticles are synthesized through methods such as the impregnation method, sol-gel method, hydrothermal/solvothermal method, co-precipitation method, ion exchange method, electro-deposition, mechanical mixing/ball milling, and photoreduction/microwave-assisted synthesis. SA-TMCs are mainly fabricated via high-temperature pyrolysis, solution coordination, post-modification strategies, and *in-situ* templating approaches.

During PS activation by TM catalysts, the TM sites in the catalyst can form bonded reactive complexes with PS. Subsequently, electron transfer may occur among the catalyst, PS, and organic contaminants. The direction of

electron transfer influenced by the valence electron structure of the TM and the molecular structure of the ECs. Following electron transfer, the chemical bonds of PS are stretched and cleaved, generating ROS. The ROS generation generally involves three mechanisms: single electron transfer, oxygen transfer and complex mechanisms. The produced ROS may include radical species ($SO_4^{\bullet-}$, $^{\bullet}OH$) and non-radical species (unstable high-valent TM, $^1O_2$, etc.).

The different structures and active sites of TM catalysts lead to different ways of interaction with PS, and also result in different types and mechanisms of ROS generation. Additionally, the structure and properties of ECs can also modulate the TM catalysts activity and the ROS generation pathway. Some ECs may directly participate in electron transfer with activated PS molecules. In some supported TM catalysts, the support sites facilitate PS adsorption, while the TM sites regulate electron distribution and accelerate electron transfer.

The PS activation performance of TM catalysts is closely related to their structures. Optimizing the elemental composition, exposed crystal facets, particle size, defect structures, coordination environment of TM, and employing confinement strategies can adjust the composition and structure (e.g., active site distribution, TM valence states, and surface electronic configuration) of TM catalysts, thereby enhancing catalytic activity and steering the reaction toward favorable advanced oxidation pathways. Furthermore, external chemical additives (e.g., ligands, and redox auxiliaries) and energy inputs (e.g., light, ultrasound, electricity, and mechanical energy) can also improve catalytic performance.

In TM-catalyzed PS systems for degrading ECs in water and wastewater, the degradation efficiency depends not only on ROS generation but also on the structure and properties of the ECs, solution pH, and coexisting substances. To enhance the degradation efficiency in complex aqueous environments, strategies such as optimizing ROS composition, coupling membrane separation system, and constructing galvanic cell reaction systems can be employed.

### *6.2. Perspectives*

To better understand and develop TM-based PS activation systems, the following key aspects should be addressed in future research:

(1) Ligand effects in homogeneous TM catalysis. The homogeneous TM-catalyzed PS activation often form ligand-TM-PS complexes, where the ligand structure directly influences the TM's electronic configuration and PS activation pathway. A deeper understanding of how ligand structural parameters govern TM electronic properties and PS activation mechanisms is essential. Future studies should furtherly elucidate the correlation between ligand design, TM redox behavior, and radical/non-radical pathway selectivity.

(2) Synthetic control of TM catalyst structures. The synthesis methods determine the structure of TM catalysts, but the regulatory laws between the synthesis methods and TM catalyst structures still need to be further clarified. The chemical principles of the TM catalysts synthesis process still need to be further revealed, and the influence mechanism of the synthesis methods on TM catalyst structures still need to be further analyzed. Moreover, current synthesis routes are often complex and costly, hindering large-scale application. To provide a theoretical basis for the synthesis of TM catalysts with specific structures for practical engineering applications, future work should focus on (i) uncovering universal synthesis-structure correlations, and (ii) elucidating the chemical mechanisms of catalyst formation.

(3) Structure-activity relationships in TM catalysts. While the PS activation mechanisms of individual TM catalysts have been extensively studied, generalized rules linking TM catalyst structure (size, morphology, TM composition, and TM-support interactions) to performance remain elusive. Advanced data-driven approaches (e.g., machine learning and high-throughput experimentation) should be employed to decode these relationships, which is beneficial to the rational design of TM catalysts with optimized activity and pathway selectivity.

(4) Distribution and roles of chemical energy in PS activation. PS activation requires energy input to cleave O-O or O-$SO_3$ bonds, and the energy released when TM interact with PS may influence bond-breaking patterns and catalytic efficiency. For example, the energy released when TM interact with PS may be used to activate reactant molecules or solid catalysts. Therefore, understanding the exchange and distribution of energy during the interaction between TM catalysts and PS are of great significance for revealing their catalytic mechanisms. Meanwhile, the lifetime, deactivation, and reactivity of surface-bound reactive species also require further investigation. Future research suggests further revealing the energy exchange process between PS and the TM catalyst, as well as the influence law of energy changes on the activation mechanism, and further studying the influence law of the existence state of surface-active species on its activation mechanism. Future studies should further reveal (i) energy redistribution and its roles in PS activation during TM-PS interactions and (ii) the stability and reactivity of interfacial active species to refine mechanistic models.

(5) Sustainable promotion strategies. External chemical additives and energy can enhance PS activation but may introduce secondary pollution or high energy costs. Future studies should prioritize eco-friendly, low-cost chemical promoters and harness renewable energy (e.g., solar or hydrodynamic power) to drive TM-catalyzed processes, which may be more beneficial for practical wastewater treatment.

(6) Catalyst stability and regeneration. PS activation induces surface reconstruction and physicochemical changes in TM catalysts due to oxidative etching, proton release, and sulfate accumulation, leading to a gradual decrease in activity and a low recycling efficiency of active sites. Despite considerable advances in current research, the underlying causes and mechanistic pathways of these issues remain incompletely understood. A critical breakthrough is required in fundamental theoretical understanding of surface reconstruction mechanisms, along with the development of innovative strategies for efficient catalyst regeneration.

(7) During PS activation, the release of protons and sulfate ions may occur, while coexisting substances in aqueous systems can interfere with target ECs degradation. The recently developed bipolar chamber galvanic cell reactor offers a promising solution to this challenge by spatially segregating PS activation and ECs degradation into distinct compartments. Future studies should focus on (i) optimizing reactor configurations and electrode designs; and (ii) elucidating the underlying reaction mechanisms to further enhance process efficiency.

(8) Demand-driven catalyst design. During the PS activation process, water matrix composition and ECs structure dictate the required ROS profiles. These ROS profiles can be precisely modulated through TM catalyst design and activation conditions, where the TM catalyst's structure is inherently linked to its synthesis methodology. How to systematically construct this demand-oriented design and synthesis method of TM catalysts is the key to the successful application of TM catalysts in practical engineering. A systematic framework linking (i) pollutant characteristics → (ii) ROS demand → (iii) TM catalyst structure → (iv) synthesis methods must be established to enable precision TM catalyst engineering for practical wastewater treatment scenarios.

(9) Machine learning is playing a pivotal role in the design of TM catalysts. The integration of machine learning with density functional theory has achieved successful outcomes in catalyst design across various catalytic fields, including as hydrogen electrocatalysis and the catalytic reduction of carbon dioxide. Although direct application research in the field of PS activation is still in its nascent stages [285], achievements in other fields have offered valuable methodological insights for the design of PS activation catalysts. In the future, in-depth research endeavors can focus on constructing a specialized machine learning database for TM-PS systems, encompassing the electronic structures, redox potentials, and coordination environment characteristics of prevalent catalytic metals such as Co, Fe, Cu, and Mn; Additionally, there is a need to develop key descriptors tailored to PS activation reactions, including metal-ligand bond energies, d-band center positions, and metal redox potential difference. Furthermore, utilizing machine learning to predict diverse single metal sites and their spatial configurations, as well as the synergistic interactions among mixed single-atom sites, represents another promising avenue for exploration.

(10) *In-situ* characterization techniques are important roles in elucidating the activation mechanism of PS. The current developed characterization techniques encompass *in-situ* Raman spectroscopy, spherical aberration-corrected electron microscopy, X-ray absorption spectroscopy, and synchrotron radiation spectroscopy. Looking ahead, development of time-resolved *in-situ* characterization techniques will enable real-time capture of short-lived intermediates during the PS activation process. The integration of *in-situ* infrared spectroscopy with mass spectrometry, will facilitate the generation pathway of free radicals and radical pathways and the transformation mechanisms of ROS. Moreover, it is necessary to develop *in-situ* characterization methods for investigating the regulatory effects of environmental conditions (such as pH, temperature, and coexisting ions) on the PS activation mechanism and on the catalytic behavior of TM in real-world wastewater environments.

(11) Integrating machine learning with *in-situ* characterization technology represents a significant trend for future advancements. Future endeavors can leverage machine learning algorithms to process vast amounts of *in-situ* spectral data, enabling rapid identification of key characteristic peaks and active species. Furthermore, machine learning can also be employed to predict dynamic processes that are difficult capture in *in-situ* characterization. The profound amalgamation integration of machine learning and *in-situ* characterization, holds promise for expediting the discovery and practical application of TM catalysts with high-performance for PS activation.

## Funding

The research was funded by the National Science Foundation of China (42577058 and 52230005).

**Institutional Review Board Statement**

Not applicable.

**Informed Consent Statement**

Not applicable.

**Data Availability Statement**

The novel data were not generated or data remains inaccessible due to privacy.

**Conflicts of Interest**

The authors declare no conflict of interest.

**Use of AI and AI-Assisted Technologies**

During the preparation of this work the authors used ChatGPT, DeepSeek and WPS AI in order to polish language and modify the image. After using this tool/service, the authors reviewed and edited the content as needed and takes full responsibility for the content of the published article.

**References**

1. Liu, Y.; Yang, Z.; Wang, J.L. Fenton/Fenton-Like Processes with *In-Situ* Production of Hydrogen Peroxide/Hydroxyl Radical for Degradation of Emerging Contaminants: Advances and Prospects. *J. Hazard. Mater.* **2021**, *404*, 124191.
2. Liu, Y.; Wang, J.L. Multivalent Metal Catalysts in Fenton/Fenton-Like Oxidation System: A Critical Review. *Chem. Eng. J.* **2023**, *466*, 143147.
3. Wang, J.L.; Chen, H. Catalytic Ozonation for Water and Wastewater Treatment: Recent Advances and Perspective. *Sci. Total Environ.* **2020**, *704*, 135249.
4. Wang, J.L.; Zhuan, R. Degradation of Antibiotics by Advanced Oxidation Processes: An Overview. *Sci. Total Environ.* **2020**, *701*, 135023.
5. Huang, X.X.; Wen, D.H.; Wang, J.L. Radiation-Induced Degradation of Sulfonamide and Quinolone Antibiotics: A Brief Review. *Radiat. Phys. Chem.* **2024**, *215*, 111373.
6. Liu, X.Y.; Wang, J.L. Decolorization and Degradation of Various Dyes and Dye-Containing Wastewater Treatment by Electron Beam Radiation Technology: An Overview. *Chemosphere* **2024**, *351*, 141255.
7. Zhang, X.; Wei, J.; Wang, C.; et al. Recent Advance of Fe-Based Bimetallic Persulfate Activation Catalysts for Antibiotics Removal: Performance, Mechanism, Contribution of the Key ROSs and Degradation Pathways. *Chem. Eng. J.* **2024**, *487*, 150514.
8. Zhu, C.; Yang, M.; Jiang, B.; et al. Insights into Excitonic Behavior in Single-Atom Covalent Organic Frameworks for Efficient Photo-Fenton-Like Pollutant Degradation. *Nat. Commun.* **2025**, *16*, 790.
9. Gong, F.; Wang, L.; Li, D.; et al. An Effective Heterogeneous Iron-Based Catalyst to Activate Peroxymonosulfate for Organic Contaminants Removal. *Chem. Eng. J.* **2015**, *267*, 102–110.
10. Yu, C.; Zhao, Z.; Zong, Y.; et al. Electric Field-Enhanced Coupled with Metal-Free Peroxymonosulfate Activator: The Selective Oxidation of Nonradical Species-Dominated System. *Water Res.* **2022**, *227*, 119323.
11. Shi, L.; Wang, Z.; Zhang, Y.; et al. Anions-Impacted Water Purification from a Dual-Substrate Perspective. *Environ. Sci. Technol.* **2025**, *59*, 12378–12386.
12. Yin, Y.N.; Wang, J.L. The Evolution of Environmental Technology: From End-of-Pipe to Systemic Solutions. *Environ. Microb. Technol.* **2026**, *1*, 1.
13. Wacławek, S.; Lutze, H.V.; Grübel, K.; et al. Chemistry of Persulfates in Water and Wastewater Treatment: A Review. *Chem. Eng. J.* **2017**, *330*, 44–62.
14. Duan, X.; Su, C.; Zhou, L.; et al. Surface Controlled Generation of Reactive Radicals from Persulfate by Carbocatalysis on Nanodiamonds. *Appl. Catal. B Environ.* **2016**, *194*, 7–15.
15. Wang, J.L.; Wang, S.Z. Activation of Persulfate (PS) and Peroxymonosulfate (PMS) and Application for the Degradation of Emerging Contaminants. *Chem. Eng. J.* **2018**, *334*, 1502–1517.
16. Li, F.; Lu, Z.; Li, T.; et al. Origin of the Excellent Activity and Selectivity of a Single-Atom Copper Catalyst with Unsaturated Cu-$N_2$ Sites via Peroxydisulfate Activation: Cu(III) as a Dominant Oxidizing Species. *Environ. Sci. Technol.* **2022**, *56*, 8765–8775.

17. Wang, S.; Zhang, X.; Wang, L.; et al. Single-Atom Catalysts for Photo-Related Advanced Oxidation Processes towards Environmental Remediation. *Adv. Funct. Mater.* **2026**, *36*, 202526761.
18. Afshin, T.; Kakavandi, B.; Azizi, M.; et al. Efficient Activation of Peroxymonosulfate by Using Ferroferric Oxide Supported on Carbon/UV/US System: A New Approach into Catalytic Degradation of Bisphenol A. *Chem. Eng. J.* **2018**, *331*, 729–743.
19. Oh, W.; Dong, Z.; Lim, T. Generation of Sulfate Radical through Heterogeneous Catalysis for Organic Contaminants Removal: Current Development, Challenges and Prospects. *Appl. Catal. B Environ.* **2016**, *194*, 169–201.
20. Peng, Y.; Tang, H.; Yao, B.; et al. Activation of Peroxymonosulfate (PMS) by Spinel Ferrite and Their Composites in Degradation of Organic Pollutants: A Review. *Chem. Eng. J.* **2021**, *414*, 128800.
21. Liu, Z.; Ren, X.; Duan, X.; et al. Remediation of Environmentally Persistent Organic Pollutants (POPs) by Persulfates Oxidation System (PS): A Review. *Sci. Total Environ.* **2023**, *863*, 160818.
22. Zhang, Z.; Duan, P.; Zheng, J.; et al. Nano-Island-Encapsulated Cobalt Single-Atom Catalysts for Breaking Activity-Stability Trade-Off in Fenton-Like Reactions. *Nat. Commun.* **2025**, *16*, 115.
23. Su, R.; Gao, Y.; Chen, L.; et al. Utilizing the Oxygen-Atom Trapping Effect of $Co_3O_4$ with Oxygen Vacancies to Promote Chlorite Activation for Water Decontamination. *Proc. Natl. Acad. Sci. USA* **2024**, *121*, e2319427121.
24. Xie, J.; Wu, S.; Luo, C.; et al. Modulating Electronic Structure of Active Sites on Iron-Based Nanoparticles Enhances Peroxymonosulfate Activation. *Appl. Catal. B Environ.* **2024**, *354*, 124138.
25. Jia, H.; Yao, N.; Liao, Z.; et al. Understanding the Role of Spin State in Cobalt Oxyhydroxides for Water Oxidation. *Angew. Chem. Int. Ed.* **2024**, *63*, e202408005.
26. Xu, W.; Huang, D.; Wang, G.; et al. Doped $Cu^0$ and Sulfidation Induced Transition from R-O$^\bullet$ to $^\bullet$OH in Peracetic Acid Activation by Sulfidated Nano Zero-Valent Iron-Copper. *Water Res.* **2024**, *256*, 121621.
27. Zhu, J.; Wang, S.; Li, H.; et al. Degradation of Phosphonates in Co(II)/Peroxymonosulfate Process: Performance and Mechanism. *Water Res.* **2021**, *202*, 117397.
28. Zhao, Y.; Chen, S.; Qie, H.; et al. Selective Activation of Peroxymonosulfate Govern by B-Site Metal in Delafossite for Efficient Pollutants Degradation: Pivotal Role of *d* Orbital Electronic Configuration. *Water Res.* **2023**, *236*, 119957.
29. Zhang, Y.; Yang, J.; Ge, R.; et al. The Effect of Coordination Environment on the Activity and Selectivity of Single-Atom Catalysts. *Coord. Chem. Rev.* **2022**, *461*, 214493.
30. Cao, P.; Mu, X.; Chen, F.; et al. Breaking Symmetry for Better Catalysis: Insights into Single-Atom Catalyst Design. *Chem. Soc. Rev.* **2025**, *54*, 3848–3905.
31. Zhu, S.; Zhong, S.; Cheng, C.; et al. Microenvironment Engineering of Heterogeneous Catalysts for Liquid-Phase Environmental Catalysis. *Chem. Rev.* **2024**, *124*, 11348–11434.
32. Chang, B.; Zhang, L.; Wu, S.; et al. Engineering Single-Atom Catalysts toward Biomedical Applications. *Chem. Soc. Rev.* **2022**, *51*, 3688–3734.
33. Du, Y.; Ma, W.; Liu, P.; et al. Magnetic $CoFe_2O_4$ Nanoparticles Supported on Titanate Nanotubes ($CoFe_2O_4$/TNTs) as a Novel Heterogeneous Catalyst for Peroxymonosulfate Activation and Degradation of Organic Pollutants. *J. Hazard. Mater.* **2016**, *308*, 58–66.
34. Jiang, J.; Zhao, Z.; Gao, J.; et al. Nitrogen Vacancy-Modulated Peroxymonosulfate Nonradical Activation for Organic Contaminant Removal via High-Valent Cobalt-Oxo Species. *Environ. Sci. Technol.* **2022**, *56*, 5611–5619.
35. Gao, S.; Cui, J.; Xiong, Y.; et al. Synergetic Effect of the Mineralization of Organic Contaminants by a Combined Use of Permanganate and Peroxymonosulfate. *Sep. Purif. Technol.* **2015**, *144*, 248–255.
36. Wang, Z.; Yu, Y.; Guo, Q.; et al. Nano- and Micro-Scale Zerovalent Iron-Activated Peroxydisulfate for Methyl Phenyl Sulfoxide Probe Transformation in Aerobic Water: Quantifying the Relative Roles of $SO_4^{\bullet-}$, Fe(IV), and $^\bullet$OH. *Water Res.* **2022**, *223*, 119014.
37. Xu, Z.; Xiao, F.; Purnell, S.; et al. Size-Dependent Catalytic Activity of Supported Metal Clusters. *Nature* **1994**, *372*, 346–348.
38. Ahn, Y.; Bae, H.; Kim, H.; et al. Surface-Loaded Metal Nanoparticles for Peroxymonosulfate Activation: Efficiency and Mechanism Reconnaissance. *Appl. Catal. B Environ.* **2019**, *241*, 561–569.
39. Zhu, S.; Ho, S.H.; Jin, C.; et al. Nanostructured Manganese Oxides: Natural/Artificial Formation and Their Induced Catalysis for Wastewater Remediation. *Environ. Sci. Nano* **2020**, *7*, 368–396.
40. Gao, Y.; Wang, Q.; Ji, G.; et al. Degradation of Antibiotic Pollutants by Persulfate Activated with Various Carbon Materials. *Chem. Eng. J.* **2022**, *429*, 132387.
41. Ghauch, A.; Tuqan, A.; Kibbi, N. Naproxen Abatement by Thermally Activated Persulfate in Aqueous Systems. *Chem. Eng. J.* **2015**, *279*, 861–873.
42. Zhang, B.; Li, X.; Akiyama, K.; et al. Elucidating the Mechanistic Origin of a Spin State-Dependent $FeN_x$-C Catalyst toward Organic Contaminant Oxidation via Peroxymonosulfate Activation. *Environ. Sci. Technol.* **2021**, *56*, 1321–1330.

43. Eghbali, P.; Hassani, A.; Wacławek, S.; et al. Recent Advances in Design and Engineering of MXene-Based Catalysts for Photocatalysis and Persulfate-Based Advanced Oxidation Processes: A State-of-the-Art Review. *Chem. Eng. J.* **2024**, *480*, 147920.
44. Wang, X.; Li, W.; Zhang, J.; et al. $Cu_2(OH)_3NO_3$/γ-$Al_2O_3$ Catalyzes Fenton-Like Oxidation for the Advanced Treatment of Effluent Organic Matter (EfOM) in Fermentation Pharmaceutical Wastewater: The Synergy of $Cu_2(OH)_3NO_3$ and γ-$Al_2O_3$. *Water Res.* **2024**, *261*, 122049.
45. Zhou, H.; He, Y.; Peng, J.; et al. High-Valent Metal-Oxo Species Transformation and Regulation by Co-Existing Chloride: Reaction Pathways and Impacts on the Generation of Chlorinated By-Products. *Water Res.* **2024**, *257*, 121715.
46. Chen, T.; Zhang, G.; Sun, H.; et al. Robust Fe-$N_4$-$C_6O_2$ Single Atom Sites for Efficient PMS Activation and Enhanced $Fe^{IV}$=O Reactivity. *Nat. Commun.* **2025**, *16*, 2402.
47. Lee, J.; Vogunten, U.; Kim, J. Persulfate-Based Advanced Oxidation: Critical Assessment of Opportunities and Roadblocks. *Environ. Sci. Technol.* **2020**, *54*, 3064–3081.
48. Yang, J.; Zhu, M.; Dionysiou, D. What Is the Role of Light in Persulfate-Based Advanced Oxidation for Water Treatment? *Water Res.* **2021**, *189*, 116627.
49. Zheng, X.; Niu, X.; Zhang, D.; et al. Metal-Based Catalysts for Persulfate and Peroxymonosulfate Activation in Heterogeneous Ways: A Review. *Chem. Eng. J.* **2022**, *429*, 132323.
50. Yang, Q.; Deng, J.; Wu, T.; et al. Node-Activated Persulfate Reduction in a Terbium Metal–Organic Framework for Low-Potential Electrochemiluminescence and Hydroquinone Sensing. *Anal. Chem.* **2026**, *98*, 13112–13119.
51. Cheng, D.; Ding, W.; Ye, H.; et al. The Mediating Roles of Aluminosilicate Minerals in Heat-Activated Persulfate Reactivity and Implications for *in Situ* Chemical Oxidation Remediation of Contaminated Sites. *J. Environ. Chem. Eng.* **2026**, *14*, 122438.
52. He, H.; Xie, J.; Liu, Y.; et al. Differential Degradation of Organic Pollutants Based on Their Molecular Properties in BiOCl Photocatalytic and Persulfate Photoactivated Systems: Adsorption-Dependent Degradation Mechanism Analysis. *J. Colloid Interface Sci.* **2026**, *708*, 139826.
53. Li, J.; Wang, T.; Liang, E. Carbon and Hydrogen Isotopic Evidence for Atrazine Degradation by Electro-Activated Persulfate: Radical Contributions and Comparisons with Heat-Activated Persulfate. *Environ. Pollut.* **2023**, *341*, 122892.
54. Chen, Z.; Zhu, E.; Luo, C.; et al. Ultrasound-Persulfate Synergistic Strategy Enables Efficient Iron Removal via Goethite Crystallization. *Sep. Purif. Technol.* **2026**, *395*, 137879.
55. Li, S.; Jing, B.; Sun, Y.; et al. Asymmetric Chemical Bond Modified CuO *In-Situ* Grown on Copper Foam Cooperates with Pollutants to Promote Copper Valence Cycling in Peroxymonosulfate Activation. *Appl. Catal. B Environ.* **2026**, *391*, 126697.
56. Yao, X.; Wang, H.; Liu, J.; et al. Electroactivated Cobalt-Cobalt Prussian Blue Analog Composite Membrane for Rapid Persulfate-Driven Antibiotic Degradation and Fouling Mitigation. *Chem. Eng. J.* **2026**, *528*, 172478.
57. Li, X.; Cheng, H. Crucial Role of *In-Situ* Formed Mn(III) Species in Pollutant Degradation by Persulfate Activated with Fe-Mn Binary Oxide-Modified Biochar. *Water Res.* **2026**, *295*, 125567.
58. Firouzan, G.; Rasoulifard, M.H.; Seyed Dorraji, M.S.; et al. Engineering a Pulsed UVA-LED/Persulfate System Guided by Parrondo's Paradox for Efficient Degradation of Emerging Pharmaceutical Pollutants and Electrical Energy Optimization. *Ind. Eng. Chem. Res.* **2026**, *65*, 2493–2501.
59. Qian, K.; Chen, H.; Li, W.; et al. Single-Atom Fe Catalyst Outperforms Its Homogeneous Counterpart for Activating Peroxymonosulfate to Achieve Effective Degradation of Organic Contaminants. *Environ. Sci. Technol.* **2021**, *55*, 7034–7043.
60. Li, S.; Fan, X.; Gu, M.; et al. Confined-Space Strategy for Anchoring Catalytic Nanoparticles on Si-OH by Ball Milling for Enhanced $O_3$/PMS Oxidation of Ciprofloxacin. *Chem. Eng. J.* **2022**, *429*, 132318.
61. Liu, H.Z.; Shu, X.X.; Huang, M.; et al. Tailoring d-Band Center of High-Valent Metal-Oxo Species for Pollutant Removal via Complete Polymerization. *Nat. Commun.* **2024**, *15*, 2327.
62. Zhao, X.; Jia, X.; Li, H.; et al. Efficient Degradation of Health-Threatening Organic Pollutants in Water by Atomically Dispersed Cobalt-Activated Peroxymonosulfate. *Chem. Eng. J.* **2022**, *450*, 138098.
63. Cao, M.; Xu, P.; Shi, F.; et al. Ultra-Fast Atrazine Degradation through Synergistic Enhancement: Exploring the Synergistic Mechanism of $CoFe_2O_4$/MXene and Thermal on Peroxymonosulfate Activation. *Chem. Eng. J.* **2024**, *497*, 154388.
64. Li, X.; Wang, S.; Chen, P.; et al. ZIF-Derived Non-Bonding Co/Zn Coordinated Hollow Carbon Nitride for Enhanced Removal of Antibiotic Contaminants by Peroxymonosulfate Activation: Performance and Mechanism. *Appl. Catal. B Environ.* **2023**, *325*, 122401.
65. Jiang, N.; Xu, H.; Wang, L.; et al. Nonradical Oxidation of Pollutants with Single-Atom-Fe(III)-Activated Persulfate: Fe(V) Being the Possible Intermediate Oxidant. *Environ. Sci. Technol.* **2020**, *54*, 14057–14065.
66. Wang, S.Z.; Xu, L.J.; Wang, J.L. Iron-Based Dual Active Site-Mediated Peroxymonosulfate Activation for the Degradation of Emerging Organic Pollutants. *Environ. Sci. Technol.* **2021**, *55*, 15412–15422.

67. Zhen, Y.; Zhu, S.; Sun, Z.; et al. Identifying the Persistent Free Radicals (PFRs) Formed as Crucial Metastable Intermediates during Peroxymonosulfate (PMS) Activation by N-Doped Carbonaceous Materials. *Environ. Sci. Technol.* **2021**, *55*, 9293–9304.
68. Zhou, R.; Liu, S.; He, F.; et al. Alkylpolyglycoside Modified $MnFe_2O_4$ with Abundant Oxygen Vacancies Boosting Singlet Oxygen Dominated Peroxymonosulfate Activation for Organic Pollutants Degradation. *Chemosphere* **2021**, *285*, 131433.
69. Wu, J.; Wang, B.; Blaney, L.; et al. Degradation of Sulfamethazine by Persulfate Activated with Organo-Montmorillonite Supported Nano-Zero Valent Iron. *Chem. Eng. J.* **2019**, *361*, 99–108.
70. Zhu, C.; Liu, F.; Ling, C.; et al. Growth of Graphene-Supported Hollow Cobalt Sulfide Nanocrystals via MOF-Templated Ligand Exchange as Surface-Bound Radical Sinks for Highly Efficient Bisphenol A Degradation. *Appl. Catal. B Environ.* **2019**, *242*, 238–248.
71. Nekouei, F.; Nekouei, S.; Kargarzadeh, H. Enhanced Adsorption and Catalytic Oxidation of Ciprofloxacin on Hierarchical CuS Hollow Nanospheres@N-Doped Cellulose Nanocrystals Hybrid Composites: Kinetic and Radical Generation Mechanism Studies. *Chem. Eng. J.* **2018**, *335*, 567–578.
72. Zhu, Y.; Wei, G.; Ma, J.; et al. Flower-Like Bentonite-Based $Co_3O_4$ with Oxygen Vacancies-Rich as Highly Efficient Peroxymonosulfate Activator for Lomefloxacin Hydrochloride Degradation. *Chem. Eng. J.* **2023**, *455*, 140673.
73. Zhou, H.; Lai, L.; Wan, Y.; et al. Molybdenum Disulfide ($MoS_2$): A Versatile Activator of Both Peroxymonosulfate and Persulfate for the Degradation of Carbamazepine. *Chem. Eng. J.* **2020**, *384*, 123264.
74. Tian, Q.; Chang, J.; Yu, B.; et al. Co-Catalysis Strategy for Low-Oxidant-Consumption Fenton-Like Chemistry: From Theoretical Understandings to Practical Applications and Future Guiding Strategies. *Water Res.* **2024**, *267*, 122488.
75. Duan, X.; Su, C.; Miao, J.; et al. Insights into Perovskite-Catalyzed Peroxymonosulfate Activation: Maneuverable Cobalt Sites for Promoted Evolution of Sulfate Radicals. *Appl. Catal. B Environ.* **2018**, *220*, 626–634.
76. He, Z.; Chen, M.; Xu, M.; et al. $LaCo_{0.5}Ni_{0.5}O_3$ Perovskite for Efficient Sulfafurazole Degradation via Peroxymonosulfate Activation: Catalytic Mechanism of Interfacial Structure. *Appl. Catal. B Environ.* **2023**, *335*, 122883.
77. Shen, Y.; Martín, D.; Gorni, G.; et al. Composition-Dependent PMS Activation in $Sr_xLa_{2-x}CoO_{4\pm\delta}$ Perovskite-Derivatives: From Radical to Strengthen the Electron-Transfer Pathway. *Appl. Catal. B Environ.* **2024**, *357*, 124291.
78. Kang, Y.; Hong, S.; Yoon, H.; et al. Mechanically Combined Persulfate on Zerovalent Iron: Mechanistic Insights into Reduction and Oxidation Processes. *Chem. Eng. J.* **2021**, *414*, 128772.
79. Liu, H.; Dai, X.; Kong, L.; et al. Ball Milling Treatment of $Mn_3O_4$ Regulates Electron Transfer Pathway for Peroxymonosulfate Activation. *Chem. Eng. J.* **2023**, *467*, 143339.
80. Hu, P.; Su, H.; Chen, Z.; et al. Selective Degradation of Organic Pollutants Using an Efficient Metal-Free Catalyst Derived from Carbonized Polypyrrole via Peroxymonosulfate Activation. *Environ. Sci. Technol.* **2017**, *51*, 11288–11296.
81. Bao, Y.; Lian, C.; Huang, K.; et al. Generating High-Valent Iron-Oxo $\equiv Fe^{IV}=O$ Complexes in Neutral Microenvironments through Peroxymonosulfate Activation by Zn-Fe Layered Double Hydroxides. *Angew. Chem. Int. Ed.* **2022**, *61*, e202209542.
82. Ke, M.; Huang, G.; Mei, S.; et al. Interface-Promoted Direct Oxidation of Parsanilic Acid and Removal of Total Arsenic by the Coupling of Peroxymonosulfate and Mn-Fe-Mixed Oxide. *Environ. Sci. Technol.* **2021**, *55*, 7063–7071.
83. Zhu, S.; Li, H.; Wang, L.; et al. Oxygen Vacancies-Rich α@δ-$MnO_2$ Mediated Activation of Peroxymonosulfate for the Degradation of CIP: The Role of Electron Transfer Process on the Surface. *Chem. Eng. J.* **2023**, *458*, 141415.
84. Wu, L.; Sun, Z.; Zhen, Y.; et al. Oxygen Vacancy-Induced Nonradical Degradation of Organics: Critical Trigger of Oxygen ($O_2$) in the Fe-Co LDH/Peroxymonosulfate System. *Environ. Sci. Technol.* **2021**, *55*, 15400–15411.
85. Zhang, M.; Tao, H.; Zhai, C.; et al. Twin-Brush ZnO Mesocrystal for the Piezo-Activation of Peroxymonosulfate to Remove Ibuprofen in Water: Performance and Mechanism. *Appl. Catal. B Environ.* **2023**, *326*, 122399.
86. Wang, M.; Liu, L.; Wen, J.; et al. Multimetallic CuCoNi Oxide Nanowires *in Situ* Grown on a Nickel Foam Substrate Catalyze Persulfate Activation via Mediating Electron Transfer. *Environ. Sci. Technol.* **2022**, *56*, 12613–12624.
87. Bi, G.; Ding, R.; Song, J.; et al. Discriminating the Active Ru Species towards the Selective Generation of Singlet Oxygen from Peroxymonosulfate: Nanoparticles Surpass Single-Atom Catalysts. *Angew. Chem. Int. Ed.* **2024**, *136*, e202401551.
88. Dong, Q.; Dong, H.; Li, Y.; et al. Degradation of Sulfamethazine in Water by Sulfite Activated with Zero-Valent Fe-Cu Bimetallic Nanoparticles. *J. Hazard. Mater.* **2022**, *431*, 128601.
89. Li, X.; Zhang, H.; Liu, J.; et al. Revealing the Overlooked Catalytic Ability of γ-$Al_2O_3$: Efficient Activation of Peroxymonosulfate for Enhanced Water Treatment. *Environ. Sci. Technol.* **2024**, *58*, 22466–22476.
90. Li, B.; Xu, H.; Liu, Y.; et al. Unveiling the Structure–Activity Relationships of Ofloxacin Degradation by $Co_3O_4$-Activated Peroxymonosulfate: From Microstructures to Exposed Facets. *Chem. Eng. J.* **2023**, *467*, 143396.
91. Wang, F.; Yang, F.; Yang, J.; et al. Synthesis of a Cu-Al Bimetallic Oxide @ PVDF Composite Membrane for the Degradation of Bisphenol A via Peroxydisulfate Activation: Performance and Mechanism. *Sep. Purif. Technol.* **2024**, *346*, 127504.

92. Song, C.; Zhan, Q.; Liu, F.; et al. Overturned Loading of Inert $CeO_2$ to Active $Co_3O_4$ for Unusually Improved Catalytic Activity in Fenton-Like Reactions. *Angew. Chem. Int. Ed.* **2022**, *61*, e202200406.
93. Hu, L.; Zhang, G.; Wang, Q.; et al. Facile Synthesis of Novel $Co_3O_4$-$Bi_2O_3$ Catalysts and Their Catalytic Activity on Bisphenol A by Peroxymonosulfate Activation. *Chem. Eng. J.* **2017**, *326*, 1095–1104.
94. Li, W.; Wu, P.; Zhu, Y.; et al. Catalytic Degradation of Bisphenol A by CoMnAl Mixed Metal Oxides Catalyzed Peroxymonosulfate: Performance and Mechanism. *Chem. Eng. J.* **2015**, *279*, 93–102.
95. Zhang, T.; Lv, Z.; Zhao, Q.; et al. Deep Insights into the Enhanced Waste Active Sludge Lysis by $MoS_2$ and $Fe^{2+}$ Co-Activated Persulfate. *Chem. Eng. J.* **2024**, *497*, 154423
96. Zhu, Z.; Ye, J.; Tang, X.; et al. Vacancy-Rich $CoS_x$@LDH@Co-NC Catalytic Membrane for Antibiotic Degradation with Mechanistic Insights. *Environ. Sci. Technol.* **2023**, *57*, 16131–16140.
97. Lian, Z.; Wu, T.; Zhang, X.; et al. Synergistic Degradation of Tetracycline from $Mo_2C$/MoO Films Mediated Peroxymonosulfate Activation and Visible-Light Triggered Photocatalysis. *Chem. Eng. J.* **2023**, *469*, 143774.
98. Si, Y.; Guo, Z.; Meng, Y.; et al. Reusing Sulfur-Poisoned Palladium Waste as a Highly Active, Nonradical Fenton-Like Catalyst for Selective Degradation of Phenolic Pollutants. *Environ. Sci. Technol.* **2022**, *56*, 564–574.
99. Zheng, N.; He, X.; Hu, R.; et al. Co-Activation of Persulfate by Cation and Anion from FeP for Advanced Oxidation Processes. *Appl. Catal. B Environ.* **2021**, *298*, 120505.
100. Huang, J.; Zhou, Y.; Deng, S.; et al. Photo-Assisted Reductive Cleavage and Catalytic Hydrolysis-Mediated Persulfate Activation by Mixed Redox-Couple-Involved $CuFeS_2$ for Efficient Trichloroethylene Oxidation in Groundwater. *Water Res.* **2022**, *222*, 118885.
101. Feng, Y.; Li, H.; Lin, L.; et al. Degradation of 1,4-Dioxane via Controlled Generation of Radicals by Pyrite-Activated Oxidants: Synergistic Effects, Role of Disulfides, and Activation Sites. *Chem. Eng. J.* **2018**, *336*, 416–426.
102. Nie, W.; Mao, Q.; Ding, Y.; et al. Highly Efficient Catalysis of Chalcopyrite with Surface Bonded Ferrous Species for Activation of Peroxymonosulfate toward Degradation of Bisphenol A: A Mechanism Study. *J. Hazard. Mater.* **2019**, *364*, 59–68.
103. Wang, J.L.; Wang, S.Z. A Critical Review on Graphitic Carbon Nitride (g-$C_3N_4$)-Based Materials: Preparation, Modification and Environmental Application. *Coord. Chem. Rev.* **2022**, *453*, 214338.
104. Wang, S.Z.; Wang, J.L. Single Atom Cobalt Catalyst Derived from Co-Pyrolysis of Vitamin $B_{12}$ and Graphitic Carbon Nitride for PMS Activation to Degrade Emerging Pollutants. *Appl. Catal. B Environ.* **2023**, *321*, 122051.
105. Fang, Q.; Yang, H.; Ye, S.; et al. Generation and Identification of $^1O_2$ in Catalysts/Peroxymonosulfate Systems for Water Purification. *Water Res.* **2023**, *245*, 120614.
106. Hu, P.; Long, M. Cobalt-Catalyzed Sulfate Radical-Based Advanced Oxidation: A Review on Heterogeneous Catalysts and Applications. *Appl. Catal. B Environ.* **2016**, *181*, 103–117.
107. Hu, L.; Yang, F.; Zou, L.; et al. CoFe/SBA-15 Catalyst Coupled with Peroxymonosulfate for Heterogeneous Catalytic Degradation of Rhodamine B in Water. *Chin. J. Catal.* **2015**, *36*, 1785–1797.
108. Yan, J.; Gao, W.; Dong, M.; et al. Degradation of Trichloroethylene by Activated Persulfate Using a Reduced Graphene Oxide Supported Magnetite Nanoparticle. *Chem. Eng. J.* **2016**, *295*, 309–316.
109. Fu, C.; Yi, X.; Abdelhaleem, A.; et al. Diphenamid Degradation via Sulfite Activation under Visible LED Using Fe(III) Impregnated N-Doped $TiO_2$ Photocatalyst. *Appl. Catal. B Environ. Environ.* **2019**, *244*, 823–835.
110. Oh, W.; Wong, Z.; Chen, X.; et al. Enhanced Activation of Peroxydisulfate by CuO Decorated on Hexagonal Boron Nitride for Bisphenol A Removal. *Chem. Eng. J.* **2020**, *393*, 124714.
111. Tang, H.; Shang, Q.; Tang, Y.; et al. Filter-Membrane Treatment of Flowing Antibiotic-Containing Wastewater through Peroxydisulfate-Coupled Photocatalysis to Reduce Resistance Gene and Microbial Inhibition during Biological Treatment. *Water Res.* **2021**, *207*, 117819.
112. Zhang, X.; Feng, M.; Qu, R.; et al. Catalytic Degradation of Diethyl Phthalate in Aqueous Solution by Persulfate Activated with Nano-Scaled Magnetic $CuFe_2O_4$/MWCNTs. *Chem. Eng. J.* **2016**, *301*, 1–11.
113. Jorfi, S.; Kakavandi, B.; Motlagh, H.; et al. A Novel Combination of Oxidative Degradation for Benzotriazole Removal Using $TiO_2$ Loaded on $Fe^{II}Fe_2^{III}O_4$@C as an Efficient Activator of Peroxymonosulfate. *Appl. Catal. B Environ.* **2017**, *219*, 216–230.
114. Li, H.; Wan, J.; Ma, Y.; et al. Degradation of Refractory Dibutyl Phthalate by Peroxymonosulfate Activated with Novel Catalysts Cobalt Metal-Organic Frameworks: Mechanism, Performance, and Stability. *J. Hazard. Mater.* **2016**, *318*, 154–163.
115. Feng, Y.; Lee, P.H.; Wu, D.; et al. Surface-Bound Sulfate Radical-Dominated Degradation of 1,4-Dioxane by Alumina-Supported Palladium (Pd/$Al_2O_3$) Catalyzed Peroxymonosulfate. *Water Res.* **2017**, *120*, 12–21.
116. Du, J.; Bao, J.; Liu, Y.; et al. Efficient Activation of Peroxymonosulfate by Magnetic Mn-MGO for Degradation of Bisphenol A. *J. Hazard. Mater.* **2016**, *320*, 150–159.

117. Qian, L.; Liu, P.; Shao, S.; et al. An Efficient Graphene Supported Copper Salen Catalyst for the Activation of Persulfate to Remove Chlorophenols in Aqueous Solution. *Chem. Eng. J.* **2019**, *360*, 54–63.
118. Pi, Y.; Ma, L.; Zhao, P.; et al. Facile Green Synthetic Graphene-Based Co-Fe Prussian Blue Analogues as an Activator of Peroxymonosulfate for the Degradation of Levofloxacin Hydrochloride. *J. Colloid Interface Sci.* **2018**, *526*, 18–27.
119. Li, W.; Liu, B.; Wang, Z.; et al. Efficient Activation of Peroxydisulfate (PDS) by Rice Straw Biochar Modified by Copper Oxide (RSBC-CuO) for the Degradation of Phenacetin (PNT). *Chem. Eng. J.* **2020**, *395*, 125094.
120. Hong, Y.; Zhou, H.; Xiong, Z.; et al. Heterogeneous Activation of Peroxymonosulfate by CoMgFe-LDO for Degradation of Carbamazepine: Efficiency, Mechanism and Degradation Pathways. *Chem. Eng. J.* **2020**, *391*, 123604.
121. Huang, J.; Li, D.; Liu, Y.; et al. Ultrathin $Ag_2WO_4$-Coated P-Doped g-$C_3N_4$ Nanosheets with Remarkable Photocatalytic Performance for Indomethacin Degradation. *J. Hazard. Mater.* **2020**, *392*, 122355.
122. Feng, M.; Qu, R.; Zhang, X.; et al. Degradation of Flumequine in Aqueous Solution by Persulfate Activated with Common Methods and Polyhydroquinone-Coated Magnetite Multi-Walled Carbon Nanotubes Catalysts. *Water Res.* **2015**, *85*, 1–10.
123. Dong, Y.; Wang, P.; Li, B. Fe Complex Immobilized on Waste Polypropylene Fibers for Fast Degradation of Reactive Red 195 via Enhanced Activation of Persulfate under LED Visible Irradiation. *J. Clean. Prod.* **2019**, *208*, 1347–1356.
124. Lin, H.; Zhong, X.; Ciotonea, C.; et al. Efficient Degradation of Clofibric Acid by Electro-Enhanced Peroxydisulfate Activation with Fe-Cu/SBA-15 Catalyst. *Appl. Catal. B Environ.* **2018**, *230*, 1–10.
125. Marinescu, C.; Ali, M.; Hamdi, A.; et al. Cobalt Phthalocyanine-Supported Reduced Graphene Oxide: A Highly Efficient Catalyst for Heterogeneous Activation of Peroxymonosulfate for Rhodamine B and Pentachlorophenol Degradation. *Chem. Eng. J.* **2018**, *336*, 465–475.
126. Yan, J.; Han, L.; Gao, W.; et al. Biochar Supported Nanoscale Zerovalent Iron Composite Used as Persulfate Activator for Removing Trichloroethylene. *Bioresour. Technol.* **2015**, *175*, 269–274.
127. Shao, H.; Zhao, X.; Wang, Y.; et al. Synergetic Activation of Peroxymonosulfate by $Co_3O_4$ Modified g-$C_3N_4$ for Enhanced Degradation of Diclofenac Sodium under Visible Light Irradiation. *Appl. Catal. B Environ.* **2017**, *218*, 810–818.
128. Wu, D.; Ye, P.; Wang, M.; et al. Cobalt Nanoparticles Encapsulated in Nitrogen-Rich Carbon Nanotubes as Efficient Catalysts for Organic Pollutants Degradation via Sulfite Activation. *J. Hazard. Mater.* **2018**, *352*, 148–156.
129. Ma, Q.; Zhang, H.; Zhang, X.; et al. Synthesis of magnetic CuO/$MnFe_2O_4$ Nanocompisite and Its High Activity for Degradation of Levofloxacin by Activation of Persulfate. *Chem. Eng. J.* **2019**, *360*, 848–860.
130. Fu, H.; Ma, S.; Zhao, P.; et al. Activation of Peroxymonosulfate by Graphitized Hierarchical Porous Biochar and $MnFe_2O_4$ Magnetic Nanoarchitecture for Organic Pollutants Degradation: Structure Dependence and Mechanism. *Chem. Eng. J.* **2019**, *360*, 157–170.
131. Zhuang, Y.; Wang, X.; Zhang, L.; et al. Double-Network Hydrogel Templated FeS/Graphene with Enhanced PMS Activation Performance: Considering the Effect of the Template and Iron Species. *Environ. Sci. Nano* **2020**, *7*, 817–828
132. Zhang, Y.; Zhang, B.; Teng, Y.; et al. Carbon Nanofibers Supported Co/Ag Bimetallic Nanoparticles for Heterogeneous Activation of Peroxymonosulfate and Efficient Oxidation of Amoxicillin. *J. Hazard. Mater*. **2020**, *400*, 123290.
133. Wu, Q.; Zhang, Y.; Liu, H.; et al. $Fe_xN$ Produced in Pharmaceutical Sludge Biochar by Endogenous Fe and Exogenous N Doping to Enhance Peroxymonosulfate Activation for Levofloxacin Degradation. *Water Res.* **2022**, *224*, 119022.
134. Miao, J.; Song, J.; Lang, J.; et al. Single-Atom $MnN_5$ Catalytic Sites Enable Efficient Peroxymonosulfate Activation by Forming Highly Reactive Mn(IV)-Oxo Species. *Environ. Sci. Technol.* **2023**, *57*, 4266–4275.
135. Yang, M.; Hou, Z.; Zhang, X.; et al. Unveiling the Origins of Selective Oxidation in Single-Atom Catalysis via Co-$N_4$-C Intensified Radical and Nonradical Pathways. *Environ. Sci. Technol.* **2022**, *56*, 11635–11645.
136. Tian, Q.; Chang, J.; Peng, X.; et al. Iron Single-Atom Based Double-Reaction-Center Catalysis Triggers Internal-Driven and External-Driven Pathways for Green Fenton-Like Chemistry. *Angew. Chem. Int. Ed.* **2025**, *64*, e202503995.
137. Wang, F.; Gao, Y.; Fu, H.; et al. Almost 100% Electron Transfer Regime over Fe-Co Dual-Atom Catalyst toward Pollutants Removal: Regulation of Peroxymonosulfate Adsorption Mode. *Appl. Catal. B Environ.* **2023**, *339*, 123178.
138. Chen, C.; Yan, M.; Li, Y.; et al. Single-Atom Co Sites Confined in Layered Double Hydroxide for Selective Generation of Surface-Bound Radicals via Peroxymonosulfate Activation. *Appl. Catal. B Environ.* **2024**, *340*, 123218.
139. Chu, C.; Yang, J.; Zhou, X.; et al. Cobalt Single Atoms on Tetrapyridomacrocyclic Support for Efficient Peroxymonosulfate Activation. *Environ. Sci. Technol.* **2020**, *55*, 1242–1250.
140. Wu, X.; Rigby, K.; Huang, D. Single-Atom Cobalt Incorporated in a 2D Graphene Oxide Membrane for Catalytic Pollutant Degradation. *Environ. Sci. Technol.* **2022**, *56*, 1341–1351.
141. Gong, H.; Zhang, L.; Deng, C.; et al. Selective Photocatalytic Aerobic Oxidation of Methane to Methyl Hydroperoxide by ZnO-Loaded Single-Atomic Ruthenium Oxide Catalyst. *J. Am. Chem. Soc.* **2025**, *147*, 119134–119146.
142. Wang, B.; Cheng, C.; Jin, M.; et al. A Site Distance Effect Induced by Reactant Molecule Matchup in Single-Atom Catalysts for Fenton-Like Reactions. *Angew. Chem. Int. Ed.* **2022**, *61*, e202207268.

143. Liu, C.; Li, J.; He, X.; et al. The "4 + 1" Strategy Fabrication of Iron Single-Atom Catalysts with Selective High-Valent Iron-Oxo Species Generation. *Proc. Natl. Acad. Sci. USA* **2024**, *121*, e2322283121.
144. Zhang, W.; Huang, L.; Guo, W.; et al. Ultrafast Peroxymonosulfate Activation via an Easily Synthesized Cobalt Cluster for Selective Cobalt(IV)=O Generation. *Environ. Sci. Technol.* **2025**, *59*, 23622–23632.
145. Zhang, L.; Jiang, X.; Zhong, Z.; et al. Carbon Nitride Supported High-Loading Fe Single-Atom Catalyst for Activation of Peroxymonosulfate to Generate $^1O_2$ with 100% Selectivity. *Angew. Chem. Int. Ed.* **2021**, *60*, 21751–21755.
146. Jin, L.; You, S.; Ren, N.; et al. Mo Vacancy-Mediated Activation of Peroxymonosulfate for Ultrafast Micropollutant Removal Using an Electrified MXene Filter Functionalized with Fe Single Atoms. *Environ. Sci. Technol.* **2022**, *56*, 11750–11759.
147. Wei, R.; Wang, H.; Jiang, L.; et al. Molecular Self-Assembled Synthesis of Highly Dispersed Co Single-Atom Coordinated 2-Methylimidazole Modified Carbon Nitride for Peroxymonosulfate Activation. *Chem. Eng. J.* **2023**, *471*, 144494.
148. Yang, J.; Zeng, D.; Zhang, Q.; et al. Single Mn Atom Anchored on N-Doped Porous Carbon as Highly Efficient Fenton-Like Catalyst for the Degradation of Organic Contaminants. *Appl. Catal. B Environ.* **2020**, *279*, 119363.
149. Zhu, Z.; Wang, Y.; Wang, P.; et al. Multidimensional Engineering of Single-Atom Cobalt Catalysts for Ultrafast Fenton-Like Reactions. *Nat. Water* **2025**, *3*, 211–221.
150. Liu, X.; Zhang, J.; Wang, S.; et al. Coordination Dependent Photocatalytic Peroxymonosulfate Activation on Biomass Derived Fe Single Atom Catalysts for Atrazine Degradation. *Chem. Eng. J.* **2024**, *499*, 156625
151. Yin, K.; Xu, X.; Yue, Q.; et al. Pore Modulation of Single Atomic Fe Sites for Ultrafast Fenton-Like Chemistry with Amplified Electron Migration Oxidation. *Water Res.* **2025**, *268*, 122545.
152. Chen, F.; Sun, Y.; Huang, X.; et al. Embedding Electronic Perpetual Motion into Single-Atom Catalysts for Persistent Fenton-Like Reactions. *Proc. Natl. Acad. Sci. USA* **2024**, *121*, e2314396121.
153. Guo, J.; Wang, Y.; Shang, Y.; et al. Fenton-Like Activity and Pathway Modulation via Single-Atom Sites and Pollutants Comediates the Electron Transfer Process. *Proc. Natl. Acad. Sci. USA* **2024**, *121*, e2313387121.
154. Zhu, G.; Fan, X.; Yu, Y.; et al. Regulating the Electronic Structure of Cu Single-Atom Catalysts toward Enhanced Electro-Fenton Degradation of Organic Contaminants via $^1O_2$ and $^{\bullet}OH$. *Environ. Sci. Technol.* **2024**, *58*, 19545–19554.
155. Yue, N.; Yang, J.; Li, P.; et al. Intensive Electron Transfer of a Single-Atom Fe-Based Catalytic Ceramic Membrane for Municipal Wastewater Treatment: The Synergistic Effects of Nitrogen Vacancy Defect and Ultrathin Nanostructure. *Water Res.* **2025**, *272*, 122983.
156. Li, S.; Wang, W.; Wu, H.; et al. Performance Enhancement and Mechanism of Electroenhanced Peroxymonosulfate Activation by Single-Atom Fe Catalyst Modified Electrodes. *Proc. Natl. Acad. Sci. USA* **2024**, *121*, e2404965121.
157. Huang, B.; Wu, Z.; Wang, X. Coupled Surface-Confinement Effect and Pore Engineering in a Single-Fe-Atom Catalyst for Ultrafast Fenton-Like Reaction with High-Valent Iron-Oxo Complex Oxidation. *Environ. Sci. Technol.* **2023**, *57*, 15667–15679.
158. Chai, Y.; Dai, H.; Duan, X.; et al. Elucidation of the Mechanistic Origin of Spin-State-Dependent P-Doped Fe Single-Atom Catalysts for the Oxidation of Organic Pollutants through Peroxymonosulfate Activation. *Appl. Catal. B Environ.* **2024**, *341*, 123289.
159. Mi, X.; Wang, P.; Xu, S.; et al. Almost 100% Peroxymonosulfate Conversion to Singlet Oxygen on Single-Atom $CoN_{2+2}$ Sites. *Angew. Chem. Int. Ed.* **2021**, *60*, 4588–4593.
160. Gao, Y.; Zhu, Y.; Li, T.; et al. Unraveling the High-Activity Origin of Single-Atom Iron Catalysts for Organic Pollutant Oxidation via Peroxymonosulfate Activation. *Environ. Sci. Technol.* **2021**, *55*, 8318–8328.
161. Shi, L.; Huang, G.; Wang, Z.; et al. Dual-Substrate Synergistic Catalysis for Highly Efficient Water Purification. *Nat. Water* **2025**, *3*, 345–353.
162. Gong, Y.; Chen, Z.; Wu, Y.; et al. Revisiting the Iron(II)/Cobalt(II)-Based Homogenous Fenton-Like Processes from the Standpoint of Diverse Metal-Oxygen Complexes. *Environ. Sci. Technol.* **2024**, *58*, 16589–16599.
163. Li, H.; Zhao, Z.; Qian, J.; et al. Are Free Radicals the Primary Reactive Species in Co(II)-Mediated Activation of Peroxymonosulfate? New Evidence for the Role of the Co(II)-Peroxymonosulfate Complex. *Environ. Sci. Technol.* **2021**, *55*, 6397–6406.
164. Chen, L.; Zuo, X.; Yang, S.; et al. Rational Design and Synthesis of Hollow $Co_3O_4$@$Fe_2O_3$ Core-Shell Nanostructure for the Catalytic Degradation of Norfloxacin by Coupling with Peroxymonosulfate. *Chem. Eng. J.* **2024**, *359*, 373–384.
165. Zhang, P.; Yang, Y.; Duan, X.; et al. Density Functional Theory Calculations for Insight into the Heterocatalyst Reactivity and Mechanism in Persulfate-Based Advanced Oxidation Reactions. *ACS Catal.* **2021**, *11*, 11129–11159.
166. Zhou, X.; Zhao, Q.; Wang, J.; et al. Nonradical Oxidation Processes in PMS-Based Heterogeneous Catalytic System: Generation, Identification, Oxidation Characteristics, Challenges Response and Application Prospects. *Chem. Eng. J.* **2021**, *410*, 128312.
167. Liu, Y.; Zhou, H. $Cu^{2+}$ Activated Persulfate for Sulfamethazine Degradation. *Chemosphere* **2020**, *257*, 127294.

168. Chen, M.; Zhu, L.; Liu, S.; et al. Efficient Degradation of Organic Pollutants by Low-Level $Co^{2+}$ Catalyzed Homogeneous Activation of Peroxymonosulfate. *J. Hazard. Mater.* **2019**, *371*, 456–462.
169. Ling, L.; Zhang, D.; Fan, C.; et al. A Fe(II)/Citrate/UV/PMS Process for Carbamazepine Degradation at a Very Low Fe(II)/PMS Ratio and Neutral pH: The Mechanisms. *Water Res.* **2017**, *124*, 446–453.
170. Zeng, Y.; He, D.; Sun, J.; et al. Non-Radical Oxidation Driven by Iron-Based Materials without Energy Assistance in Wastewater Treatment. *Water Res.* **2024**, *264*, 122255.
171. Gao, Y.; Zhou, Y.; Pang, S.; et al. Enhanced Peroxymonosulfate Activation via Complexed Mn(II): A Novel Non-Radical Oxidation Mechanism Involving Manganese Intermediates. *Water Res.* **2021**, *193*, 116856.
172. Yang, Z.; Cui, Y.; Pan, B.; et al. Peroxymonosulfate Activation by Fe(III)-Picolinate Complexes for Efficient Water Treatment at Circumneutral pH: Fe(III)/Fe(IV) Cycle and Generation of Oxyl Radicals. *Environ. Sci. Technol.* **2023**, *57*, 18918–18928.
173. Wang, Z.; Qiu, W.; Pang, S.; et al. Further Understanding the Involvement of Fe(IV) in Peroxydisulfate and Peroxymonosulfate Activation by Fe(II) for Oxidative Water Treatment. *Chem. Eng. J.* **2019**, *371*, 842–847.
174. Li, X.; Lv, R.; Zhang, W.; et al. Amorphous Zirconium Oxide Activates Peroxymonosulfate for Selective Degradation of Organic Compounds: Performance, Mechanisms and Structure-Activity Relationship. *Water Res.* **2023**, *228*, 119363.
175. Peng, X.; Yang, Z.; Hu, F.; et al. Mechanistic Investigation of Rapid Catalytic Degradation of Tetracycline Using $CoFe_2O_4$@$MoS_2$ by Activation of Peroxymonosulfate. *Sep. Purif. Technol.* **2022**, *287*, 120525.
176. Du, J.; Bao, J.; Liu, Y.; et al. Facile Preparation of Porous Mn/$Fe_3O_4$ Cubes as Peroxymonosulfate Activating Catalyst for Effective Bisphenol A Degradation. *Chem. Eng. J.* **2019**, *376*, 119193.
177. Xu, C.; Yang, G.; Li, J.; et al. Efficient Purification of Tetracycline Wastewater by Activated Persulfate with Heterogeneous Co-V Bimetallic Oxides. *J. Colloid Interface Sci.* **2022**, *619*, 188–197.
178. Li, H.; Yuan, N.; Qian, J.; et al. $Mn_2O_3$ as an Electron Shuttle between Peroxymonosulfate and Organic Pollutants: The Dominant Role of Surface Reactive Mn(IV) Species. *Environ. Sci. Technol.* **2022**, *56*, 4498–4506.
179. Wang, J.; Fan, J.; Yao, J.; et al. Facet Tailoring and Cu Doping Promoted Photo-Assisted Peroxymonosulfate Activation by Oxygen-Deficient α-$MnO_2$ for Efficient Mineralization of Bisphenol A. *Chem. Eng. J.* **2023**, *461*, 142024.
180. Wang, Z.; Xie, A.; Li, Z.; et al. Selective Oxidation of Electron-Rich Pollutants in Peroxymonosulfate-Activated Electro-Fenton System: The Role of Microenvironment-Regulated Cathode. *Water Res.* **2025**, *268*, 122699.
181. Wang, Y.; Bao, S.; Liu, X.; et al. Regulating the Peroxymonosulfate Activation on N Doped δ-$MnO_2$ Nanosheets for Tetracycline Degradation: N Species as the Degradation Pathways Switcher to Convert Radical to Nonradical. *Chem. Eng. J.* **2023**, *477*, 147050.
182. Wu, L.; Hong, J.; Zhang, Q.; et al. Deciphering Highly Resistant Characteristics to Different pHs of Oxygen Vacancy-Rich $Fe_2Co_1$-LDH/PS System for Bisphenol A Degradation. *Chem. Eng. J.* **2020**, *385*, 123260.
183. Ge, L.; Shao, B.; Liang, Q.; et al. Layered Double Hydroxide Based Materials Applied in Persulfate Based Advanced Oxidation Processes: Property, Mechanism, Application and Perspectives. *J. Hazard. Mater.* **2022**, *424*, 127612.
184. Huang, J.; Zhang, H. Mn-Based Catalysts for Sulfate Radical-Based Advanced Oxidation Processes: A Review. *Environ. Int.* **2019**, *133*, 105141.
185. Zhang, X.; Deng, H.; Zhang, G.; et al. Natural Bornite as an Efficient and Cost-Effective Persulfate Activator for Degradation of Tetracycline: Performance and Mechanism. *Chem. Eng. J.* **2020**, *381*, 122717.
186. Jing, J.; Wang, X.; Zhou, M. Electro-Enhanced Activation of Peroxymonosulfate by a Novel Perovskite-$Ti_4O_7$ Composite Anode with Ultra-High Efficiency and Low Energy Consumption: The Generation and Dominant Role of Singlet Oxygen. *Water Res.* **2023**, *232*, 119682.
187. Afzal, S.; Quan, X.; Zhang, J. High Surface Area Mesoporous Nanocast $LaMO_3$ (M = Mn, Fe) Perovskites for Efficient Catalytic Ozonation and an Insight into Probable Catalytic Mechanism. *Appl. Catal. B Environ.* **2017**, *206*, 692–703.
188. Liu, Y.; Guo, H.; Zhang, Y.; et al. Heterogeneous Activation of Peroxymonosulfate by Sillenite $Bi_{25}FeO_{40}$: Singlet Oxygen Generation and Degradation for Aquatic Levofloxacin. *Chem. Eng. J.* **2018**, *343*, 128–137.
189. Wang, Y.; Liu, M.; Hu, C.; et al. Enhanced $MnO_2$/Peroxymonosulfate Activation for Phthalic Acid Esters Degradation: Regulation of Oxygen Vacancy. *Chem. Eng. J.* **2022**, *433*, 134048.
190. Yuan, C.; Li, G.; Ran, M.; et al. Fe(III) Alleviates pH Dependence of Iron-Based Bimetallic/PMS System for Organic Pollutant Oxidation. *Appl. Catal. B Environ.* **2025**, *366*, 125002.
191. Deng, J.; Cheng, Y.; Lu, Y.; et al. Mesoporous Manganese Cobaltite Nanocages as Effective and Reusable Heterogeneous Peroxymonosulfate Activators for Carbamazepine Degradation. *Chem. Eng. J.* **2017**, *330*, 505–517.
192. Huang, M.; Li, Y.; Zhang, C.; et al. Facilely Tuning the Intrinsic Catalytic Sites of the Spinel Oxide for Peroxymonosulfate Activation: From Fundamental Investigation to Pilot-Scale Demonstration. *Proc. Natl. Acad. Sci. USA* **2022**, *119*, e2202682119.
193. Liu, Y.; Tian, L.; Huang, M.; et al. Magnesium Oxide-Supported Single Atoms with Fine-Modulated Steric Location for Polymerization Transfer Removal of Water Pollutants. *Environ. Sci. Technol.* **2024**, *59*, 880–891.

194. Gao, P.; Tian, X.; Fu, W.; et al. Copper in $LaMnO_3$ to Promote Peroxymonosulfate Activation by Regulating the Reactive Oxygen Species in Sulfamethoxazole Degradation. *J. Hazard. Mater.* **2021**, *411*, 125163.
195. Zhong, Q.; Sun, Y.; Xu, C.; et al. $Fe_xSe_y$@C Superlattice Nanocrystals for Peroxymonosulfate Activation: Intrinsic Nature of Fe Spin State. *Appl. Catal. B Environ.* **2023**, *339*, 123113.
196. Cong, Y.; Wang, Y.; Li, X.; et al. Modulation of Co Spin State at Crystalline-Amorphous Interfaces to Enhance Peroxymonosulfate Activation for Advanced Degradation of Florfenicol. *Appl. Catal. B Environ.* **2026**, *383*, 126090.
197. Fu, D.; Zhang, W.; Zhao, Z.; et al. Oxygen Vacancy-Mediated d-Band Center Regulation in $NiCu_{0.4}Fe_{1.6}O_4$ via Cu-Doping Achieves Efficient Peroxymonosulfate Activation for Durable Water Purification. *Appl. Catal. B Environ.* **2026**, *386*, 126420.
198. Quan, W.; Lu, W.; Luo, F.; et al. Engineering Coordination Environment of Cobalt Single-Atoms Integrated with Cobalt Nanoclusters to Construct d-Band Center Targeted Co(IV)=O and Accelerate PMS Activation. *Appl. Catal. B Environ.* **2026**, *390*, 126640.
199. Wang, L.; Guo, Z.; Hou, Y.; et al. Spin-Regulated Fe-Cu Diatomic Catalytic Chemistry Enables Significant Minimization of Catalyst Consumption with High-Efficiency Fenton-Like Activity. *Angew. Chem. Int. Ed.* **2026**, *65*, e200525747.
200. Liu, Y.; Zhou, A.; Duan, C.; et al. Dynamic Structural Evolution of Carbon Catalysts during Persulfate Activation Rewires Nonradical Pathways for Water Decontamination. *Water Res.* **2026**, *391*, 126100.
201. Lu, J.; Ding, A.; Wang, L.; et al. Spin States of Fe-$N_4$ Sites Regulates PMS Activation Pathways for Ultrafast Sulfamethoxazole Degradation. *Small* **2026**, *22*, e14930.
202. Li, Y.H.; Li, T.; Hu, X.; et al. Synchronous Increase in Spin-State Induced by Advanced 3d–4d Orbital Hybridization for Enhancing Radical Yield. *Adv. Funct. Mater.* **2025**, *35*, e14549.
203. Ma, D.; Huo, X.; Lai, C.; et al. Hollow Carbon Nanocage-Loaded Fe Single-Atom Mediated Electron Transfer Process for Antibiotics Removal: Coordination Environment and Mechanism Investigation. *Appl. Catal. B Environ.* **2026**, *381*, 125894.
204. Li, X.; Wang, Z.; Zhang, B.; et al. $FeCo_3$-$O_4$ Nanocages Derived from Nanoscale Metal–Organic Frameworks for Removal of Bisphenol A by Activation of Peroxymonosulfate. *Appl. Catal. B Environ.* **2016**, *181*, 788–799.
205. Ren, Y.; Lin, L.; Ma, J.; et al. Sulfate Radicals Induced from Peroxymonosulfate by Magnetic Ferrospinel $MFe_2O_4$ (M = Co, Cu, Mn, and Zn) as Heterogeneous Catalysts in the Water. *Appl. Catal. B Environ.* **2015**, *165*, 572–578.
206. Xu, L.; Sun, X.; Hong, J.; et al. Peroxymonosulfate Activation by α-$MnO_2$/$MnFe_2O_4$ for Norfloxacin Degradation: Efficiency and Mechanism. *J. Phys. Chem. Solids* **2021**, *153*, 110029.
207. Yang, Z.; Li, X.; Huang, Y.; et al. Facile Synthesis of Cobalt-Iron Layered Double Hydroxides Nanosheets for Direct Activation of Peroxymonosulfate (PMS) during Degradation of Fluoroquinolones Antibiotics. *J. Clean. Prod.* **2021**, *310*, 127584.
208. Lu, S.; Wang, G.; Chen, S.; et al. Heterogeneous Activation of Peroxymonosulfate by $LaCo_{1-x}Cu_xO_3$ Perovskites for Degradation of Organic Pollutants. *J. Hazard. Mater.* **2018**, *353*, 401–409.
209. Dong, H.; Qiang, Z.; Hu, J.; et al. Accelerated Degradation of Iopamidol in Iron Activated Persulfate Systems: Roles of Complexing Agents. *Chem. Eng. J.* **2017**, *316*, 288–295.
210. Yu, J.; Zeng, T.; Wang, H.; et al. Oxygen-Defective $MnO_{2-x}$ Rattle-Type Microspheres Mediated Singlet Oxygen Oxidation of Organics by Peroxymonosulfate Activation. *Chem. Eng. J.* **2020**, *394*, 124458.
211. Zaheer Afzal, M.; Zha, M.; Zhang, H.; et al. Copper-Incorporated Zinc Manganite as a Novel Catalyst for Activating Peroxymonosulfate in the Degradation of Tetracycline. *Sep. Purif. Technol.* **2025**, *354*, 128673.
212. Yang, X.; Duan, J.; Qi, J.; et al. Modulating the Electron Structure of Co-3d in $Co_3O_{4-x}$/$WO_{2.72}$ for Boosting Peroxymonosulfate Activation and Degradation of Sulfamerazine: Roles of High-Valence W and Rich Oxygen Vacancies. *J. Hazard. Mater.* **2023**, *445*, 130576.
213. Liu, S.; Du, J.; Wang, H.; et al. How Hetero-Single-Atom Dispersion Reconstructed Electronic Structure of Carbon Materials and Regulated Fenton-Like Oxidation Pathways. *Water Res.* **2024**, *254*, 121417.
214. Wang, X.; Xiong, Z.; Shi, H.; et al. Switching the Reaction Mechanisms and Pollutant Degradation Routes through Active Center Size-Dependent Fenton-Like Catalysis. *Appl. Catal. B Environ.* **2023**, *329*, 122569.
215. Tian, M.; Zhang, H.; Liu, Y.; et al. Breaking the Oxo-Wall for Co(IV)-Oxo Species and Their Nanoconfined Catalytic Performance within Ce-Co Lamellar Membrane. *Nat. Commun.* **2026**, *17*, 1767.
216. Zhou, X.; Ke, M.; Huang, G.; et al. Identification of Fenton-Like Active Cu Sites by Heteroatom Modulation of Electronic Density. *Proc. Natl. Acad. Sci. USA* **2022**, *119*, e2119492119.
217. Yin, K.; Wu, R.; Shang, Y.; et al. Microenvironment Modulation of Cobalt Single-Atom Catalysts for Boosting Both Radical Oxidation and Electron-Transfer Process in Fenton-Like System. *Appl. Catal. B Environ.* **2023**, *329*, 122558.
218. Li, Z.; Wang, L.; Liu, Y.; et al. Overlooked Enhancement of Chloride Ion on the Transformation of Reactive Species in Peroxymonosulfate/Fe(II)/$NH_2OH$ System. *Water Res.* **2021**, *195*, 116973.
219. Dong, Y.; He, C.; Sun, S.; et al. Mechanically Treated $Mn_2O_3$ Triggers Peracetic Acid Activation for Superior Non-Radical Oxidation of Micropollutants: Identification of Reactive Complexes. *Water Res.* **2024**, *255*, 121486.

220. Sheng, B.; Yang, F.; Wang, Y.; et al. Pivotal Roles of $MoS_2$ in Boosting Catalytic Degradation of Aqueous Organic Pollutants by Fe(II)/PMS. *Chem. Eng. J.* **2019**, *375*, 121989.
221. Liu, X.; Shao, P.; Gao, S.; et al. Benzoquinone-Assisted Heterogeneous Activation of PMS on $Fe_3S_4$ via Formation of Active Complexes to Mediate Electron Transfer towards Enhanced Bisphenol A Degradation. *Water Res.* **2022**, *226*, 119218.
222. Hu, J.; Tian, K.; Jiang, H. Improvement of Phenol Photodegradation Efficiency by a Combined g-$C_3N_4$/Fe(III)/Persulfate System. *Chemosphere* **2016**, *148*, 34–40.
223. Dong, L.; Xu, T.; Chen, W.; et al. Synergistic Multiple Active Species for the Photocatalytic Degradation of Contaminants by Imidazole-Modified g-$C_3N_4$ Coordination with Iron Phthalocyanine in the Presence of Peroxymonosulfate. *Chem. Eng. J.* **2019**, *357*, 198–208.
224. Chen, X.; Yao, J.; Dong, H.; et al. Enhanced Bezafibrate Degradation and Power Generation via the Simultaneous PMS Activation in Visible Light Photocatalytic Fuel Cell. *Water Res.* **2021**, *207*, 117800.
225. Tang, R.; Zeng, H.; Deng, Y.; et al. Dual Modulation on Peroxymonosulfate Activation Site and Photocarrier Separation in Carbon Nitride for Efficient Photocatalytic Organics Degradation: Efficacy and Mechanism Evaluation. *Appl. Catal. B Environ.* **2023**, *336*, 122918.
226. Cai, C.; Zhang, H.; Zhong, X.; et al. Ultrasound Enhanced Heterogeneous Activation of Peroxymonosulfate by a Bimetallic Fe-Co/SBA-15 Catalyst for the Degradation of Orange II in Water. *J. Hazard. Mater.* **2015**, *283*, 70–79.
227. Pang, Y.; Lei, H. Degradation of p-Nitrophenol through Microwave-Assisted Heterogeneous Activation of Peroxymonosulfate by Manganese Ferrite. *Chem. Eng. J.* **2016**, *287*, 585–592.
228. Marino, L.; Gagliano, E.; Santoro, D.; et al. Fluorescence Sensor Enabled Control of Contaminants of Emerging Concern in Reclaimed Wastewater Using Ozone-Based Treatment Processes. *Water Res.* **2025**, *268*, 122616.
229. Xu, P.; Wei, R.; Wang, P.; et al. $CuFe_2O_4$/Diatomite Actuates Peroxymonosulfate Activation Process: Mechanism for Active Species Transformation and Pesticide Degradation. *Water Res.* **2023**, *235*, 119843.
230. Tran, T.; Do, Q.; Kang, J.; et al. Boosted Micropollutant Removal over Urchin-Like Structured Hydroxyapatite-Incorporated Nickel Magnetite Catalyst via Peroxydisulfate Activation. *Water Res.* **2024**, *249*, 120951.
231. Zhao, X.; Zhang, Z. Heterogeneous Peroxymonosulfate-Based Advanced Oxidation Mechanisms: New Wine in Old Bottles? *Environ. Sci. Technol.* **2025**, *59*, 5913–5924
232. Xie, Z.; He, C.; Zhou, H.; et al. Effects of Molecular Structure on Organic Contaminants' Degradation Efficiency and Dominant ROS in the Advanced Oxidation Process with Multiple ROS. *Environ. Sci. Technol.* **2022**, *56*, 8784–8795.
233. Zhang, H.; Xie, C.; Chen, L.; et al. Different Reaction Mechanisms of $SO_4^{\bullet-}$ and $^{\bullet}OH$ with Organic Compound Interpreted at Molecular Orbital Level in Co(II)/Peroxymonosulfate Catalytic Activation System. *Water Res.* **2023**, *229*, 119392.
234. Ren, W.; Xiong, L.; Yuan, X.; et al. Activation of Peroxydisulfate on Carbon Nanotubes: Electron-Transfer Mechanism. *Environ. Sci. Technol.* **2019**, *53*, 14595–14603.
235. Ren, W.; Cheng, C.; Shao, P.; et al. Origins of Electron-Transfer Regime in Persulfate-Based Nonradical Oxidation Processes. *Environ. Sci. Technol.* **2022**, *56*, 78–97.
236. Yang, S.; He, L.; Peng, P.; et al. Synergistic $Fe^{2+}$/UV Activated Peroxydisulfate as an Efficient Method for the Degradation of Thiacloprid. *Process Saf. Environ. Prot.* **2022**, *161*, 466–475.
237. Cheng, C.; Ren, W.; Miao, F.; et al. Generation of $Fe^{IV}$=O and Its Contribution to Fenton-Like Reactions on a Single-Atom Iron-N-C Catalyst. *Angew. Chem. Int. Ed.* **2023**, *62*, e202218510.
238. Yin, K.; Shang, Y.; Chen, D.; et al. Redox Potentials of Pollutants Determining the Dominate Oxidation Pathways in Manganese Single-Atom Catalyst (Mn-SAC)/Peroxymonosulfate System: Selective Catalytic Mechanisms for Versatile Pollutants. *Appl. Catal. B Environ.* **2023**, *338*, 123029.
239. Jiang, Z.; Wei, J.; Niu, X.; et al. Highly Dispersed $Fe_7S_8$ Anchored on $sp^2/sp^3$ Hybridized Carbon Boosting Peroxymonosulfate Activation for Enhanced EOCs Elimination through Singlet Oxygen-Dominated Nonradical Pathway. *J. Hazard. Mater.* **2024**, *461*, 132607.
240. Pan, J.; Wang, X.; Yang, X.; et al. Insights into the Enhanced Oxidation of Organic Micropollutants by Single-Atom Cu Catalyst Activated Peroxydisulfate: Valence-Dominated Nonradical Pathway. *Appl. Catal. B Environ.* **2024**, *351*, 123997.
241. Zhou, Y.; Jiang, J.; Gao, Y.; et al. Activation of Peroxymonosulfate by Benzoquinone: A Novel Nonradical Oxidation Process. *Environ. Sci. Technol.* **2015**, *49*, 12941–12950.
242. Meng, C.; Wang, Z.; Zhang, W.; et al. Laminar Membranes Assembled by Ultrathin Cobalt-Copper Oxide Nanosheets for Nanoconfined Catalytic Degradation of Contaminants. *Chem. Eng. J.* **2022**, *449*, 137811.
243. Asif, M.; Kang, H.; Zhang, Z. Assembling CoAl-Layered Metal Oxide into the Gravity-Driven Catalytic Membrane for Fenton-Like Catalytic Degradation of Pharmaceuticals and Personal Care Products. *Chem. Eng. J.* **2023**, *463*, 142340.
244. Chen, W.; Li, X.; Wei, X.; et al. Activation of Peroxymonosulfate for Degrading Ibuprofen via Single Atom Cu Anchored by Carbon Skeleton and Chlorine Atom: The Radical and Non-Radical Pathways. *Sci. Total Environ.* **2023**, *858*, 160097.
245. Guan, Y.; Ma, J.; Li, X.; et al. Influence of pH on the Formation of Sulfate and Hydroxyl Radicals in the

UV/Peroxymonosulfate System. *Environ. Sci. Technol.* **2011**, *45*, 9308–9314.
246. Yang, Y.; Guo, H.; Zhang, Y.; et al. Analysis on the Removal of Ammonia Nitrogen Using Peroxymonosulfate Activated by Nanoparticulate Zero-Valent Iron. *Chem. Pap.* **2017**, *71*, 1497–1505.
247. Peydayesh, M.; Suta, T.; Usuelli, M.; et al. Sustainable Removal of Microplastics and Natural Organic Matter from Water by Coagulation–Flocculation with Protein Amyloid Fibrils. *Environ. Sci. Technol.* **2021**, *55*, 8848–8858.
248. Peng, Y.; Zhang, Q.; Ren, W.; et al. Thermodynamic and Kinetic Behaviors of Persulfate-Based Electron-Transfer Regime in Carbocatalysis. *Environ. Sci. Technol.* **2023**, *57*, 19012–19022.
249. Chen, L.; Wang, S.; Yang, Z.; et al. Selective Interfacial Oxidation of Organic Pollutants in Fenton-Like System Mediated by Fe(III)-Adsorbed Carbon Nanotubes. *Appl. Catal. B Environ.* **2021**, *292*, 120193.
250. Du, J.; Sun, B.; Zhang, J.; et al. Parabola-Like Shaped pH-Rate Profile for Phenols Oxidation by Aqueous Permanganate. *Environ. Sci. Technol.* **2012**, *46*, 8860–8867.
251. Chen, T.; Sun, Y.; Dong, H.; et al. Understanding the Importance of Periodate Species in the pH-Dependent Degradation of Organic Contaminants in the $H_2O_2$/Periodate Process. *Environ. Sci. Technol.* **2022**, *56*, 10372–10380.
252. Zhang, X.; Zhang, Y.; Tian, J.; et al. Generating $^1O_2$ and $Co^{IV}$=O through Efficient Peroxymonosulfate Activation by $ZnCo_2O_4$ Nanosheets for Pollutant Control. *Nano Res.* **2024**, *17*, 8025–8035.
253. Shi, P.; Singh, S.; Rani, M.; et al. Bimetallic $CoMn_2O_4$ Spinel as an Effective Catalyst for Peroxymonosulfate Activation toward Perfluorooctanoic Acid Degradation. *Chem. Eng. Sci.* **2026**, *321*, 122792.
254. Liu, Z.; Bikogiannakis, A.K.; Qing, X.; et al. Activation of Peroxymonosulfate by a Core-Shell Structured Carbon-Encapsulated Cobalt Ferrite ($CoFe_2O_4$/CoFe@C) for Bisphenol S Removal: Temperature-Dependent Structure and Degradation Mechanism Elucidation. *Chem. Eng. J.* **2025**, *505*, 159185.
255. Xu, X.; Ji, X.; Bao, Y.; et al. MOF-Derived Porous CoMn Bimetallic Oxide for Efficient Peroxymonosulfate Activation: Electron Transfer Pathway Transition Steered by Synergistic Effect of Nanoconfinement and Bimetallic Sites. *Chem. Eng. J.* **2025**, *525*, 170194.
256. Li, J.; Zou, J.; Zhang, S.; et al. Sodium Tetraborate Simultaneously Enhances the Degradation of Acetaminophen and Reduces the Formation Potential of Chlorinated By-Products with Heat-Activated Peroxymonosulfate Oxidation. *Water Res.* **2022**, *224*, 119095.
257. Wang, L.; Peng, L.; Xie, L.; et al. Compatibility of Surfactants and Thermally Activated Persulfate for Enhanced Subsurface Remediation. *Environ. Sci. Technol.* **2017**, *51*, 7055–7064.
258. Arvaniti, O.; Ioannidi, A.; Mantzavinos, D.; et al. Heat-Activated Persulfate for the Degradation of Micropollutants in Water: A Comprehensive Review and Future Perspectives. *J. Environ. Manag.* **2022**, *318*, 115568.
259. Li, H.; Yang, Y.; Li, X.; et al. Degradation of Sulfamethazine by Vacuum Ultraviolet-Activated Sulfate Radical-Advanced Oxidation: Efficacy, Mechanism and Influences of Water Constituents. *Sep. Purif. Technol.* **2022**, *282*, 120058.
260. Li, N.; Wang, Y.; Cheng, X.; et al. Influences and Mechanisms of Phosphate Ions onto Persulfate Activation and Organic Degradation in Water Treatment: A Review. *Water Res.* **2022**, *222*, 118896.
261. Chen, Y.; Tong, Y.; Xue, Y.; et al. Degradation of the β-Blocker Propranolol by Sulfite Activation Using FeS. *Chem. Eng. J.* **2020**, *385*, 123884.
262. Yan, Y.; Wei, Z.; Duan, X.; et al. Merits and Limitations of Radical vs. Nonradical Pathways in Persulfate-Based Advanced Oxidation Processes. *Environ. Sci. Technol.* **2023**, *57*, 12153–12179.
263. Qin, Y.; Li, H.; Ma, J. Enhanced Degradation of Organic Contaminants by Thermally Activated Peroxymonosulfate in the Presence of Chloride Ion. *Chem. Eng. J.* **2023**, *451*, 138814.
264. Li, L.; Cheng, M.; Sun, H.; et al. Assessing the Discrepant Role of Anions in the Transformation of Reactive Oxygen Species in $H_2O_2$ and PDS System: A Comparative Kinetic Analysis. *J. Hazard. Mater.* **2024**, *480*, 136465.
265. Cao, S.; Yin, Y.; Zheng, S.; et al. Peroxymonosulfate Activation by Ni–Co Nanoparticles Encapsulated in Nitrogen-Doped Carbon Derived from Co-Doped Ni Metal–Organic Frameworks for Efficient Enrofloxacin Degradation. *Chem. Eng. J.* **2025**, *503*, 158281.
266. Dai, C.; Huang, X.; Liu, Q.; et al. Peroxymonosulfate Activation by Ruthenium in Homogeneous Systems for Degradation of Triclosan: Comparison between Ru(II) and Ru(III). *Sep. Purif. Technol.* **2024**, *332*, 125820.
267. An, Y.; Li, X.; Liu, Z.; et al. Constant Oxidation of Atrazine in Fe(III)/PDS System by Enhancing Fe(III)/Fe(II) Cycle with Quinones: Reaction Mechanism, Degradation Pathway and DFT Calculation. *Chemosphere* **2023**, *317*, 137883.
268. Yin, R.; Hou, X.; Lu, S.; et al. Making Waves: Sustainable Control of Micropollutants via NOM-Mediated Photosensitized Activation of Oxidants. *Water Res.* **2025**, *280*, 123492.
269. Wang, C.; Xue, S.; Xu, Y.; et al. Novel Electrocatalytic Capacitive Deionization with Catalytic Electrodes for Selective Phosphonate Degradation: Performance and Mechanism. *Water Res.* **2024**, *256*, 121614.
270. Zhang, Y.; Yip, K.; Kim, Y.; et al. Monolithic Ceramic $CoTiO_3$/$TiO_2$ Membrane Balancing Catalytic Efficiency and Durability in Advanced Oxidation Processes. *Environ. Sci. Technol.* **2025**, *59*, 6863–6871.
271. Xiang, S.; Dong, H.; Li, Y.; et al. Novel Flower-Like Fe-Mo Composite for Peroxydisulfate Activation toward Efficient

Degradation of Carbamazepine. *Sep. Purif. Technol.* **2023**, *305*, 122487.
272. Wang, S.; Wang, J. Cobalt-Silicon Coordination-Induced Nonradical Activation of Peroxymonosulfate for Enhancing the Degradation of Organic Pollutants in Real Wastewater. *Small* **2025**, *21*, 2500434.
273. Chen, F.; Liu, L.; Chen, J.; et al. Efficient Decontamination of Organic Pollutants under High Salinity Conditions by a Nonradical Peroxymonosulfate Activation System. *Water Res.* **2021**, *191*, 116799.
274. Yao, Y.; Wang, C.; Yan, X.; et al. Rational Regulation of Co-N-C Coordination for High-Efficiency Generation of $^1O_2$ toward Nearly 100% Selective Degradation of Organic Pollutants. *Environ. Sci. Technol.* **2022**, *56*, 8833–8843.
275. Chen, Z.; Wang, J.; Yang, B.; et al. Organic Carbon Transfer Process in Advanced Oxidation Systems for Water Clean-Up. *Nat. Water* **2025**, *3*, 334–344.
276. Zhu, C.; Cun, F.; Fan, Z.; et al. Heterogeneous Fe-Co Dual-Atom Catalyst Outdistances the Homogeneous Counterpart for Peroxymonosulfate-Assisted Water Decontamination: New Surface Collision Oxidation Path and Diatomic Synergy. *Water Res.* **2023**, *241*, 120164.
277. Liu, Y.; Lin, Q.; Guo, Y.; et al. The Nitrogen-Doped Multi-Walled Carbon Nanotubes Modified Membrane Activated Peroxymonosulfate for Enhanced Degradation of Organics and Membrane Fouling Mitigation in Natural Waters Treatment. *Water Res.* **2022**, *209*, 117960.
278. Li, Y.; Chen, C.; Gao, S.; et al. Unveiling Roles of Nonradical Electron-Donation Pathway in Peroxymonosulfate Activation for Boosted Interfacial Radical Generation. *Angew. Chem. Int. Ed.* **2025**, *64*, e202507772.
279. Xiao, Z.; Yang, B.; Feng, X.; et al. Density Functional Theory and Machine Learning-Based Quantitative Structure-Activity Relationship Models Enabling Prediction of Contaminant Degradation Performance with Heterogeneous Peroxymonosulfate Treatments. *Environ. Sci. Technol.* **2023**, *57*, 3951–3961.
280. Deng, J.; Li, F.; Qi, Z.; et al. A Novel Redox Synergistic Mechanism of Peroxymonosulfate Activation Using Pd-$Fe_3O_4$ for Ultra-Fast Chlorinated Hydrocarbon Degradation. *Appl. Catal. B Environ.* **2024**, *359*, 124499.
281. Hu, X.; Zhu, M. Were Persulfate-Based Advanced Oxidation Processes Really Understood? Basic Concepts, Cognitive Biases, and Experimental Details. *Environ. Sci. Technol.* **2024**, *58*, 10415–10444.
282. Liu, X.; Liu, Y.; Qin, H.; et al. Selective Removal of Phenolic Compounds by Peroxydisulfate Activation: Inherent Role of Hydrophobicity and Interface ROS. *Environ. Sci. Technol.* **2022**, *56*, 2665–2676
283. Pei, J.; Liu, J.; Fu, K.; et al. Non-Metallic Iodine Single-Atom Catalysts with Optimized Electronic Structures for Efficient Fenton-Like Reactions. *Nat. Commun.* **2025**, *16*, 800.
284. Luo, H.; Fu, H.; Yin, Q.; et al. Carbon Materials in Persulfate-Based Advanced Oxidation Processes: The Roles and Construction of Active Sites. *J. Hazard. Mater.* **2022**, *426*, 128044.
285. Yan, C.; Xu, Z.; Xue, D.; et al. DFT-Assisted Machine Learning for Global Optimization of Fe–Carbon Catalyst: Persulfate Activation and Targeted Removal of Emerging Contaminants. *Catalysts* **2026**, *16*, 444.